Numerical simulation of geomembranes at large deformations

To the Faculty of Geosciences, Geoengineering and Mining (III)

of the Technische Universität Bergakademie Freiberg

approved

DISSERTATION

To attain the academic degree of

Doctor of Engineering (Dr. -Ing.)

submitted

by M.Sc. Eng. Nguyen Duc Vinh

born on the 27 of July 1984 in Ha Noi, Viet Nam

Reviewers:

Prof. Dr. -Ing. habil. Heinz Konietzky, Institut für Geotechnik, TU Bergakademie Freiberg

Prof. Dr.-Ing. Rolf Katzenbach, Institut für Geotechnik, TU Darmstadt

Assoc. Prof. Dr. Nguyen Van Manh, Ha Noi University of Mining and Geology

Date of the award: 14.12.2022

ABSTRACT AND STRUCTURE OF THESIS

This thesis documents the development of a simulation strategy to model the behavior of geomembranes at large deformations using the explicit finite difference code FLAC^{3D}. The geomembrane is represented by special shell elements and interfaces at both sides of the geomembrane duplicating the interaction with the overlying and underlying materials.

Chapter 1 provides an introduction to geotextiles in general, geomembranes in particular, and their use in geotechnical engineering. The general properties of geotextiles are described. Special attention is paid to pull-out tests because of their importance to describe the behavior at large deformations.

Chapter 2 of the thesis describes the proposed 'liner' model concept to simulate the interaction of a geomembrane with the over- and underlying material. Furthermore, this chapter documents in detail the simulation of uniaxial pull-out tests for validation of the proposed 'liner' model concept and compares it with the FLAC^{3D} built-in geogrid element.

To clarify more clearly the potential failure (crack propagation and rupture process) of the geomembrane, the 'liner' model under biaxial loading was investigated. Corresponding results are documented in chapter 3.

Chapter 4 documents a detailed parameter study with a special focus on the stiffness and frictional behavior of the 'liner' element using a simplified waste dump.

In chapter 5 a new constitutive model ("Femesalz") is proposed and described in detail. This constitutive model is able to describe the visco-elasto-plastic behavior of crushed salt and waste rock salt, respectively. Exemplary, the "Femesalz" constitutive model together with the 'liner' model is applied to simulate the behavior of a rock salt waste dump (2.5-dimensional) to validate both, the new constitutive model "Femesalz" as well as the 'liner' model.

Chapter 6 documents the use of the 'liner' element and the "Femesalz" constitutive model to simulate salt dump models in 2D and 3D on different terrain types (mountain, valley, plain) for a time of 100 years to generate large deformations.

Chapter 7 contains the main conclusions and recommendations.

The main results of the thesis can be summarized as follows:

- The proposed ‘liner’ element is suitable to simulate the interaction of the geomembrane with the over- and underlying material even under very large deformations incl. the failure (rupture) of the geomembrane.
- The newly developed constitutive model “Femesalz” is able to describe the visco-elasto-plastic behavior of crushed salt and waste dump rock salt.
- The properties at the interfaces at both sides of the geomembrane have a significant influence on the loading of the geomembrane as well as on the deformation of the overlying material.
- The pronounced topography of the ground below a geomembrane can produce significant local deformations in the geomembrane. Depending on the specific geometry a 3D consideration might be necessary.

ACKNOWLEDGMENTS

On the first days when I arrived in Freiberg, everything was a surprise for me. I even lost my way when I first came to the institute. However, this Ph.D. project fascinated me although I had no knowledge of numerical simulations. Experiencing many difficulties and challenges, sometimes I don't even know if I can complete it or not. However, the positive learning and working environment at Freiberg helped me to overcome all the problems. Above all, the guidance of Professor Dr. habil. Heinz Konietzky is the most important for me.

First of all, I want to express my deep gratitude to my supervisor, Professor Dr. habil. Heinz Konietzky, who always supported me in my research work and real life. I will always remember and cherish the affection and attention from him and his wife. I will always remember the Christmas time with Professor Konietzky's family and foreign colleagues.

Secondly, I also want to thank the research group from K+S company and Itasca, which provided data and resources. I also want to thank all of my friendly colleagues at the Geotechnical Institute at TU Bergakademie Freiberg, especially Dr. Martin Herbst, who helped me a lot during my research period. Also, thanks to Mr. Gunther Lüttschwager and Mr. Fabian Weber.

I also gratefully acknowledge the funding sources that made my Ph.D. work possible. It was funded by the Vietnamese International Cooperation Department, Ministry of Education and Training.

Special thanks to my parents in Vietnam, who always gave me advice and supported me in purchasing my career. During a hard time in Germany, my wife and two daughters were always behind me and gave me the motivation and strength to complete this thesis, although the COVID crisis occurred. Seeing them growing up healthy and being happy every day is my greatest happiness.

CONTENTS

LIST OF TABLES

LIST OF FIGURES

Chapter 1

Chapter 2

NOMENCLATURE

List of notations/ symbols

Symbol	Unit	Explanation
B	m	Width of pull-out box
H	m	Height of pull-out box
L	m	Length of pull-out box
T	K	Temperature
A	-	Material constant
A	-	Viscosity factor
A_p	-	Viscous proportionality factor
a-wipp	-	Structural parameter A (primary creep)
b_o	kg/(s·m^3)	Creep compaction parameter for crushed salt
b_1	Pa	Creep compaction parameter for crushed salt
b_2	kg/m^3	Creep compaction parameter for crushed salt
b-wipp	-	Structure parameter B (primary creep)
B_1	-	Constant determined by mathematical functions of regression analysis of load-controlled triaxial creep tests
B_2	-	Constant determined by mathematical functions of regression analysis of load-controlled triaxial creep tests
B_3	-	Constant determined by mathematical functions of regression analysis of load-controlled triaxial creep tests
B_4	-	Constant determined by mathematical functions of regression analysis of load-controlled triaxial creep tests
c	Pa	Cohesion of soil
C_o	-	Material constant
C_1	-	Material constant
C_1'	-	Constant determined by mathematical functions of regression analysis of load-controlled triaxial creep tests
C_2	-	Material constant
c-ctable	-	Table ID for cohesion during compaction
c-dtable	-	Table ID for dilatancy angle during compaction

c-ftable	-	Table ID for friction angle during compaction
c-ttable	-	Table ID for tensile strength during compaction
D	$Pa^{-n}s^{-1}$	Damage structure parameter
D_1	-	Constant determined by mathematical functions of regression analysis of load-controlled triaxial creep tests
d-wipp	-	Structure parameter D (stationary creep)
E	Pa	Young's modulus
e_{ij}	-	Strain deviator
$\dot{e}_{ij}^{ve}$	s^{-1}	Visco-elastic deformation rate
e_{ij}^{ve}	-	Visco-elastic deformation
$\dot{e}^{vpl,tr}$	s^{-1}	Visco-plastic transient deviatoric strain rate
$\dot{e}^{vpl,tr}$	s^{-1}	Visco-plastic stationary strain rate
E_5	-	Constant determined by mathematical functions of regression analysis of load-controlled triaxial creep tests
E_6	-	Constant determined by mathematical functions of regression analysis of load-controlled triaxial creep tests
E_7	-	Constant determined by mathematical functions of regression analysis of load-controlled triaxial creep tests
E_8	-	Constant determined by mathematical functions of regression analysis of load-controlled triaxial creep tests
F_d	-	Fractional density
G	Pa	Shear modulus
G_f	Pa	Shear modulus of intact salt
G_k	Pa	Shear modulus (Kelvin model)
G_M	Pa	Shear modulus (Maxwell model)
I_1	-	First stress invariant
K	Pa	Bulk modulus
K_f	Pa	Bulk modulus of intact salt
k_n	Pa/m	Normal Stiffness of structural element
k_s	Pa/m	Shear Stiffness of structural element
m	-	Time exponent

n	-	Stress exponent
n_p	-	Stress exponent
n_{max}	-	Maximum pore volume
N_ϕ	-	Shear failure potential constant
N_ψ	-	Stress failure potential constant
n-wipp	-	Stress exponent n (steady-state creep)
P	-	Porosity
Q	cal/mol	Activation energy
rho	kg/m^3	Density
R	-	Force ratio
R_g	cal/mol·K	Universal gas constant
s	Pa	Deviatoric stress
S_{ij}	Pa	Deviatoric stress
t	s	Time step
V	-	Hardening structural parameter
y-ctable	-	Table ID for cohesion during plastic distortion
y-dtable	-	Table ID for dilatancy angle during plastic distortion
y-ftable	-	Table ID for friction angle during plastic distortion
y-ttable	-	Table ID for tensile strength during plastic distortion
ΔV	m^3	Change in volume
V_o	m^3	Initial volume
$\Delta z_{\min}$	m	Smallest dimension of the zone adjoining the interface in normal direction

Greek symbols

Symbol	Unit	Explanation
ρ	kg/m^3	Density
ϕ	^{o}	Internal friction angle
ν	-	Poisson's ratio
σ_i	Pa	Stress vector
ε^d	-	Damage state deformation
σ_{eff}	Pa	Effective stress
ε^{el}	-	Elastic deformation
σ_{eq}	Pa	Von Mises stress
ρ_f	kg/m^3	Density of intact salt
δ_{ij}	-	Kronecker delta
σ_{ij}	Pa	Stress tensor
η_k	Pa·s	Dynamic viscosity (Kelvin model)
σ_o	Pa	Major stress
ε^{pr}	-	Primary creep strain
ε^{sd}	-	Secondary creep strain
ε^{te}	-	Tertiary creep strain
ε_{vol}	-	Volumetric strain
$\dot{\varepsilon}_{cr}^{pr}$	s^{-1}	Primary creep strain rate
$\dot{\varepsilon}_{ij}^{c}$	s^{-1}	Compaction creep rate
ε_{ij}	-	Total creep strain
ε_{ij}^{el}	-	Instantaneous elastic strain
ε_{ij}^{pl}	-	Instantaneous plastic strain
ε_{ij}^{vpl}	-	Visco-plastic strain
ε_{kk}	-	Volumetric strain
$\dot{\varepsilon}_{kk}^{vpl}$	s^{-1}	Visco-plastic volumetric strain rate
$\dot{\varepsilon}_{ij}^{d}$	s^{-1}	Deviatoric strain rate
$\dot{\varepsilon}_{ij}^{de}$	s^{-1}	Elastic deviatoric strain rate

$\dot{\varepsilon}_{ij}^{dv}$	s^{-1}	Viscous deviatoric strain rate
$\varepsilon_{kk,\,max}$	-	Maximum volumetric strain
$\dot{\varepsilon}_{kk}$	s^{-1}	Volumetric strain rate
$\dot{\varepsilon}_{p}$	s^{-1}	Primary creep strain rate
$\dot{\varepsilon}_{s}$	s^{-1}	Secondary creep strain rate
$\dot{\varepsilon}_{ss}^{*}$	s^{-1}	Critical creep strain rate
$\dot{\varepsilon}_{v,c}$	s^{-1}	Compaction creep strain rate
$\dot{\sigma}_{ij}^{d}$	$Pa \cdot s^{-1}$	Deviatoric stress rate
$\dot{\varepsilon}_{cr}$	s^{-1}	Creep strain rate
ε_{ij}^{el}	-	Elastic strain
ε_{pl}	-	Plastic creep strain
ε^{s}	-	Secondary creep strain
ε_{v}	-	Viscous creep strain
η_{M}	$Pa \cdot s$	Dynamic viscosity (Maxwell model)
$\bar{\sigma}$	Pa	Von Mises stress
$\sigma_{t,\,max}$	Pa	Tensile strength
μ	-	Constant of creep law

Mathematical functions/ definitions

Max	Maximum value of a respective variable
Min	Minimum value of a respective variable
+	Referred to tensile stresses in $FLAC^{3D}$
-	Referred to compressive stresses in $FLAC^{3D}$
x, y, z	Cartesian coordinates

Abbreviations

BAM	Bundesanstalt für Materialforschung und -prüfung
CCL	Compacted Clay Liner
CD	Cross-machine Direction
EPDM	Ethylene Propylene Diene Monomer
FEM	Finite Element Method
$FLAC^{3D}$	Fast Lagrangian Analysis of Continua in 3 Dimensions
GCL	Geosynthetic Clay Liner
HDPE	High-density Polyethylene
ID	Identification
LLDPE	Linear Low-Density Polyethylene
MD	Machine Direction
NW	Nonwoven Geotextile
PA	Polyamide
PE	Polyethylene
PET	Polyethylene Terephthalate
PP	Polypropylene
PVC	Polyvinyl Chloride
UV	Ultraviolet
DEM	Discrete Element Method
WIPP	Waste Isolation Pilot Plant
CST	Constant-Strain-Triangle
DKT-CST	Discrete-Kirchhoff-Triangle - Constant-Strain-Triangle
REF	Reference
RPP	Reinforced Polypropylene
TRP	Reinforced Polyethylene

CHAPTER 1: INTRODUCTION AND STATE-OF-THE-ART

1.1 Geosynthetics for geoengineering projects (overview)

Geosynthetics are synthetic products manufactured from a polymeric material. Geosynthetics have many advanced functions such as separation, and applications, including roads, airfields, embankments, reservoirs, dams, erosion control, landfill liners, landfill cover, mining, etc. There are different types of geosynthetics, including geotextiles, geomembranes, geogrids, geosynthetic clay liners, geocomposite sheet drains, geocomposite strip drains, geocells, erosion control products or HDPE vertical barrier systems (Zornberg & Christopher, 2007). The characteristics of these materials vary considerably, primarily due to their applications: reinforcement, filtration, drainage, barrier, protection, etc. Therefore, geosynthetics are used widely in many fields, especially in geoengineering.

With the function of separation and protection, geotextiles and geomembranes are embedded under constructions such as waste dumps, dams, and stockpiles. Geosynthetics must ensure stability and withstand large deformation over a long lifetime of up to 100 years or even more.

For the mining industry, it is essential to reuse tailings and ensure the safety of mine waste. Such tailings may contain small amounts of toxic substances such as radioactive substances or heavy metals with deadly chemicals from the ore extraction process, such as cyanide or sulfuric acid. The treatment of such landfills is one of the most important requirements for environmental protection, so geosynthetic systems such as geomembranes, geotextiles, geosynthetic clay liners, geogrids, and geocomposite drainage materials are chosen as effective solutions to ensure long-term safety.

To achieve high efficiency while still protecting a safe and sustainable environment, up to 40% of the geotextile material is used by the mining industry (Post & Maubeuge, 2018). One of the prominent issues in mining is the construction and maintenance of safe and stable mining waste dumps. The two most common problems are dump leaching and slope stability. To solve these two problems, geosynthetics in general, and geotextiles/geomembranes, in particular, have been used as effective solutions. Fig. 1.1 shows the application of geosynthetics for tailing management.

a) Classification of geotextiles and geomembranes

Geotextiles

Geotextiles are made from petroleum by-products from one or two polymers (polyamides) such as polyester (PET) or polypropylene (PP). Depending on the compound and structure, each type of geotextile has different physico-mechanical properties such as tensile strength, maximum elongation, water permeability, adaptive environment, etc. Geotextiles are divided into three main groups based on fiber composition: woven, non-woven, and composite geotextiles (knitted geotextiles) (Greenwood, Schroeder, & Voskamp, 2015).

Figure 1.1: Geosynthetics applied for tailing management (naue)

The woven group includes weft-woven yarns resembling textile fabrics, such as polypropylene woven geotextiles. The deformation of this material is usually tested in two main directions: longitudinal direction, abbreviated NW (machine direction), and transverse direction, abbreviated CD (cross-machine direction). The tensile strength in the longitudinal direction is always greater than the tensile strength in the transverse direction. Ordinary woven fabrics are used as reinforcement for ground treatment works when required.

A non-woven geotextile consists of continuous short and long yarns, not in particular directions, which are bonded together by chemical (using adhesives), thermal (using heat), or mechanical (using a needle) methods.

Complex fabrics are a combination of woven and non-woven fabrics. Manufacturers sew bundles of load-bearing (woven) yarns onto a non-woven base to create a product that has the full functionality of woven and non-woven geotextiles.

At present, the basic material of geotextiles is mainly synthetic fiber. Polypropylene (PP) is the most frequently used material in connection with geotextiles, followed by polyethylene terephthalate (PET) and polyethylene (PE) (Prambauer et al., 2019).

Polypropylene is used mostly for geotextile fibers because of its low cost, low density, acceptable tensile properties, and chemical inertness. However, polypropylene is sensitive to UV and heat, demonstrating poor creep characteristics (Stepanovic et al., 2016).

PET has high tensile strength properties and high creep resistance. The geotextiles made of polyester fiber can be used at high temperatures. The main disadvantage of polyester fiber is that it is easy to hydrolyze and degrade in soils with a pH value of more than 10 (Pelyk et al., 2019).

Although polyethylene fibers are typically used to make geomembranes, the scarcity of polyethylene fibers means that it is rarely used for geotextiles. Polyamide is also rarely used for geotextiles due to its poor overall performance (Rawal et al., 2016).

Table 1.1: Properties of most common polymers used as geotextiles (Atrechian et al., 2018)

Type of Fiber	Polypropylene (PP)	Polyethylene Terephthalate (PET)	Polyethylene (PE)	Polyamide (PA)
Density (kg/m^3)	910	1400	920-960	1140
Modulus of elasticity (GPa)	1.5-1.2	2-2.5	5-100	1-8.3
Tensile strength (MPa)	240-900	45	80-600	75-80
Maximum elongation (%)	15-80	120	4-100	55-60
Acid resistance	High	Low	High	High
% of total geosynthetic geotextile production	~92	~5	~2	~1
Corresponding geotextile price ($\$/m^2$)	0.22-2.5	0.15-2.0	0.11-1.2	0.27-1.5

Typically, additives are added to improve the performance of geotextiles, such as B. Antioxidants, hindered amine light stabilizers, UV absorbers and stabilizers, long-term thermal stabilizers, processing modifiers, flame retardants, lubricants, and antibacterial agents (Wiewel et al., 2016).

According to the guidelines for the certification of geotextiles for filtration and separation in landfill sealing systems by BAM (Bundesanstalt für Materialforschung und Prüfung, 2015), geotextiles used as seals under landfills with separation functions must fulfill several physical characteristics such as mass per unit area must be at least 300 g/m², the thickness at least 3 mm; in addition, there are also some requirements for durability and longevity such as resistance to

chemicals, resistance to aging, resistance to weathering and resistance to micro-organisms. Some of the major mechanical properties of geotextiles are direct shear strength and pull-out strength (which is discussed in more detail in section 1.2).

Geomembranes

According to (Matthew, 2021), geomembranes are classified into HDPE, LLDPE, PVC, EPDM, RPP, and TRP.

HDPE (High-Density Polyethylene) geomembrane

HDPE is the most widely used geomembrane due to its durability, strong UV resistance, and inexpensive material costs. HDPE geomembranes are often chosen for exposed applications such as landfills, water reservoir covers, and pond and sewer liners. The reason for this is low material costs and high chemical resistance.

LLDPE (Linear Low-Density Polyethylene) geomembrane

LLDPE geomembranes provide more flexibility than HDPE. So, LLDPE makes installations where an impermeable geomembrane is required easier. It is made with virgin polyethylene resins, making it resistant to low temperatures and ultraviolet exposure. LLDPE geomembranes are also suited for long-term use and remain strong and durable for years. Its best use relates to industrial applications, such as liquid storage tanks and environmental and animal waste containment.

PVC (Polyvinyl Chloride) geomembrane

The polyvinyl chloride resin used for PVC geomembranes is made by cracking ethylene dichloride into a vinyl chloride monomer. PVC geomembranes are used as thermo-plastic waterproofing materials, plasticizers and stabilizers. It is then polymerized to make PVC resin. The material is tear-, puncture-, and abrasion-resistant, making it ideal for preventing contaminants from entering water sources and ensuring drinking water supply. PVC geomembranes are highly flexible and are best suited for landfills and sewers, tank liners, soil remediation, and sewage lagoon liners.

EPDM (Ethylene Propylene Diene Monomer) geomembrane

EPDM geomembrane is a flexible and durable material that can resist punctures and extreme weather conditions. It has a rubber-like texture and is UV-stable with great strength. EPDM geomembranes are typically used as surface barriers for dams and other irrigation sites. It is also

easy to install, so backyard landscapers use this type of geomembrane. It is suitable for agricultural applications such as irrigation ponds, liners, and covers.

RPP (Reinforced Polypropylene) geomembrane

RPP geomembranes are polyester-reinforced liners for long-term water containment and industrial waste applications. It's made from a UV-stabilized polypropylene polymer that gives the material flexibility, stability, and chemical resistance. RPP geomembranes are perfect for applications where folds appear due to uneven and inconsistent weather conditions. It is supported with nylon scrim to ensure it remains strong and durable. This geomembrane type is typically used in municipal applications, evaporation pond liners, and mine tailings.

TRP (Reinforced Polyethylene) geomembrane

TRP geomembranes use polyethylene fabric for long-term water containment and industrial waste applications. TRP geomembranes are chosen for lining temporary retaining ponds. TRP geomembranes are also a durable solution for soil remediation. Its physical properties include chemical resistance, low-temperature resistance, and ultraviolet stability. This type of geomembrane is used for canals, landfills as well as agricultural and municipal applications. Tab. 1.2 provides some typical properties of geomembranes.

Table 1.2: Properties of geomembranes (Bacas, 2011; Bentofix, 2000)

Parameter	Bextofix (2000)	Abel (2003)	Koerner (2005)	Bacas (2011)	Sika (2014)	GSE (2015)
E-Modulus (MPa)	-	200	720	75	100	150
Tensile strength (MPa)	33	-	23	-	15	26
Density (kg/m^3)	917	950	-	-	890	944
Thickness (mm)	7	2.5	1.5	-	≥2	2.5
Maximum stretching (%)	10	-	15	-	-	10

b) Typical applications of geotextiles and geomembranes at large deformation

Geotextiles and Geomembranes are used in the mining industry with a focus on separation, filtration, drainage, and reinforcement, see for instance (Palmeira et al., 2010; Dolez et al., 2017; Tuomela et al., 2021). The functions of separation, drainage, and filtration with four geosynthetic systems (Andy et al., 2018) are illustrated in Fig. 1.2.

The mining dump shown in Fig. 1.2 has four geosynthetic systems. Under the dump, three geosynthetic systems are applied to prevent heap leaching. The non-woven geotextile is responsible for separating soil particles from impermeable layers such as geomembranes or geosynthetic clay liners, which have poor penetration resistance, and at the same time, the geotextile helps to create a conducive seepage system at the bottom of the landfill into the seepage ditch. The fourth geosynthetic system is responsible for covering the slope to prevent surface water from seeping into the landfill and creating a surface drainage system.

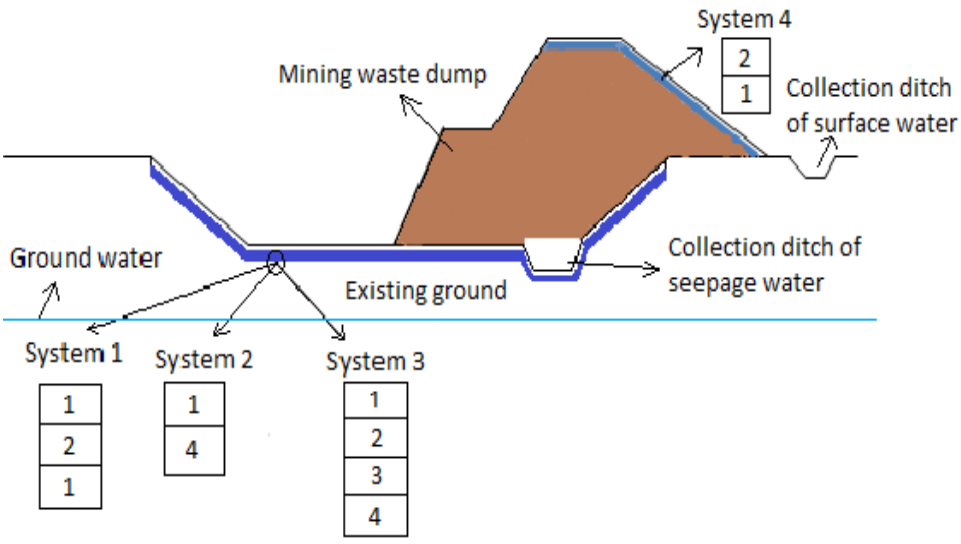

Figure 1.2: Mine waste dump with four geosynthetic systems (Andy et al., 2018)
(1) non-woven geotextile, (2) geomembrane, (3) geosynthetic drainage material, (4) geosynthetic clay liner

According to Pries et al. (2014), single and double composite liner systems are usually used as heap leach pads.

Single liner systems (Fig. 1.3a) are used for heap leaching systems (flat pad, on-off pad, or valley pad) where the hydraulic head (= leachate mound height) is low. A single liner system consists of the existing foundation (subsoil), the low permeability layer under the geomembrane, either a Compacted Clay Liner (CCL) or a Geosynthetic Clay Liner (GCL), the geomembrane, a protective layer (geotextile), and the mineral drainage layer (including solution collection/air injection pipes). Double liner systems are used if higher leach solution hydraulic heads are expected on top of the liner system to reduce the hydraulic head on the bottom geomembrane and to minimize the leakage of solution from the facility. As shown in Fig. 1.3b, a double liner system is built on top of the prepared surface/foundation, starting with the low permeable layer,

either as Compacted Clay Liner (CCL) or as Geosynthetic Clay Liner (GCL). On top of the low permeable soil, the secondary geomembrane liner, the leak detection, and recovery layer, and the primary geomembrane will be placed. Finally, the mineral drainage layer, including the piping, is installed.

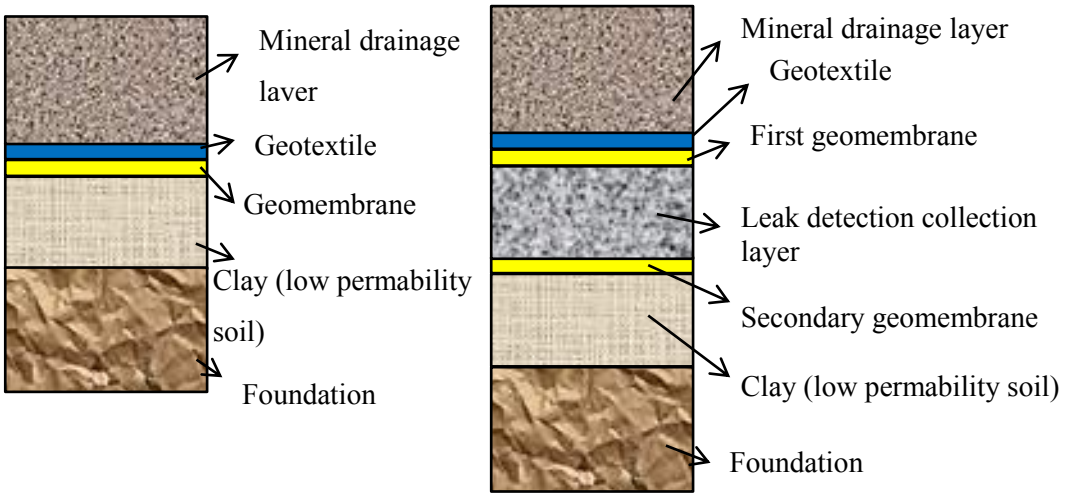

a) *b)*

Figure 1.3: Scheme of liner systems (Pries et al., 2014)

a) Single composite liner system; b) Double composite liner system

The potential failure of geotextiles and geomembranes at critical points under the landfill is depicted in Fig. 1.4. Initially, at critical points (possibly due to topographic factors or errors in the construction process), the soil particles under the pressure of the landfill create large local deformations to the geotextile/geomembrane and cause damage to the geosynthetic system. Water seeps from the top down according to this destructive tear and causes the phenomenon of heap leaching.

It can be seen that geosynthetics in general and geotextiles/ geomembranes, in particular, are smart solutions when building mining waste dumps. With the features mentioned above, geotextiles/ geomembranes contribute to the sustainable development of mining operations as well as keeping the environment free of pollution. However, unlike geotextiles, geomembranes are highly impermeable which allows them to work as hydraulic barriers in landfill structures (Shirazi et al., 2019).

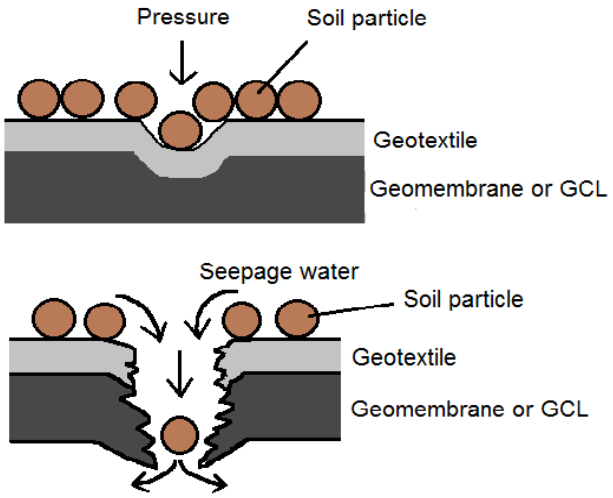

Figure 1.4: Sketch to illustrate damage process due to local large deformations

1.2 Pull-out tests (overview)

According to Jewell et al. (1985) and Milligan et al. (1988), the interface between soil and geosynthetics has three main characteristics: namely bearing, sliding, and bonding. Bearing is the load capacity due to the ground, sliding is the movement along the geosynthetic surface of the soil layer above or below the geosynthetic, and bonding represents the link between the soil and the geosynthetic that is mobilized when pulling the geosynthetic out of the soil.

In order to determine the interaction between geosynthetic and soil, many experimental studies have been performed, such as pull-out tests (Duszyńska et al., 2004; Abu-Farsakh et al., 2006; Sayao et al., 2009; Lopes et al., 2010; Hsieh et al., 2011; Chen et al., 2013; Kayadelen et al., 2018), direct shear tests (Tuna et al., 2012; Cen et al., 2018); triaxial compression tests (Nguyen et al., 2013; Markou, 2018) and ring shear tests (Effendi, 2011). In addition, 2D and 3D numerical simulations (Zhang et al., 2008; Stahl et al., 2011; Abdi et al., 2013; Hegde et al., 2018; Xu et al., 2018, Bacas et al., 2015, Beneito et al., 2020) were performed to duplicate such experiments. Among those, direct shear tests and pull-out tests are performed the most. However, the results of those two tests varied significantly considering laboratory test designs and numerical simulations (Murthy et al., 1993).

Hsieh et al. (2011) performed laboratory tests with large-scale direct shear / pull-out machines. He concluded that the shear resistance determined in the pull-out tests is lower than in the direct shear tests, and the failure mechanisms of direct shear tests and pull-out tests are quite different. In the direct shear test, a sliding surface is usually observed in the soil or at the interface between

soil and geosynthetic. During the pull-out test, there are two sliding surfaces above and below the soil or at the interface between the soil and geosynthetic.

Lopes et al. (2010) conducted direct shear tests and pull-out tests. Their results showed a dependence of the measured horizontal force on the vertical stress, difficulties in performing a direct shear test with a constant area with the bottom half of the box filled with soil, and in measuring the vertical displacement of the loading plate. In contrast, the properties of the soil / geosynthetic interface during extraction, when the geosynthetic is in full contact with the soil, cannot be determined based on the results of direct shear tests, as with this attempting to ignore the contribution of the deformation of the geosynthetic to the properties of the interface when moving out.

According to Bacas et al., (2015), the direct shear behavior of the geotextile/ geomembrane interface under a dump was studied by direct shear tests with eight types of geosynthetic materials. Those 3 types of geotextiles and 5 types of geomembranes are shown in Tab. 1.3.

Fig. 1.5 shows interfaces' typical shear strength behavior for nonwoven geotextile / textured geomembrane interfaces. The shear strength - shear displacement curves show a strain-softening behavior, i.e., the shear strength of the interface decreases with increasing shear displacement. The higher the normal stress, the stronger the softening behavior. This phenomenon is observed in rock joints, but unlike geosynthetic interfaces, here: the higher the normal stress, the lower the elongation-softening behavior.

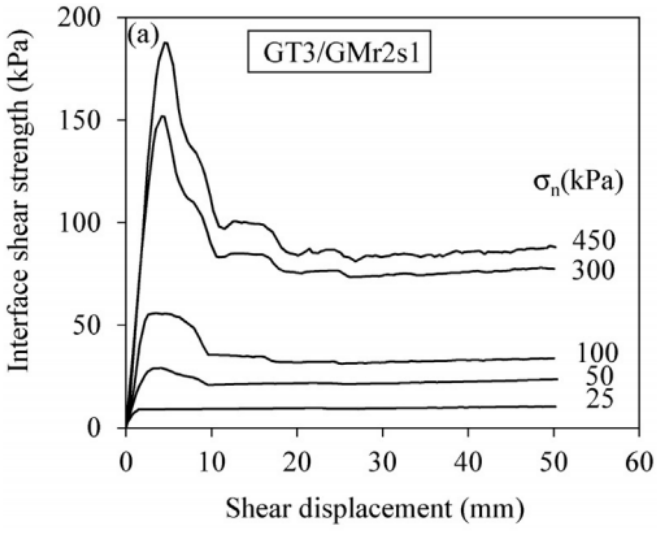

Figure 1.5: Typical interface shear strength behavior for nonwoven geotextile/textured geomembrane interfaces (Bacas et al., 2015)

Fig. 1.6 illustrates how the maximum shear strength of the interface is achieved with a small shear displacement (peak displacement) where the angle of friction is mobilized first, and then the hook and loop interact, whereby the shear strength reaches its maximum value. After the peak, the hook and loop mechanism declines as the threads are pulled out of the geotextile, torn, and untangled until the residual shear strength of the interface is reached.

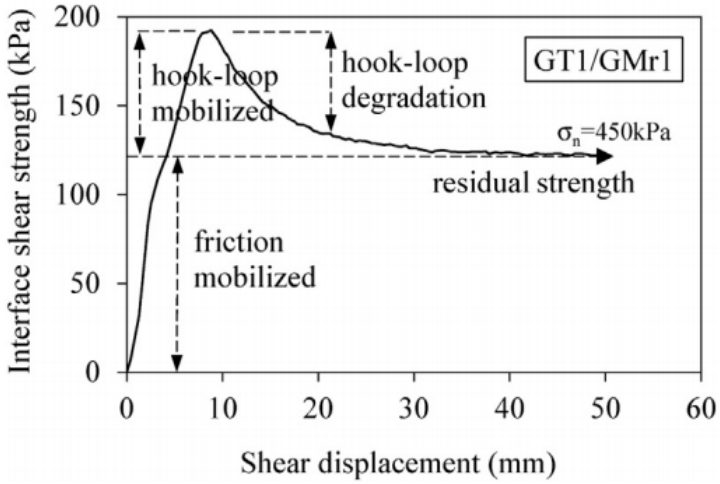

Figure 1.6: Illustration of the decomposition of strain-softening behavior (Bacas et al., 2015)

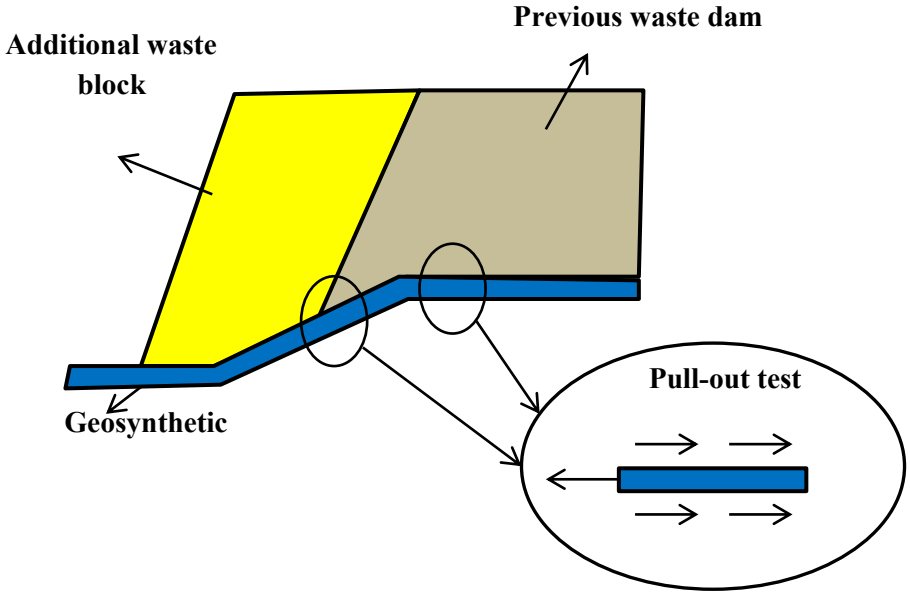

Figure 1.7: Cross-section of waste dump expansion with critical points of deformation

One specific task of this study (discussed later in more detail in chapter 6) refers to the expansion of a waste dump or the phased construction of a waste dump on a surface with uneven topography, as shown in Fig. 1.7, considering the stretching of the geotextile due to creep and

gravitational loading by a waste dump. When an additional waste block is added at critical points of the geosynthetic below, destructive traction can appear. Therefore, the pull-out test is an appropriate test to investigate such a situation.

Table 1.3: Types of geosynthetics (modified from Bacas et al., 2015)

Geo-synthetic	Label	Type	Raw material / Type of fiber	Manufacturing process	Mass/ area (g/m^2)	Density (g/m^3)	Thickness (mm)
Geotextiles	GT1	NW	PP/monofilament	Needle-punched	500		4±0.2
	GT2	NW	PP/staple fibers	Needle-punched	500		5±0.6
	GT3	NW	70%pp + 30% PE/monofilament	Thermally bonded	335		2±0.2
Geomem-branes	GMr1	Textured (~0.5mm)[a]	HDPE	Coextrusion nitrogen gas		≥ 0.94	1.5
	GMr2	Textured (s1:~1.2; s2:~0.8)[b]	HDPE	Calendared structured		≥ 0.94	1.5
	GMr3	Textured (~1.3)[a]	HDPE	Structured same resin as base		0.94	1.5
	GMr4	Textured (~0.25)[a]	HDPE	Coextrusion nitrogen gas		≥ 0.93	1.4
	GMr5	Smooth	HDPE	Flat sheet extrusion		0.94	1.5

Note: NW = Nonwoven geotextile; PP= Polypropylene; PE = Polyethylene; HDPE = High density polyethylene.
a. Average asperity height (mm).
b. Average asperity height of GMr2 presents two different textured sides: s1 = side 1 and s2 = side 2.

Laboratory and field pull-out tests

Pull-out tests with geotextiles were carried out in the field and the laboratory. Abu-Farsakh et al. (2006) compared these two tests and conducted experiments with four types of geogrid and three types of geotextile in a marginal silty clay soil of medium plasticity. Their study indicated that the field test results generally agree with the laboratory test results. However, the results of field experiments were greatly influenced by possibly non-uniform in-situ compaction and possibly arching of geosynthetic strips caused by the walled settlement.

Mohiuddin (2003) also indicated that laboratory and field pull-out test results are close to each other and recommended for the field pull-out tests that displacements should be measured at the end of each specimen length (by a glued strain gauge) to account for the effect of the pull-out. He also suggested that numerical modeling might be a better method to understand the behavior of the interface between soil and geosynthetics.

Typical pull-out devices are shown in Fig. 1.8 and Fig. 1.9. The pull-out box illustrated in Fig. 1.8 has internal dimensions for small (e.g. L x B x H = 0.25 x 0.15 x 0.15m), medium (e.g. L x B x H =0.6 x 0.4 x 0.4m), and large scale boxes (e.g. L x B x H = 1.3 x 0.8 x 0.5m) into which soil and reinforcement are installed (L, B, and H = length, width, and height of the box) **(Minažek, 2013)**. The vertical plate supplies and ensures even and stable vertical pressure distribution. A Geosynthetic embedded in the ground is fitted with sleeves to reduce the influence of the front wall. An electric pull-out system is connected to the geosynthetic via a clamp to prevent specimen damage.

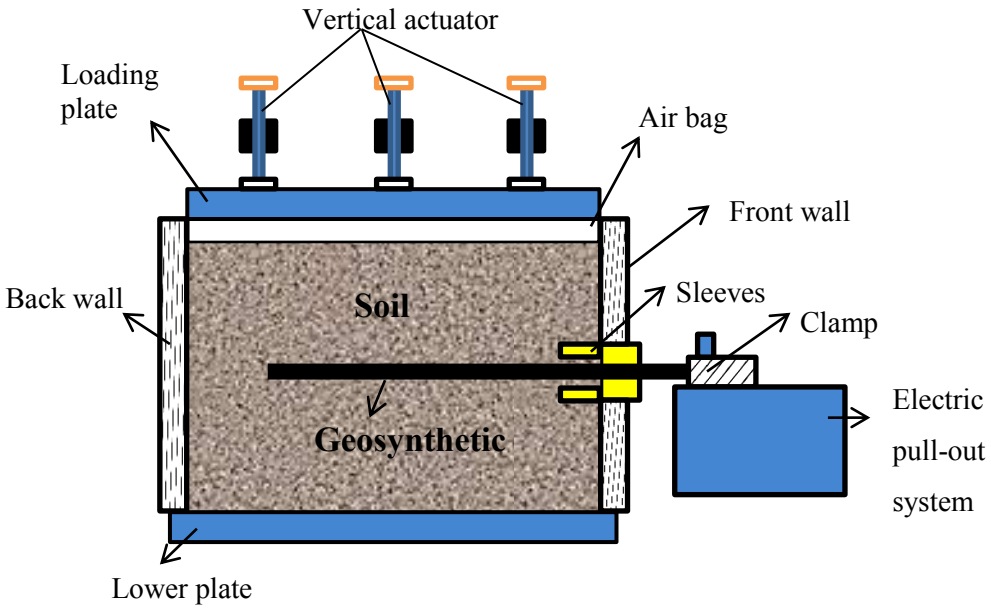

Figure 1.8: Cross-sectional sketch of a pull-out test device

Fig. 1.9 shows the ADS500 large-frame shear box device in the laboratory of the Geotechnical Institute, TU Bergakademie Freiberg, Germany. The machine has a pull-out box with dimensions of 437 x 437 mm, a pulling speed from 0.01 to 1 mm/min, and generates vertical pressure from 25 to 500 kN/m^2.

Duszyńska et al. (2004) conducted a large-scale pull-out test with a biaxial geogrid embedded in coarse sand. They concluded that the pull-out resistance of geosynthetics anchored in the ground depends on many factors, such as the soil and reinforcement properties, the stresses in the soil, the model test conditions, and the parameters of the test device.

Abu-Farsakh et al. (2006) conducted experiments with two types of weak geogrids and two types of strong geogrids in silty clay soil. The authors indicated that the pull-out load increases with the increase in confining pressure. For most laboratory pull-out tests, the peaks (ultimate loads) were observed and defined either by plastic flow (failure) or reinforcement rupture. One also can notice that the geosynthetics continue to have a resistance load after reaching the peak pull-out load (residual load). Research also shows that weak geogrids have higher strain and normalized shear values than stronger geogrids.

Figure 1.9: DS500 large-frame shear box device (Geotechnical Institute, TU Bergakademie Freiberg, Germany)

Moraci et al. (2008) performed large shear box pull-out tests with knitted and welded geogrids embedded in granular soils and stated that in the trigger phase as well as in the peak state, the elongation of the reinforcement increases with the increase in the applied vertical stress; pull-out resistance and apparent interface coefficient of friction depend on the dilatancy of the soil at the interface. The values of the peak pull-out resistance measured in the tests are quite similar for the two different geogrids.

Decreasing displacements were observed along the length of the geogrid in pull-out tests conducted in fine and coarse soil by Sayao et al. (2009) due to the extensibility of the grids. As a result, the strains along the grid also decreased, whereby the mobilized shear strain is unevenly distributed and drops to zero at the end of the grid. They also observed an approximately linear strength envelope.

Chen et al. (2013) performed pull-out tests with biaxial and triaxial geogrids in railway ballast. They mentioned that the triaxial geogrid outperforms the biaxial geogrid, and the geogrid aperture size is more influential than the tensile strength or thickness of ribs. This study also provided good predictions of the pull-out resistance and the distribution of contact forces in the geogrid embedded in ballast. In addition, the calibrated geogrid model and the use of clumps to model ballast particles hold much promise for investigating the interaction between geogrids and ballast and can therefore be used to optimize the product.

Small-scale pull-out tests were also performed by Kayadelen et al. (2018) with geogrids embedded in the sand. They mentioned that when the displacement increases, the pull-out resistance increases up to a certain displacement, but after a certain pull-out displacement, the pull-out resistance decreases as the displacement increases. The results showed that the relative density of the sandy soil and the normal stress acting on the sample are the dominant parameters for the increase in the pull-out load due to the interlocking of soil grains with geogrid gaps. Interface friction between soil and geogrid was also observed to be greater than the internal friction of soil. The observed relationship between pull-out load and normal stresses was nearly linear. While it increases with increasing relative density at low normal stresses, it tends to decrease at higher normal stresses. On the other hand, it was found that the gradation of the sandy soil has a smaller influence on the pull-out load.

It can be seen that most of the pull-out tests mentioned above focus on reinforced geosynthetics for non-cohesive soils such as sand or gravel. The results of these studies show that the behavior of the soil-geosynthetic interface follows the general rule of nonlinear visco-elastic materials in terms of stress and strain (Schmachtenberg, 1985), as shown in Fig. 1.10.

However, the pull-out resistance depends on many factors. A study by Bauer et al. (1988) indicated that the pull-out resistance is mainly influenced by friction, including friction of soil particles over the reinforcement and friction of soil particles on soil interlocked in grid apertures.

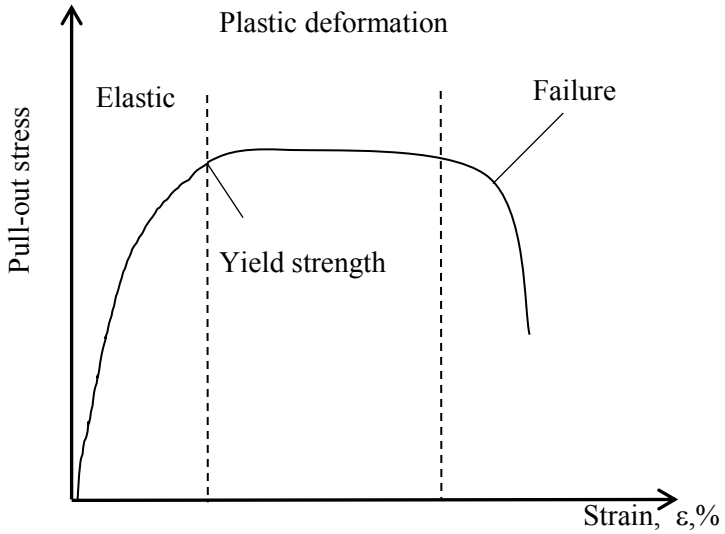

Figure 1.10: Generalized pull-out stress versus strain curve of a soil-geosynthetic interface

Besides that, the passive soil resistance to the grid transversal ribs also influences the pull-out resistance. Therefore, soil's physical and mechanical properties and geosynthetic geometry also greatly influence the pull-out resistance. Moraci et al. (2014) conducted pull-out tests in soils with two different grain sizes. They concluded that pull-out resistance depends on soil particle size, average grain size, and soil mechanical properties, as well as geosynthetics stiffness and geometry. In particular, pull-out resistance increases with the increase of soil shear strength and geogrid bearing area.

Ferreira et al. (2020) performed pull-out tests in granitic residual soil and indicated that soil density is a key factor affecting reinforcement pull-out resistance and failure mode at the interface regardless of geosynthetic type or soil moisture content.

The results of the laboratory pull-out tests are influenced by boundary effects, variations in testing procedure, soil placement, and compaction schemes (Juran et al., 1988). Therefore, numerical simulation is an additional and effective tool to find solutions to those problems.

Numerical simulation for pull-out tests

Numerical simulations of pull-out tests in 2D or 3D were performed by using discrete element methods (DEM) or continuum-based methods, like the finite element method (FEM) or finite difference method (FDM).

Konietzky et al. (2004) and McDowell et al. (2006) used DEM studies to look at the interaction between geogrids and the surrounding area in triaxial and small shear box pull-out tests. They

investigated contact force distributions, deformations, and particle rearrangements. The simulations showed the development of strong contact forces in the vicinity of the geogrid area due to the interlocking. It was also found that a well-defined reinforced zone was approximately 10 cm above and below the geogrid, although this may depend on the size of the rock particles and the type and size of the geogrid.

Zhang et al. (2008) and Xu et al. (2018) also used DEM to simulate geogrid pull-out tests in granular soil and gravelly sand. Zhang pointed out that the density has a great influence on the restrained dilatancy effect on soil reinforcement interaction during the pull-out test. Xu et al. figured out the effects of gradation on the pull-out responses and investigated displacement distribution along the geogrid, normal stress distribution in the geogrid plane, and pull-out force at different clamp displacements.

Chen et al. (2013) used the DEM to simulate large shear box pull-out tests for biaxial geogrids embedded in ballast. The authors calibrated the geogrid model and the two-ball clump models to describe the interaction between ballast particles and geogrid. It is mentioned that DEM simulations provide good predictions of the trend of pull-out force, especially for the initial 20 mm displacements.

The DEM can study the interaction between geogrid and soil particles directly, especially in coarse-grained soils. However, large-scale simulations of experiments for cohesive soils or fine sands with a huge number of particles exceed the currently available computer power. Moreover, for non-woven geotextiles and geomembranes, continuum-based methods are an appropriate solution.

Perkin et al. (2003) performed 2D FEM geogrid pull-out test simulations. In this study, the geogrid was modeled as a 4-node membrane element (elasto-plastic continuous layer). The Coulomb friction model has been applied to the soil-geogrid interfaces. The result showed that the load-displacement predictions were not much influenced by the geosynthetic creep properties, but the load-displacement relationship was significantly influenced by the plasticity when the geosynthetic approaches failure.

Abdi et al. (2013) conducted continuum-based 2D pull-out test simulations for a geogrid embedded in pluviated and compacted sand. An elasto-plastic Mohr-Coulomb model and normal pressure were applied, and an optimum sand layer thickness was determined. The authors indicated that the strengthening effect of sand layers combined with geogrid reinforcement

increased with an increase in normal pressure. Test results showed that the provision of thin layers of sand on both sides of the geogrid effectively improves the pull-out strength.

Bhattacharjee et al. (2011) simulated pull-out tests for geotextile in an oblique direction and compared them with laboratory test results. The backfill soil is modeled as an elasto-plastic Mohr-Coulomb material coded with a hyperbolic soil modulus. At the same time, the geogrid structural element with three nodes was applied for the geotextile reinforcement. Results of the simulation and laboratory matched with each other. The alignment of the reinforcement slightly influences the interaction behavior, and the pull-out behavior of the geosynthetic material is affected by the prototype's size. The numerical model helped to scale the experiment to larger dimensions and facilitated the variations in reinforcement and adjacent soil.

Hussein et al. (2013) used a continuum-based 3D model to simulate pull-out tests for geogrid embedded in the sand. The elasto-plastic Mohr-Coulomb model was applied for the sand, and a nonlinear elastic-plastic constitutive model was developed to simulate the geogrid. A general agreement between calculated and measured geogrid pull-out resistance was observed. The results showed that the contribution of the load-bearing (transversal) elements to the total pull-out resistance is about 36%. In addition, the pull-out load increases with increasing the internal angle of friction of the soil and the interaction coefficients.

CHAPTER 2: 'LINER' CONCEPT AND NUMERICAL SIMULATIONS OF UNIAXIAL PULL-OUT TESTS

2.1 Introduction

As mentioned in chapter 1, pull-out tests are often used to determine the strength and deformation characteristics of geotextiles and geomembranes in particular interacting with surrounding soil, rock, or waste material. To simulate this process, elastic, elasto-plastic, and elasto-visco-plastic material descriptions are required. Special attention has to be paid to the interaction between the geotextile and the underlying and overlying materials.

The study considers two different approaches to simulate the interaction of a geomembrane with underlying and overlying materials. A sensitivity analysis is performed to estimate the influence of individual parameters on the simulation results. The robustness of numerical simulations is proven.

2.2 Numerical calculations

2.2.1 General considerations

The 3-dimensional simulation of geomembranes should meet the following requirements:

- The geomembrane acts as a flexible material with limited tensile strength.
- The geomembrane has a frictional contact on both sides (possibly also a cohesive bond, possibly a tensile bond) with the over- and underlying material
- The thickness of the geomembrane has to be taken into account
- The calculations should be performed optionally in large- or small-strain mode
- The geomembrane should be modeled with isotropic and, if necessary, also anisotropic stiffness and strength parameters
- The geomembrane should be installed or activated step by step to follow the actual installation sequence in-situ
- It should be possible to model any interface stiffness at the contact between the geomembrane and the surrounding material
- It should be possible to represent thermal expansion/ contracting, if necessary

- The utilization factor of the geomembrane (actual stress to strength limit) should be permanently monitored and read out.

FLAC^{3D} provides a predefined element called ‘geogrid’, which was developed to simulate the behavior of geotextiles interacting with a surrounding rock or soil mass. On the other hand, FLAC^{3D} provides other basic elements like volume elements, shell elements, and interface elements, which can be used in combination to represent a geomembrane, but requires special programming. In the following the former one is called 'geogrid' element and the later one 'liner' element.

Both elements offer certain basic characteristics that meet the mentioned requirements to a large extent. Special additional characteristics can and have to be added using the FLAC^{3D} internal programming language FISH.

However, there is a significant difference between these two elements ('geogrid' versus 'liner'). The 'geogrid' element allows only equal interaction on both sides of the geomembrane, and the relative displacement between the materials on both sides is limited.

2.2.2 Concept of the 'liner' element

The basic idea of the ‘liner’ element is to overcome the two main restrictions of the ‘geogrid’ element, namely the restricted movement and failure potential, respectively, as well as the equal properties at both sides of the geomembrane. The concept of the ‘liner’ element is shown in Fig. 2.1.

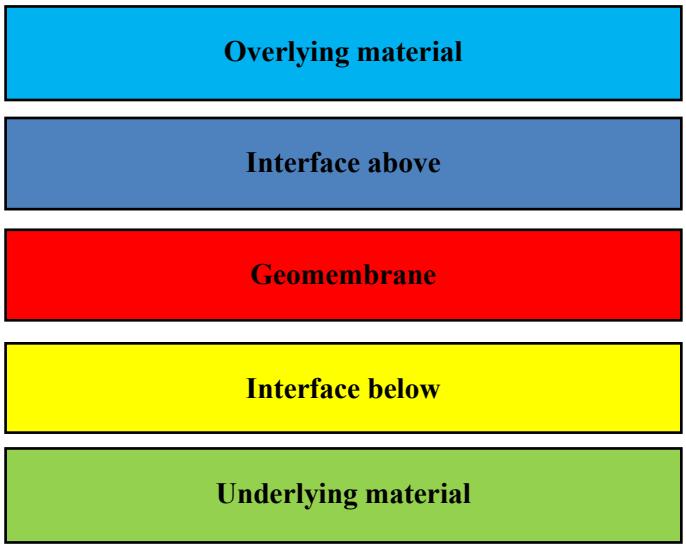

Figure 2.1: Concept of the 'liner’ element

2.2.3 'geogrid' versus 'liner' element

The pre-defined 'geogrid' element in FLAC^{3D} (Fig. 2.2) has the following basic properties:

- Density and thickness
- Elastic isotropic or anisotropic material behavior
- Thermal expansion
- Cohesive contact between geogrid and the material on both sides
- Frictional bond between geogrid and material on both sides
- Shear stiffness between geogrid and material on both sides

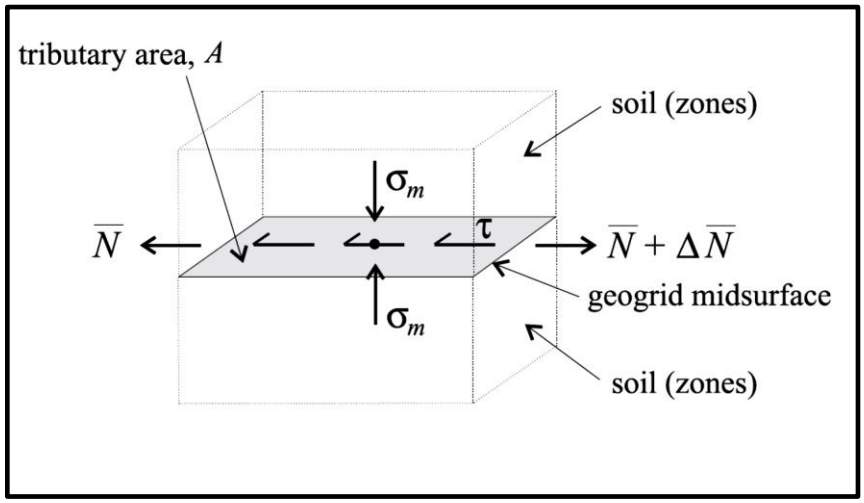

Figure 2.2: Illustration of the 'geogrid' element (Itasca 2017)

The 'geogrid' element itself is based on a CST (Constant-Strain-Triangle) element without bending stiffness and can be placed in a mesh (volume elements) as desired. The advantage of this element is the easy handling and trouble-free installation in any mesh. A disadvantage for the task at hand is, in particular, the fact that identical properties act on both sides of the geogrid.

An alternative to the 'geogrid' element is the developed 'liner' element (Fig. 2.1). The 'liner' element is a DKT-CST (Discrete-Kirchhoff-Triangle- Constant-Strain-Triangle) element and can, in principle, also represent bending stiffness. In order to use this element as a geomembrane, it must be assigned with interfaces on both sides. This makes it possible to simulate different interactions with the over- and underlying material. This proposed 'liner' element has the following basic properties:

- Density and thickness
- Elastic isotropic or anisotropic material behavior

- Thermal expansion
- Cohesive and frictional contact between geomembrane and overlying material
- Cohesive and frictional contact between geomembrane and underlying material
- Shear and normal stiffness between geomembrane and overlying material
- Shear and normal stiffness between geomembrane and underlying material
- Tensile strength between geomembrane and overlying material
- Tensile strength between geomembrane and underlying material

Both 'geogrid' and 'liner' element initially respond purely elastic. In order to simulate the failure of the geomembrane itself, additional functionalities have to be implemented: the maximum tensile stresses in the geotextile have to be monitored, and when limit values are reached, the corresponding zones of the geotextile have to be set as cracked (deleted). These functionalities have been implemented via the internal program language FISH.

2.2.4 Verification of 'liner' element

The objective is to develop a simulation strategy to investigate and verify the interaction between the geomembrane and surrounding material by using a simple model considering practical relevant scenarios. For this purpose, the following aspects have to be considered:

- Large relative displacements between the geomembrane and under- and overlying material
- Large strain of the geomembrane
- Tensile failure of the geomembrane (tearing)
- Different superimposed loads
- Different parameter combinations for interaction between geomembrane and under- and overlying material

A pull-out test is best suited to proof the functionality, as it is standardly used for the investigation of the interaction between geomembrane and soil in the laboratory. Pull-out tests are carried out in large shear box devices, where soil material is placed in the lower shear box, the geomembrane in between the two shear boxes, and soil material again in the upper shear box. Normal stress can be applied to the upper shear box in the vertical direction. The geomembrane

can be fixed at one edge or lie between the soil layers freely. Traction is applied at one edge, and at least traction force and pull-out distance are measured. In addition, other quantities such as the internal deformation of the geomembrane can be monitored. This test is used to determine the interaction between the geomembrane and the soil material, particularly to investigate the frictional bond between the geomembrane and the soil.

The interaction between the geomembrane and the material above as well as between the geomembrane and the material below includes 5 phases (initially assuming that the geomembrane does not crack, i.e., the tensile strength of the geomembrane is not exceeded):

- 1st phase: pure elastic reaction (expansion of the geomembrane and shear deformation in the geomembrane/ overlying material or geomembrane/ underlying material interfaces).
- 2nd phase: reaching the limit state in one of the two interfaces
- 3rd phase: further elastic reaction in one of the interfaces and plastic reaction in the other (frictional sliding)
- 4th phase: reaching the limit state also in the second interface
- 5th phase: friction sliding in both interfaces

These 5 phases cover all possible forms of shear deformation. In addition, tensile failure can occur, at least theoretically. This is also handled by defining a tensile strength in both interfaces, although it is normally not relevant from the practical point of view.

The numerical model should be able to reproduce this behavior. Therefore, extensive testing as described below was performed using the 'liner' element and for comparison also the 'geogrid' element. The interface functionality contains automatic contact cancellation and reestablishment. When testing the failure of the geomembrane, the following 3 phases shall be evident:

- Linear or bi-linear behavior in terms of tensile stress versus pull-out distance until the tensile strength is reached in at least one element of the geomembrane
- Stepwise failure of the geomembrane elements in which the tensile strength is reached up to complete rupture
- Stress relief in the ruptured geomembrane and retention of residual stress according to a surcharge and frictional contact

For the tests described below, different parameters regarding the interface properties and the surcharge are selected to test the functionality of the 'geogrid' and 'liner' elements. The choice of parameters regarding stiffness and friction angle cover very wide ranges including the practical, relevant parameters not only valid for geomembranes but for geotextiles in general.

The tests can be considered successful if:

- The five above mentioned phases of the interaction between the geotextile and the material on both sides can be reproduced
- The dependence on the superimposed load is correctly represented
- The cracking of the geotextile when tensile strength is exceeded is correctly represented

Tab. 2.1 shows an overview of the individual simulations performed to verify the functionality.

Table 2.1: Overview of verification tasks

Case	**Geomembrane** **G: 'geogrid' - element L: 'liner' - element**
A	G: Variation of interface stiffness
B	G: Variation of interface friction angle
C	L: Variation of interface stiffness
D	L: Variation of interface friction angle
E	Compare G element and L element
F	L: Different ratios of normal stiffness to shear stiffness and different stiffness in the two interfaces
G	L: like F, but with higher friction angle
H	L: Tensile strength and failure of geotextile alone without interaction with the surrounding material
I	L: like L, but with interaction with surrounding material as well as with load
J	L: like I, but with a wide range of potential failure in the geomembrane

Fig. 2.1 illustrates the structure of the 'liner' element, where:

- The geotextile is represented by special shell elements (= liner elements),
- The two interfaces are represented by special interface elements with automatic contact detection and
- The over- and underlying materials are represented by volume elements with arbitrary material laws and arbitrary layer structure.

The numerical simulations of the pull-out tests are performed with a model as shown in Fig. 2.3 using FLAC^{3D} (Version 6.0). Initially, both interfaces at the 'geogrid' and 'liner' elements are assigned identical with adequate values, i.e., parameters are identical on both sides of the geomembrane. The geomembrane is pulled in the X-direction until pure elastic interaction between geomembrane and over- and underlying material is exceeded. Failure of the geomembrane itself is excluded at present.

a)

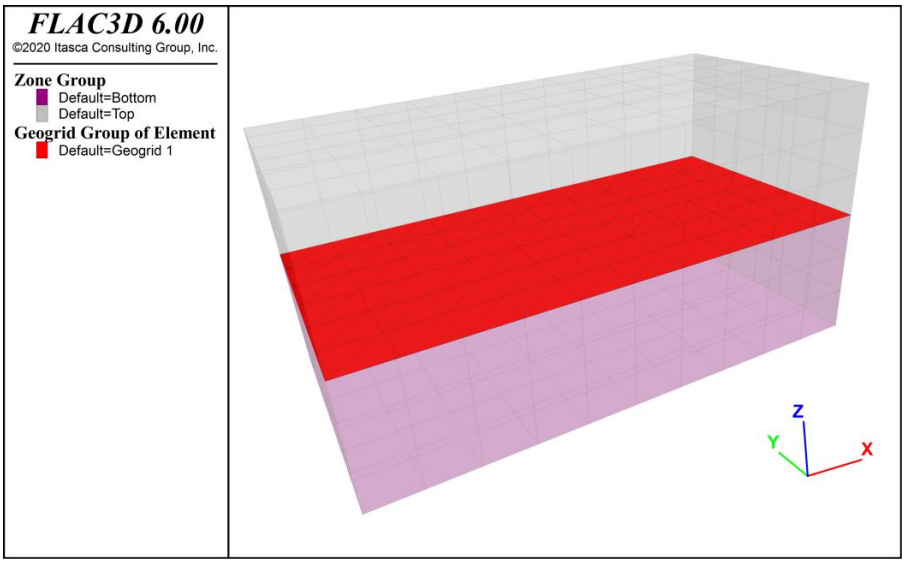

b)

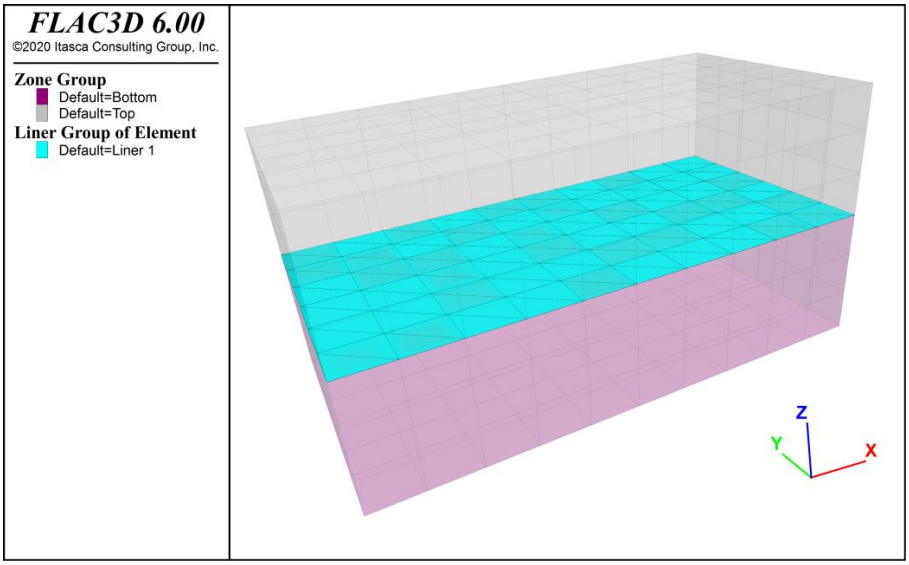

Figure 2.3: Numerical models for pull-out test.
a) 'liner' element, *b)* 'geogrid' element

The external model dimensions are 1.0 m x 0.5 m x 0.5 m. The geomembrane is installed in the center. The left edge of the model and the bottom are fixed in the normal direction. The geomembrane is also fixed at the left edge. The geomembrane is pulled horizontally at the right

edge in the right (x) direction. The parameters of the elastic material above and below are bulk modulus $K = 12 \cdot 10^6$ Pa, shear modulus $G = 5.77e \cdot 10^6$ Pa (corresponding to $E = 15$ MPa and $\nu = 0.3$), density $\rho = 1950$ kg/m^3. The tensile strength of the interface was always set to zero. In addition to the pure gravitational loading, the following additional vertical imposed loads are assumed in the simulated tests: 20 kPa and 40 kPa.

Simulation case A

The 'geogrid' element is used for case A. Fig. 2.4 shows the results of the pull-out tests for different parameter combinations in terms of shear stress (pull-out force divided by geomembrane area) versus pull-out distance. The effect of different contact shear stiffness (see the slope of the curves) and the effect of different imposed loads (see the maximum value of shear stresses that can be transmitted) becomes obvious.

Table 2.2: Parameters for 'geogrid' element for case A

Parameter		Uniaxial geogrid	Biaxial geogrid	Woven geotextile
E-Modul, Pa	Surrounding Material	$2.6 \cdot 10^{10}$	$2.6 \cdot 10^{10}$	$2.6 \cdot 10^{10}$
Poisson's ratio		0.33	0.33	0.33
Cohesion, Pa	Interface	0	0	0
Friction angle, ^{o}		30	30	30
Shear stiffness, Pa/m		$1.5 \cdot 10^6$	$2.5 \cdot 10^6$	$1 \cdot 10^6$

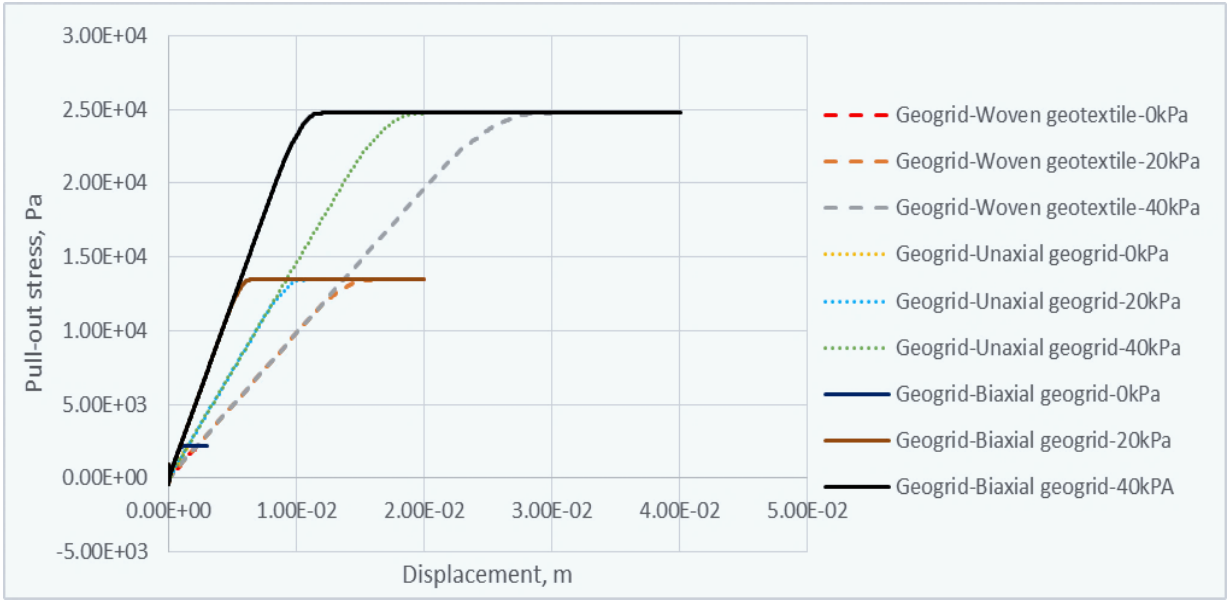

Figure 2.4: Pull-out stress (Pa) versus displacement (m) for 'geogrid' element according to Tab. 2.2

Simulation case B

Case B is based on case A but considers the effect of the interface friction angle with otherwise identical parameters. Fig. 2.5 shows the results of the pull-out tests in terms of shear stress (pull-out force divided by geotextile area) versus pull-out distance for 40 kPa surcharge load. At about 90% of the final failure load in the interface, slight nonlinearity becomes visible in all tests (particularly visible because of very large displacements in the interface), indicating initial local attainment of shear strength of individual interface elements (very local transition from pure elastic response to frictional sliding).

Table 2.3: Parameters for 'geogrid' element for case B

Parameter		Woven geotextile			
E-Module, Pa	Subsoil	$2.6 \cdot 10^{10}$			
Poisson's ratio		0.33			
Cohesion, Pa	Geotextile	0			
Friction angle, °		10	20	30	40
Shear stiffness, Pa/m		$1 \cdot 10^{6}$			

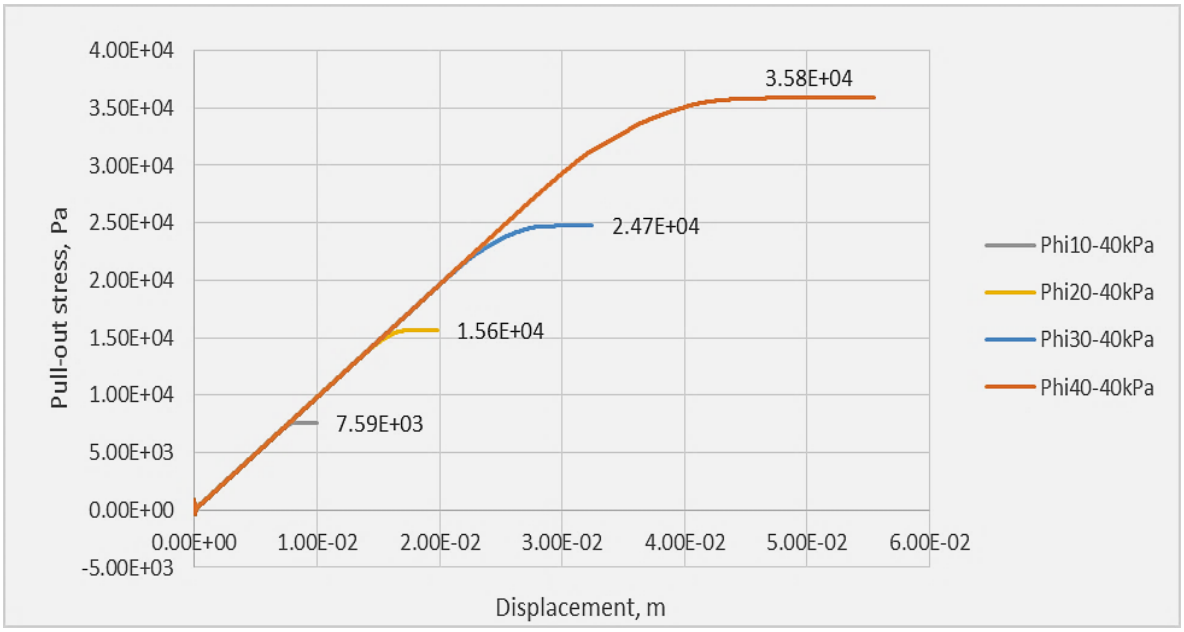

Figure 2.5: Pull-out stress (Pa) versus displacement (m) for 'geogrid' element according to Tab. 2.3

Simulation case C

This case is performed in analogy to case A, but the 'geogrid' element is replaced by the 'liner' element. Tab. 2.4 shows the parameters used. The interface properties on both sides are identical.

Fig. 2.6 shows the results of the pull-out tests in terms of shear stress (pull-out force divided by geotextile area) versus pull-out distance. According to Tab. 2.4, the selected parameters correspond to typical values of various geotextiles (woven geotextile, uniaxial geogrid, and biaxial geogrid). The imposed loads are 0, 20, and 40 kPa, with gravitational loading always acting in addition.

Table 2.4: Parameters for 'liner' element for case C

Parameters		Woven geotextile	Uniaxial geogrid	Biaxial geogrid
E-Module, Pa		$2.6 \cdot 10^{10}$	$2.6 \cdot 10^{10}$	$2.6 \cdot 10^{10}$
Poisson's ratio of geotextile		0.33	0.33	0.33
Thickness of geotextile, m		0.003	0.003	0.003
Cohesion of interface, Pa	same for both sides	0	0	0
Shear stiffness of interface, Pa/m		$1 \cdot 10^{6}$	$1.5 \cdot 10^{6}$	$2.5 \cdot 10^{6}$
Friction angle of interface, °		29	29	29
Normal stiffness of interface, Pa/m		$1 \cdot 10^{6}$	$1.5 \cdot 10^{6}$	$2.5 \cdot 10^{6}$

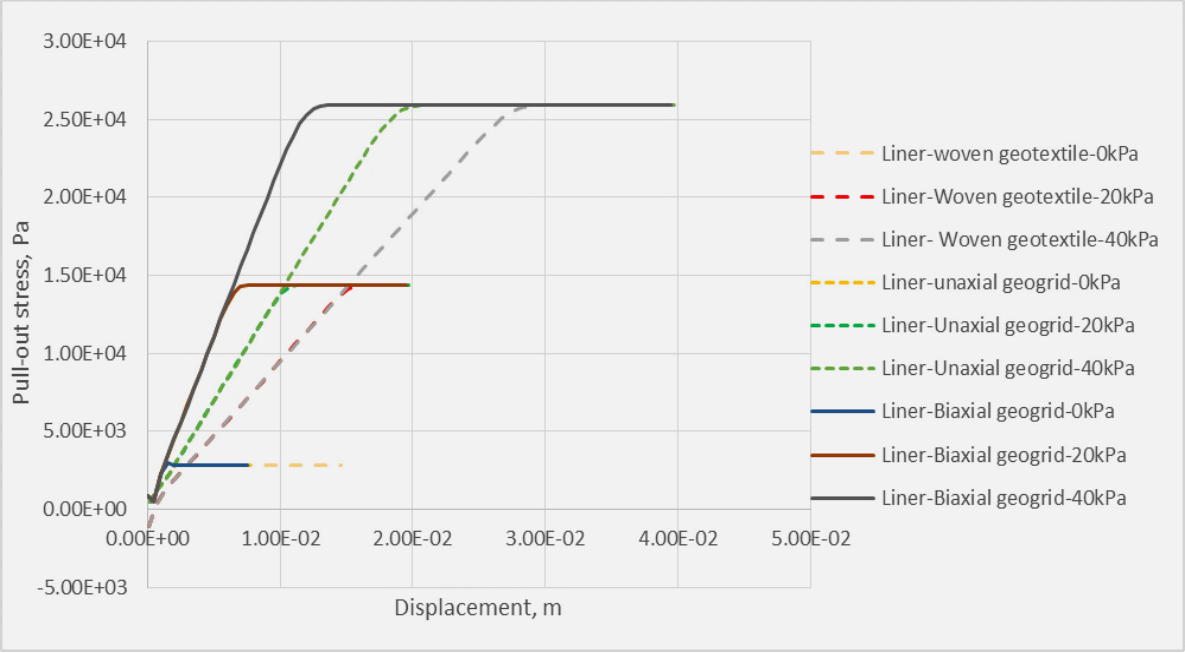

Figure 2.6: Pull-out stress (Pa) versus displacement (m) for 'liner' element according to Tab. 2.4

Simulation case D

Case D is based on case C and focuses on different interface friction angles with otherwise identical parameters. The interface properties are the same on both sides. Fig. 2.7 shows the

results of the pull-out tests in terms of shear stress (pull-out force divided by geotextile area) versus pull-out distance. The applied load is 40 kPa in each case.

Table 2.5: Parameters for 'liner' element for case D

Parameter		**Woven geotextile**			
E-Module, Pa		$2.6 \cdot 10^{10}$			
Poisson's ratio of geotextile		0.33			
Thickness of geotextile, m		0.003			
Cohesion of interface, Pa	same for both sides	0			
Shear stiffness of interface, Pa/m		$1 \cdot 10^6$			
Friction angle of interface, °		10	20	30	40
Normal stiffness of interface, Pa/m		$1 \cdot 10^6$			

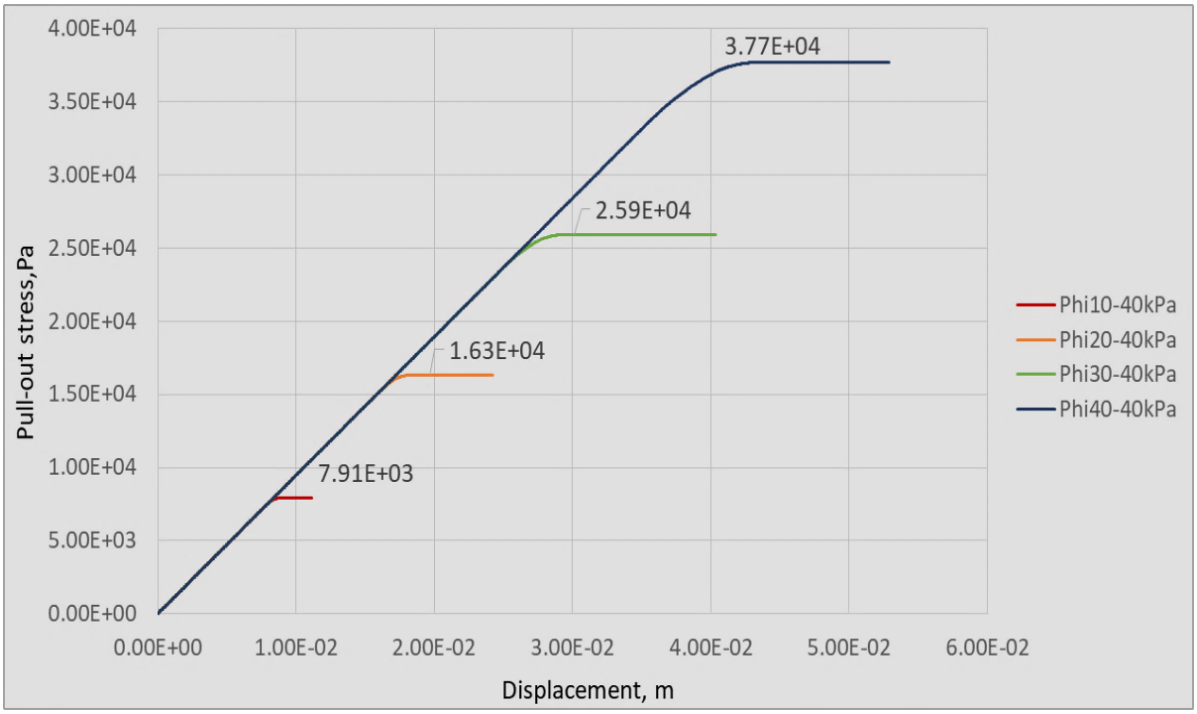

Figure 2.7: Pull-out stress (Pa) versus displacement (m) for 'liner' element according to Tab. 2.5.

Simulation case E

Case E compares 'geogrid' and 'liner' elements with identical parameters for the geotextile and interface parameters. Tab. 2.6 shows the parameters used. Fig. 2.8 shows the pull-out test results in terms of shear stress (pull-out force divided by geotextile area) versus pull-out distance. Both approaches show similar behavior, with the 'geogrid' element providing slightly lower pull-out forces or stresses.

Table 2.6: Parameters used for comparison between 'geogrid' and 'liner' elements

Parameter	'liner' element		'geogrid'- element
E-Module, Pa	$2.6 \cdot 10^{10}$		$2.6 \cdot 10^{10}$
Poisson's ratio of geotextile	0.33		0.33
Thickness of geotextile, m	0.003		0.003
Cohesion of interface, Pa	0	same for both sides	0
Shear stiffness of interface, Pa/m	$1 \cdot 10^6$		$1 \cdot 10^6$
Friction angle of interface, °	29		29
Normal stiffness of interface, Pa/m	$1 \cdot 10^6$		--

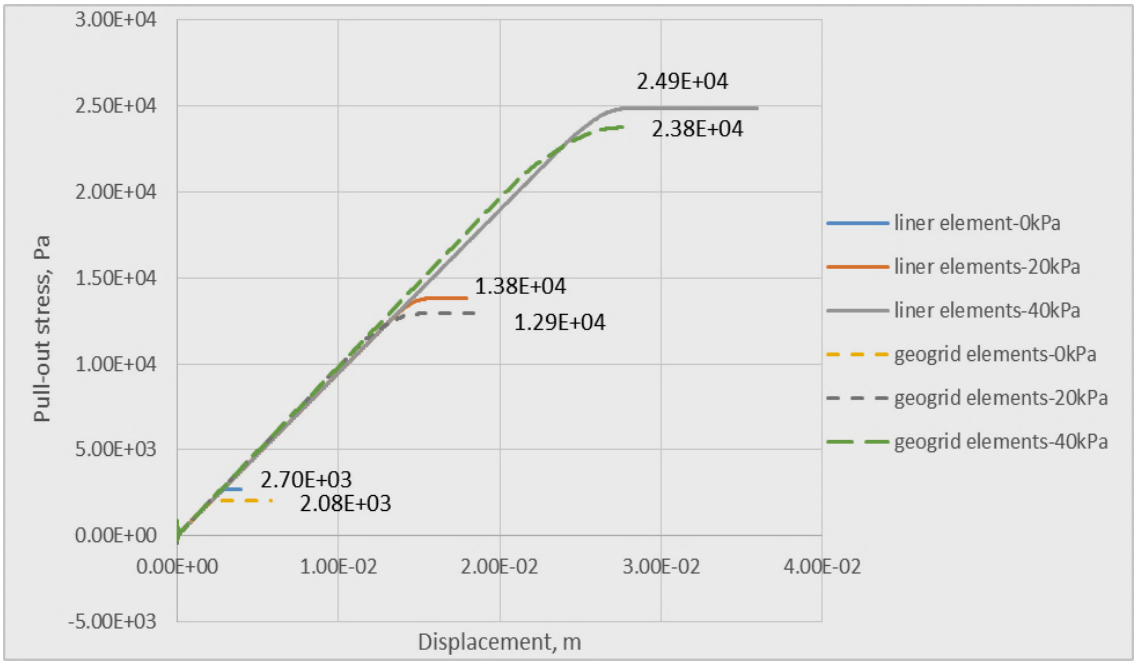

Figure 2.8: Pull-out stress (Pa) versus displacement (m) for 'geogrid' and 'liner' elements according to Tab 2.6.

Table 2.7: Comparison of limit shear stresses in pull-out tests under superimposed loads of 0, 20, and 40 kPa.

	Theoretical value	Value using geogrid element	Value using liner element
τ_{0kPa}, Pa	$2.70 \cdot 10^3$	$2.08 \cdot 10^3$	$2.70 \cdot 10^3$
τ_{20kPa}, Pa	$1.38 \cdot 10^4$	$1.29 \cdot 10^4$	$1.38 \cdot 10^4$
τ_{40kPa}, Pa	$2.49 \cdot 10^4$	$2.30 \cdot 10^4$	$2.49 \cdot 10^4$

As Tab. 2.7 shows, the 'geogrid' element delivers shear resistances that are somewhat too low. The proposed 'liner' element provides exactly the theoretically expected value. It should be noted that the 'geogrid' element and the 'liner' element work completely differently. The former is

inserted into the grid and interacts with the zones via special averaging algorithms, leading to small errors. The 'liner' element is mapped exactly via completely formed elements and assigned nodes in each case and, therefore, provides greater accuracy. Nevertheless, from a practical point of view, the 'geogrid' element is also acceptable and applicable (error of about 10% or less).

Simulation case F

This case considers the 'liner' element with different properties for the two interfaces. The friction angle in both interfaces is 10°, but shear and normal stiffness differ according to Tab 2.8. The other parameters correspond to Tab. 2.6.

Table 2.8: Interface stiffness values for 'liner' element for test F

k_n/k_s	k_n, Pa/m		k_s, Pa/m	
	Side 1	**Side 2**	**Side 1**	**Side 2**
1	10^8	10^5	10^8	10^5
5	$5 \cdot 10^8$	$5 \cdot 10^5$	10^8	10^5

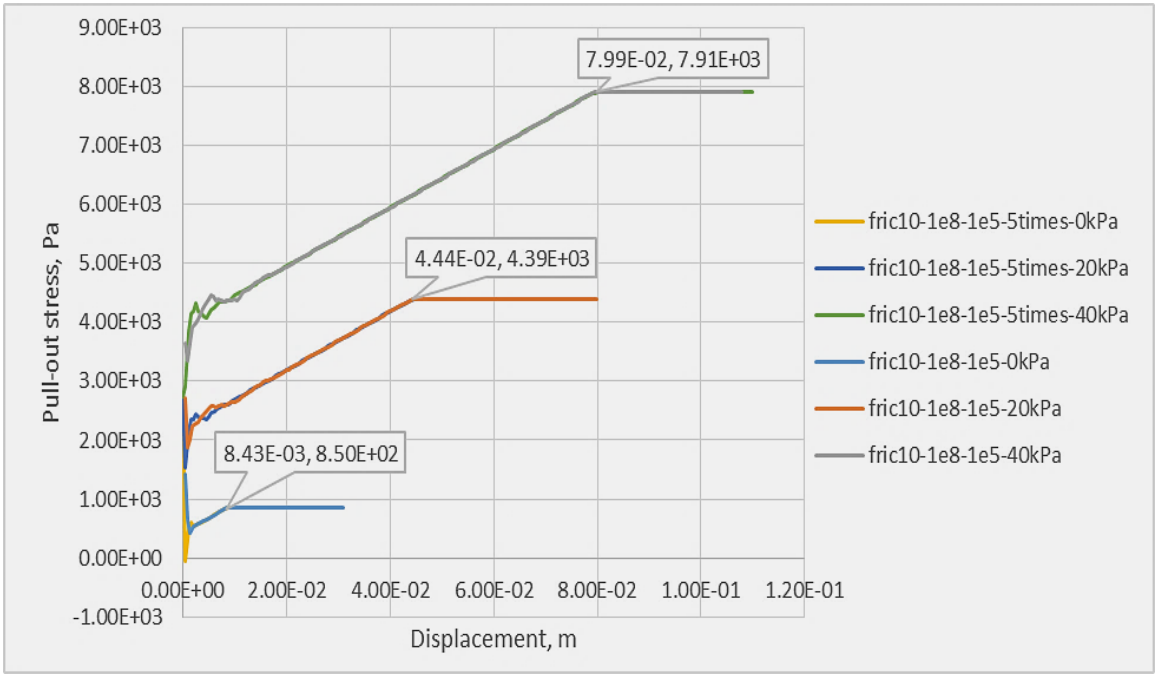

Figure 2.9: Pull-out stress (Pa) versus displacement (m) for 'liner' elements according to Tab. 2.8 and 2.6 (interface friction angle of 10° on both sides)

Fig. 2.9 shows that the pull-out resistance for 10° (friction angle) corresponds to that already documented in Fig. 2.5 and 2.6. On the other hand, a bi-linear behavior can be seen up to the failure limit. The reason is the strongly different shear stiffness in the interfaces on both sides of

the geomembrane. The initial extremely high stiffness is determined by the effect of both interface stiffnesses (but especially the one with a higher value). The first buckling point marks the point where the limit stress in the stiffer interface is reached, and friction-controlled shear resistance occurs in this interface. In comparison, the softer interface still reacts elastically until the second buckling point is reached. Then the limit stress is also reached in the second interface, and friction-controlled shear resistance is now active in both interfaces.

These simulations consider extreme stiffness differences to identify the onset of failure and to prove the robustness of the algorithm. The normal stiffness has no significant influence, but the shear stiffness is decisive. An increase by a factor of 5 in the normal stiffness does not influence the shear behavior, as shown in Fig. 2.10. The additionally applied normal stresses (20 and 40 kPa) lead to increased shear resistances (= normal stress x friction coefficient), as shown in Fig. 2.9. The fluctuations partially visible in the curves (see, e.g., Fig. 2.9 in the initial phase) are due to the choice of the simulation time step. They can be eliminated without problems if the time step is reduced at the cost of the computation time.

Simulation case G

This case is identical to case F except for the interface friction angles, which are now 40°. As expected, the final pull-out resistance is correspondingly higher compared to test F.

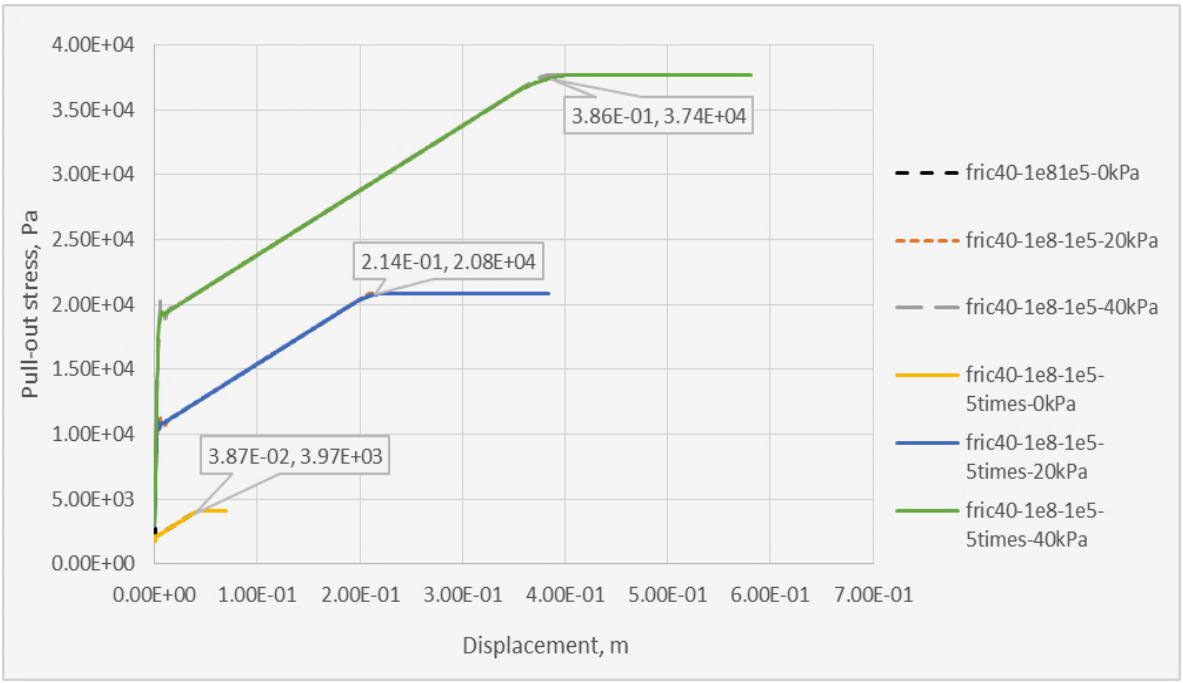

Figure 2.10: Pull-out stress (Pa) versus displacement (m) for 'liner' elements according to Tab. 2.8 and 2.6 (interface friction angle of 40° on both sides)

Simulation case H

This case simulates the tearing of the geomembrane by deactivating liner elements during the pull-out test and the corresponding interface elements. However, the remaining parts of the geomembrane are still active. The stresses in the 'liner' element are monitored, and principal stresses are determined and compared with the tensile strength of the geomembrane. When a zone of the 'liner' element reaches the tensile strength of the geomembrane, it is deleted.

To test this algorithm, a model with the following properties is used. The geomembrane has a thickness of 30 mm and is reduced to 10 mm in one single row of elements perpendicular to the tensile load direction (see Fig. 2.11). The geomembrane is pulled in the x-direction with a constant speed, and at the opposite edge, the geomembrane is fixed. This test automatically results in the highest tensile stresses in the area with reduced thickness, i.e., these elements should fail and should be deleted according to the algorithm when the tensile strength (here $1e^8$ Pa) is reached. Fig. 2.11 to 2.15 illustrate this process. The residual stresses visible in Fig. 2.15 represent numerical noise (they are about seven orders of magnitude smaller and would drop to almost zero with ongoing computation time).

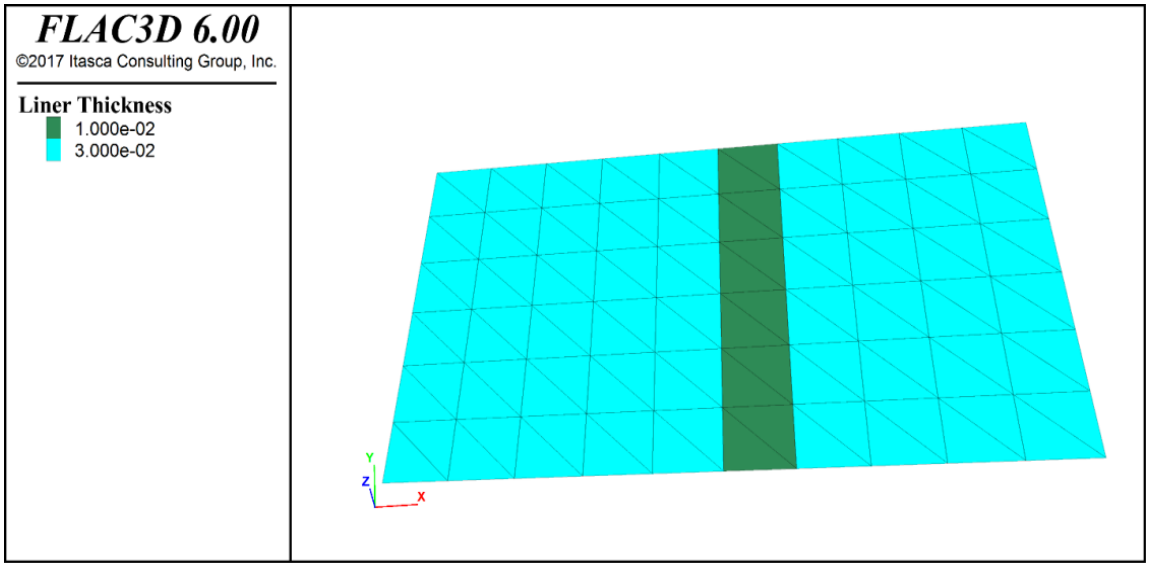

Figure 2.11: Geomembrane with specification of thickness (m)

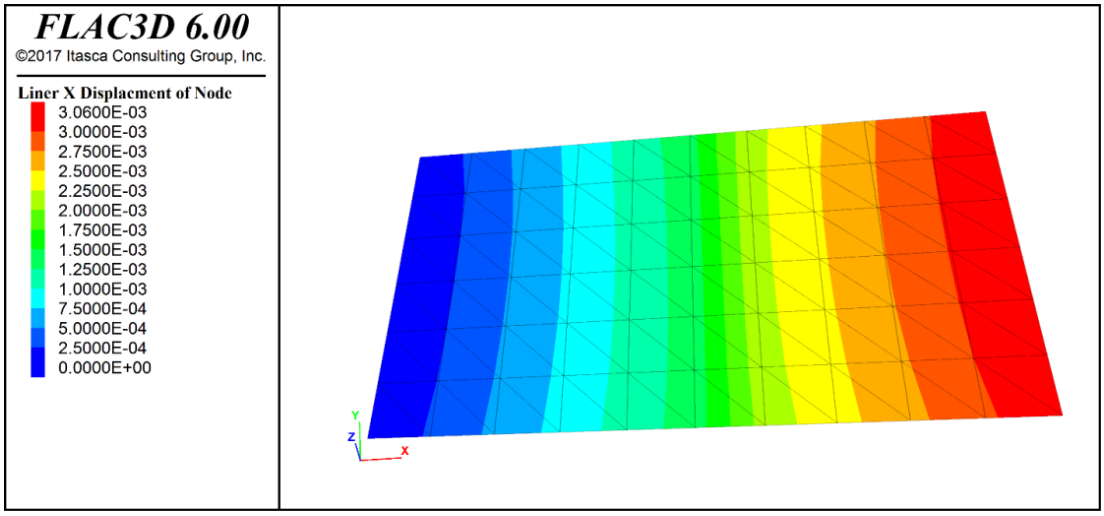

Figure 2.12: Geomembrane with displacement field in x-direction (m) during tensile test

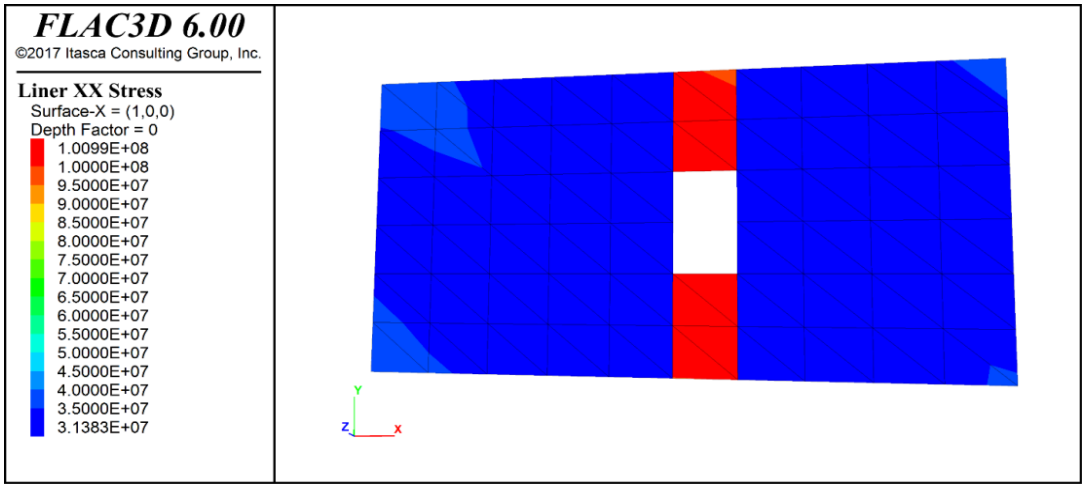

Figure 2.13: Tensile stresses (Pa) in geomembrane in the initial state of rupture (limit stress of 10^8 Pa is reached) during the tensile test

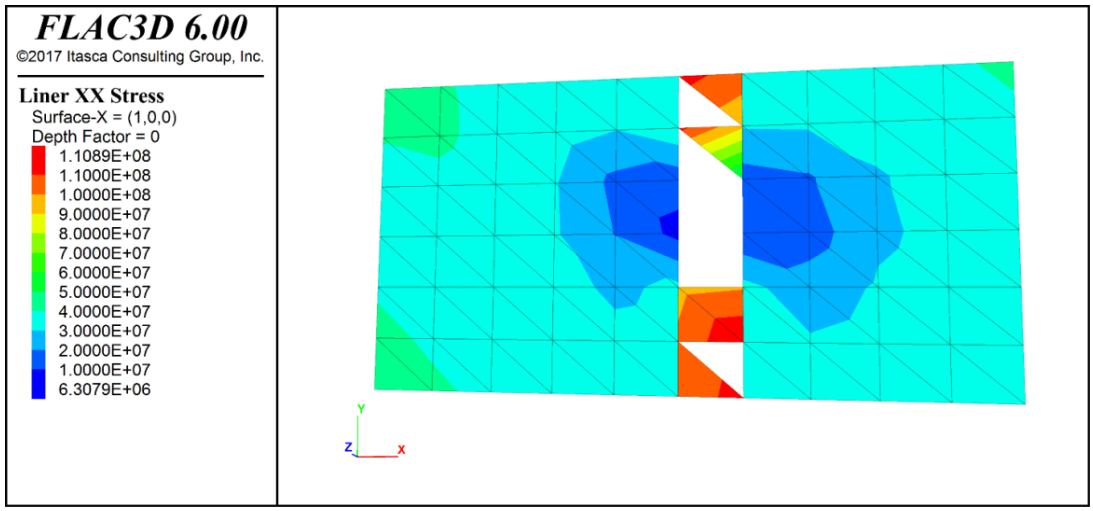

Figure 2.14: Tensile stresses (Pa) in geomembrane in the state of rupture (limit stress of 10^8 Pa is reached) during the tensile test

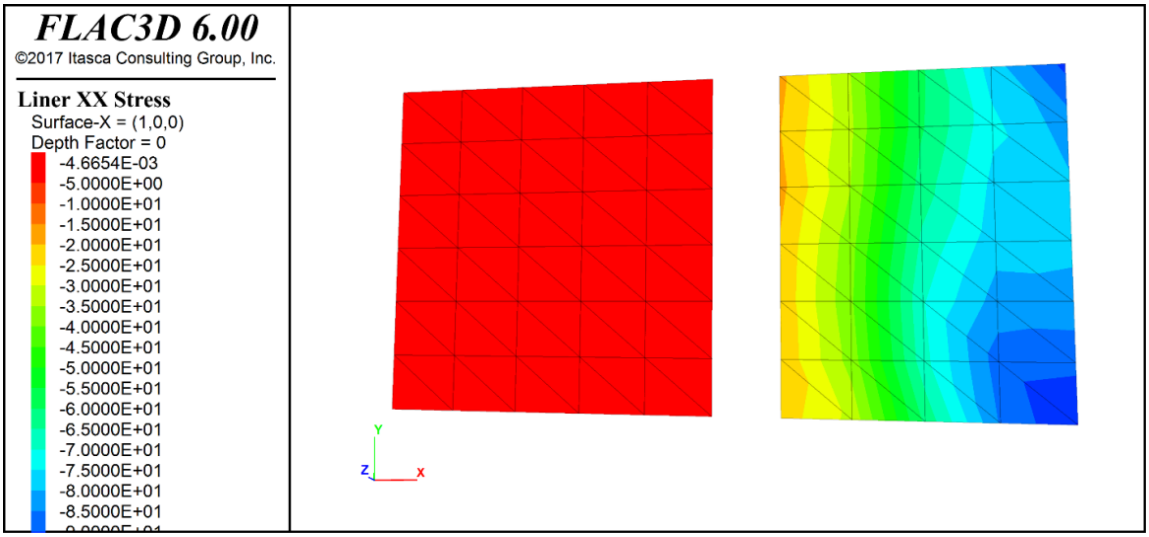

Figure 2.15: Tensile stresses (Pa) in geomembrane immediately (directly) after complete rupture during the tensile test

Simulation case I

This case is based on case H but considers the interaction on both sides of the geomembrane. The latter acts gravitationally and takes into account a vertical surcharge load of $4 \cdot 10^5$ Pa, which exceeds the gravitational effect. There is a purely frictional contact with a friction angle of 10° on both sides of the geomembrane. Fig. 2.16 to 2.21 illustrate the model behavior. The geomembrane fails again when the limit stress of 10^8 Pa is reached. If the geomembrane ruptures and the corresponding elements are deleted, the load is transferred from the waste dump via the remaining interface elements into the underlying material.

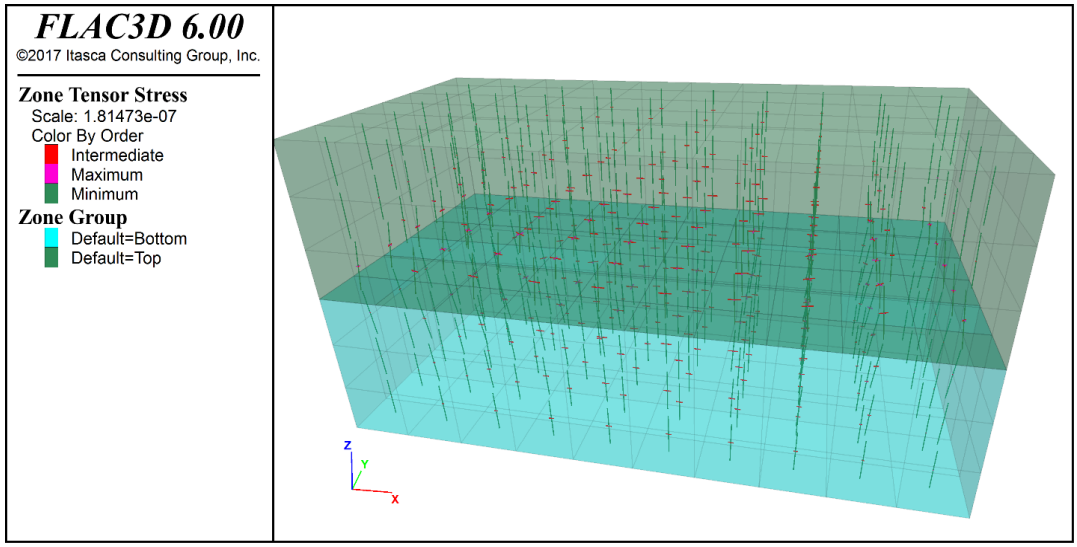

Figure 2.16: Initial stress state in model with installed geomembrane before start of tensile test

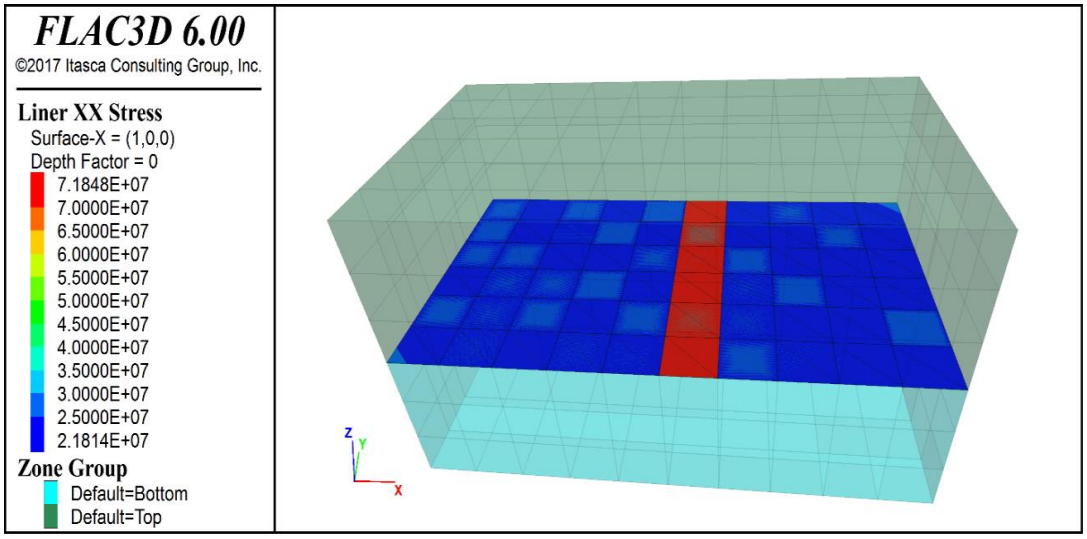

Figure 2.17: Tensile stress (Pa) during the tensile test before rupturing of the geomembrane

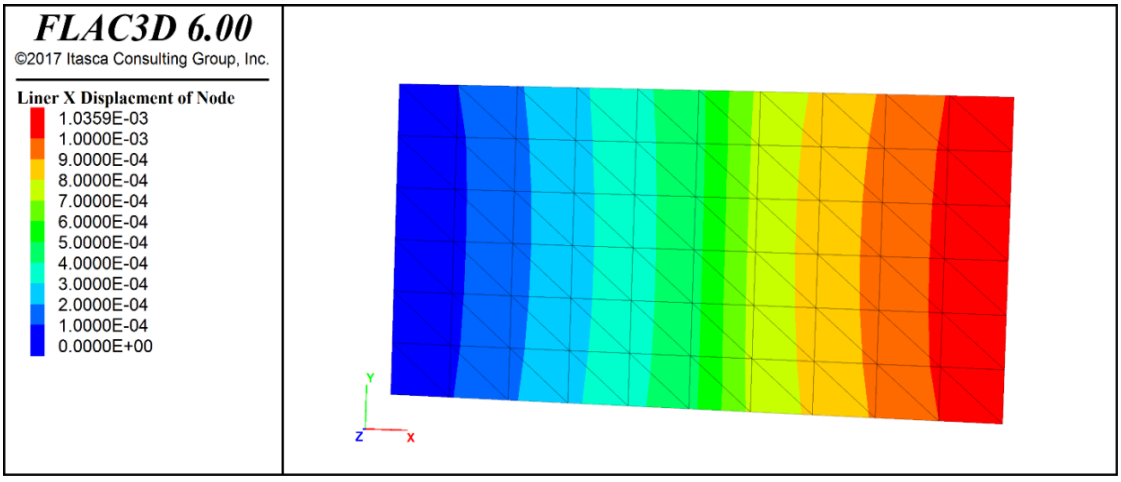

Figure 2.18: Displacement field (m) of geomembrane during the tensile test before rupture

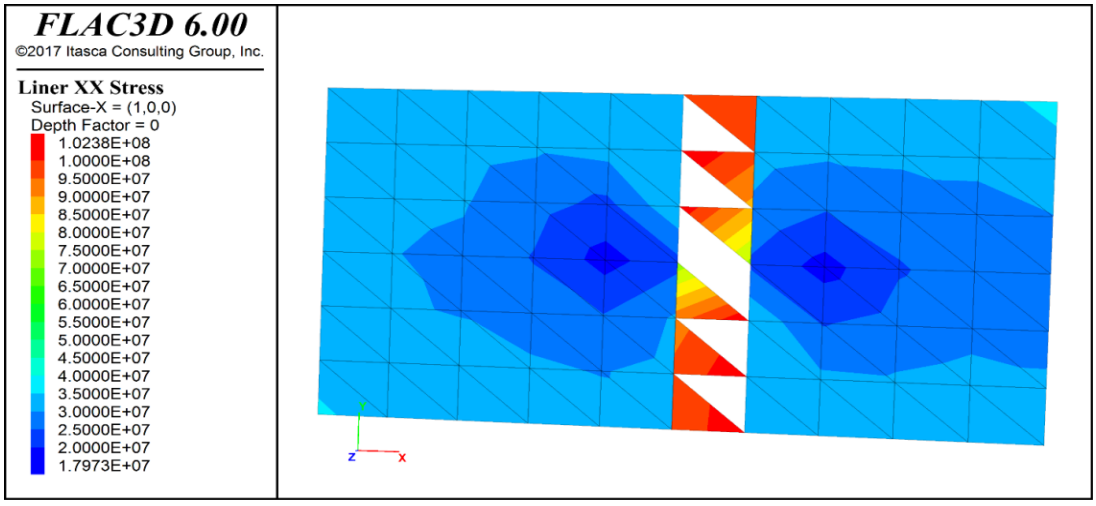

Figure 2.19: Tensile stress (Pa) in geomembrane during the tensile test at the time of rupture

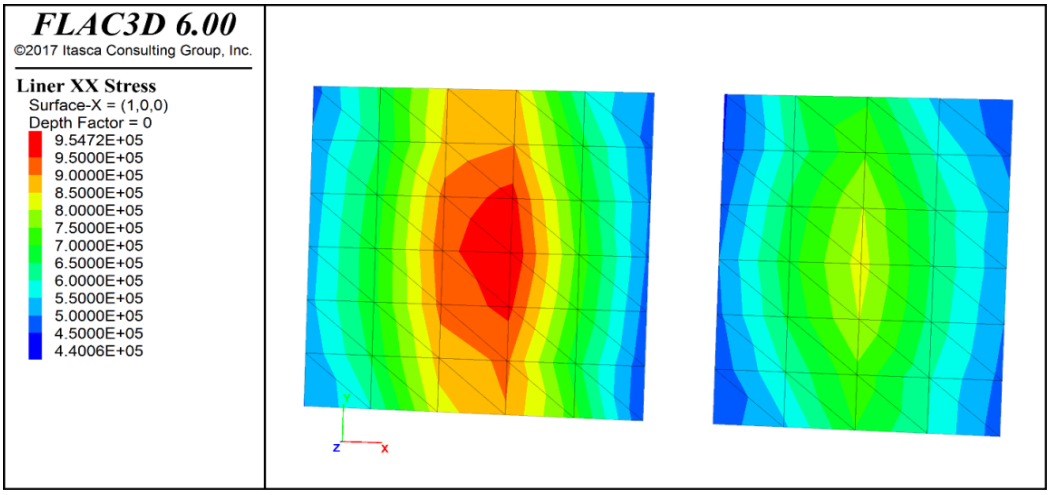

Figure 2.20: Tensile stress (Pa) in geomembrane after rupture during the tensile test

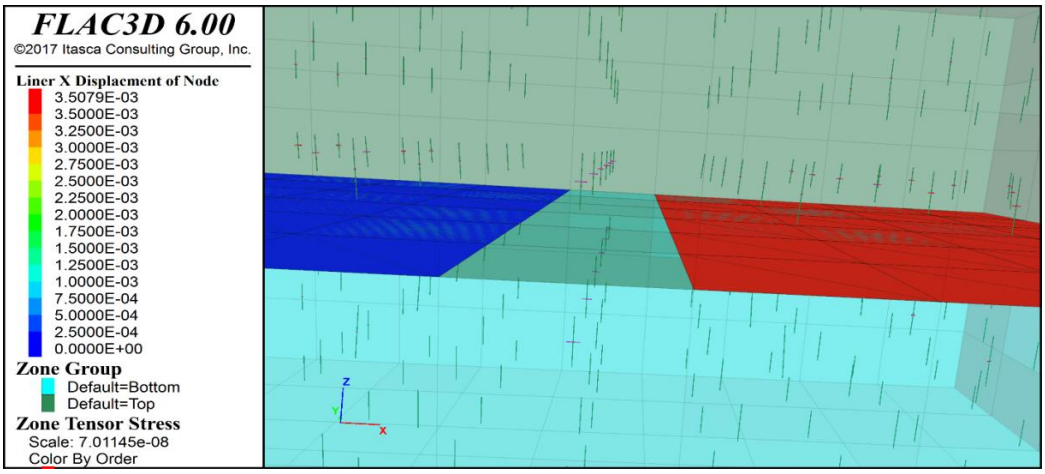

Figure 2.21: Stress state (principal stresses) and displacements of the geomembrane (m) after rupture during the tensile test

This model was calculated with restrained lateral strain and with unrestrained lateral strain. In both cases, the correct (almost identical) behavior of the geomembrane was recorded. The sequence of images shown above is taken from the model without restrained lateral expansion. As Fig. 2.20 shows, residual tensile stresses remain in the geomembrane because the frictional bond and the surcharge prevent complete relaxation. The right part of the cracked geomembrane is moved further to the right due to the applied constant pull-out speed and therefore has larger displacement values. In contrast, the left part partly moves back until the residual shear stress is in equilibrium with the frictional resistance.

Simulation case J

Case J is analog to case I, but the strip with reduced thickness was extended to a width comprising 4 or 2 elements. In this case, the rupture also develops only along one element width

(see Fig. 2.22 and 2.23). The sequence of events is as follows: first, one of the zones fails, followed by stress redistributions, which affect neighboring zones and bring them to the limit state. This process continues - as a failure propagation process - until no element reaches the limit state anymore. In this test, again, a constant pull-out speed acts in the x-direction.

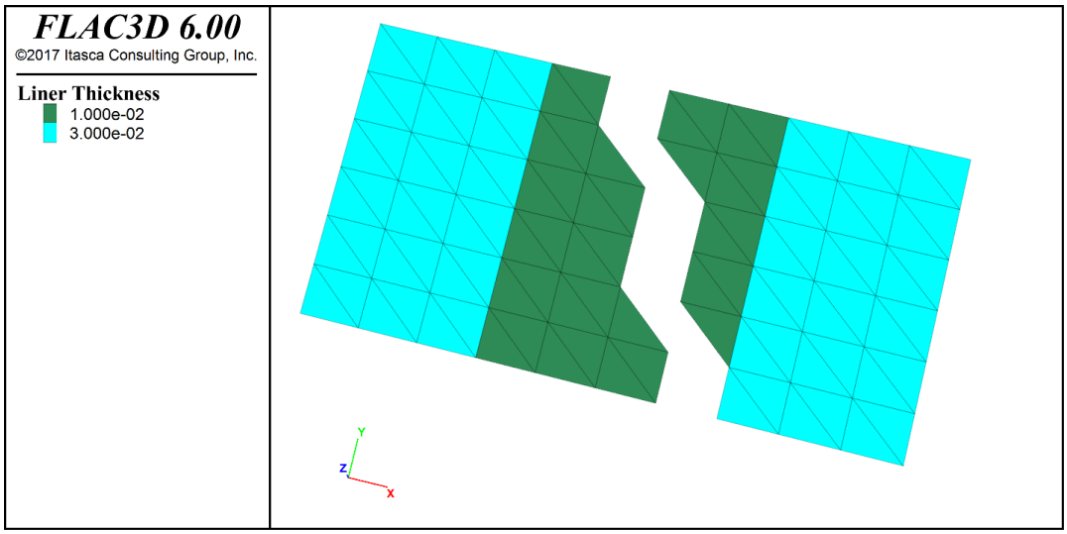

Figure 2.22: Geomembrane at the state of rupture during tensile test

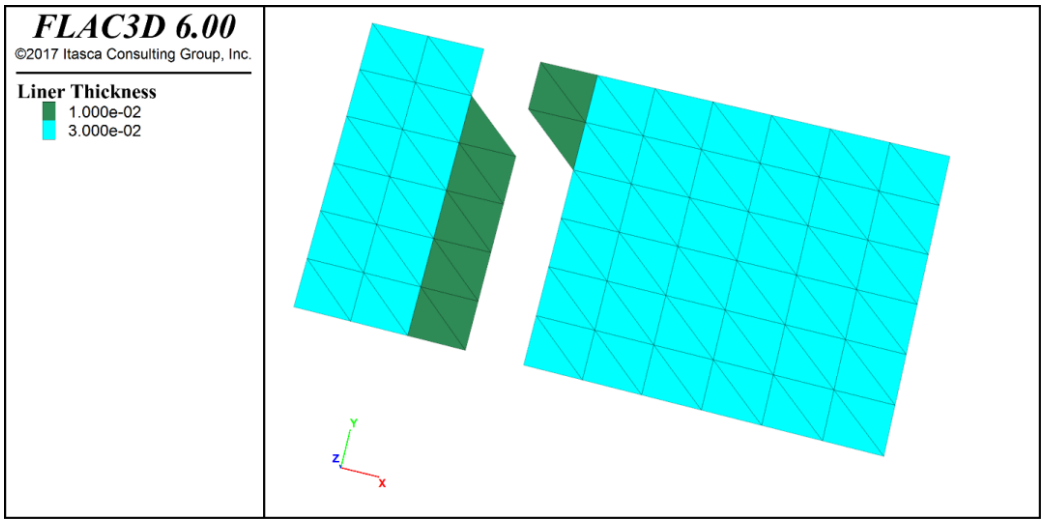

Figure 2.23: Geomembrane at the state of rupture during tensile test

2.2.5 Conclusions

The 'liner' element shows a robust and plausible behavior for a wide range of parameters. The 'liner' element has the following potential features:

- Elastic interaction with over-and underlying material
- Detachment from the over- and underlying material

- Different frictional sliding at interfaces above and below the geomembrane
- Cracking of the geomembrane in case of overloading
- Resistance-free compression under compressible loading

The interaction of the geomembrane ('liner' element) with the over-and underlying material has two phases: an elastic and a plastic (frictional) reaction. The geomembrane itself reacts primarily purely elastic. When the tensile strength is exceeded, the corresponding elements are deleted and thus become ineffective. The degree of utilization of the geomembrane as the ratio of maximum tensile stress to tensile strength can be monitored during the simulation, evaluated, and displayed at any time.

Cohesion and dilatancy angles can be set to zero as a first approximation. To represent higher static friction than sliding friction, one can define an initial cohesion that is set to zero when the shear strength is exceeded (analog to the strain-softening behavior) or reduce the friction angle as a function of shear displacement.

How can the required parameters of the geomembrane and the interfaces be determined? The parameters of the geomembrane itself are available as product information (additional tests regarding tensile strength may be required if cracking has to be included in the considerations). The parameters of the interfaces can be determined by performing large shear tests. Depending on the type of device, either pull-out tests can be performed in complete analogy to the numerical ones or classical shear tests with a fixed geomembrane. By incorporating different materials, the corresponding parameter combinations can be determined. Surcharge load can be considered in form of multi-stage tests or in the form of different individual tests. Since the surcharge level may vary strongly (a few kPa up to several MPa) for different geotechnical projects, it may be necessary to use soil and rock mechanical devices in combination.

From the computational point of view, it should be noted that:

- The shell elements generally work in a local coordinate system, i.e., additionally implemented functions (e.g., query after exceeding the tensile strength) require a transformation of the tensor values. This process is computationally intensive producing additional computational time. In the simulations documented in this report, this was done in each case.

- After deleting the geotextile elements (tensile failure), a new interface must be automatically placed at this location if the crack width is more than one element width. This algorithm has been implemented and tested, but may not be necessarily activated (saving computational time) since the crack is nearly always restricted to a width of one element only.

In the current implementation, the visco-elasto-plastic behavior of the geomembrane itself cannot be simulated. However, the degree of utilization can be determined and cracking is duplicated by deleting 'liner' elements.

Since the dimensioning of a geomembrane must be such that cracking is avoided, it may be sufficient to monitor only the utilization factor (maximum tensile stress / tensile strength) for each element. The reciprocal value of the utilization factor corresponds to a safety factor.

CHAPTER 3: BIAXIAL LOADING OF 'LINER' MODEL

3.1 Introduction

In chapter 2, only uniaxial loading was considered. However, under complex conditions (surface morphology, settlement differences, complex shape of dump, etc.), one has to expect that the geomembrane will experience 2-dimensional loading (stretching).

This chapter aims to demonstrate that the developed modeling strategy for the geomembrane can also reproduce realistic results in the case of the biaxial loading of the geomembrane. In order to check the behavior of the geomembrane in terms of the stress-strain response, including crack development, two different models were set up to investigate the geomembrane behavior under different biaxial load constellations.

3.2 Model set-up

Two different approaches for biaxial pull tests were set up named Biaxial-Model-1 and Biaxial-Model-2 (see Fig. 3.1). The simulations were performed assuming a box of 1 x 1 x 0.5 m, composed of two half parts. The geomembrane is again represented by the 'liner' element. Only the geomembrane alone is considered in this study. The other parts of the model (interfaces as well as over- and underlying materials) were deactivated.

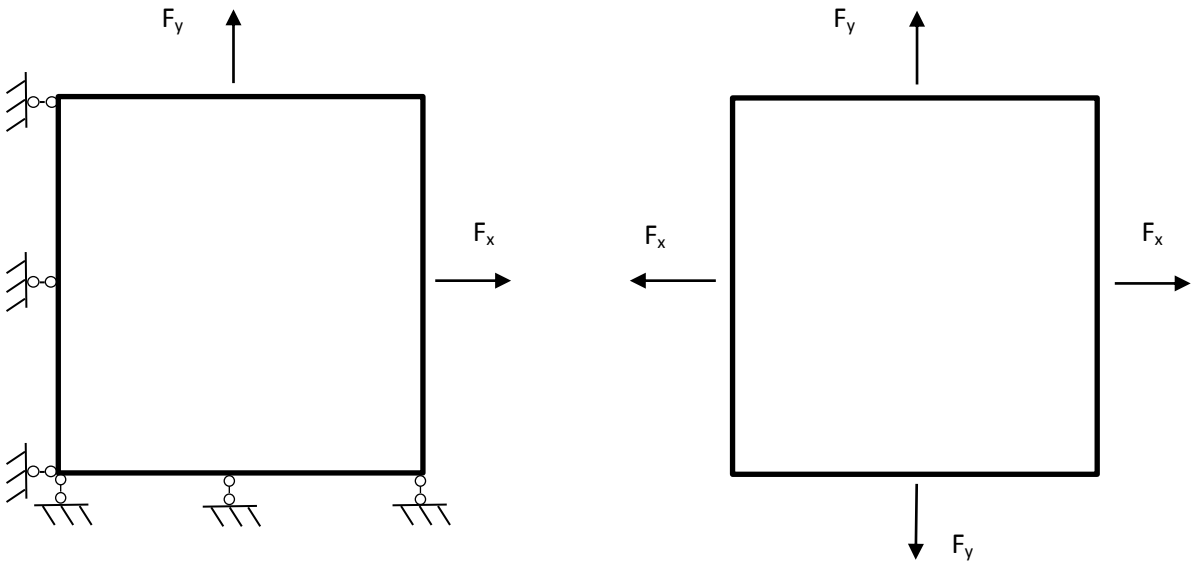

Figure 3.1: Models for biaxial testing of 'liner' element: Biaxial-Model-1 (left) and Biaxial-Model-2 (right)

The developed algorithm, which deletes elements whenever the maximum principal stress reaches the limit state, was applied to simulate the failure of the geomembrane. The 'liner' element consists of 3 nodes, as shown in Fig. 3.2. Thus, failure of the liner element always begins at one edge (node) of the element and develops further, for instance, from node 1 to node 3, as exemplarily shown in Fig. 3.2. The parameters of the 'liner' element representing the geomembrane used in the simulations are given in Tab. 3.1.

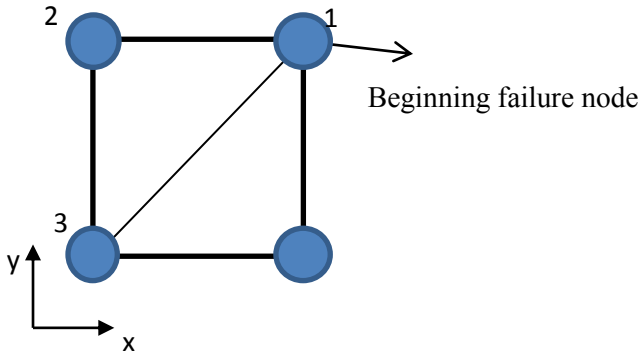

Figure 3.2: Structure of 'liner' element

Table 3.1: Properties of 'liner' element used for biaxial tests

Parameter	Value
E (Young's modulus), Pa	$6 \cdot 10^8$
ν (Poisson's ratio)	0.33
Thickness, m	0.003
Density, kg/m^3	900
Stress at the yield point (at about 16% strain), Pa	$1 \cdot 10^7$
Force at the yield point (at about 16% strain), N/m	$3 \cdot 10^4$

The simulations are performed using different loading conditions producing specific force ratios R:

$$R = \frac{F_y}{F_x} \tag{1}$$

F_x is the pull force in the x-direction,

F_y is the pull force in the y-direction

The force ratios R are set to 1; 1.25; 1.5; 1.75; 2 and 4 for both models. The pull force was produced by applying constant horizontal and vertical velocities at the outer boundaries of the

'liner', respectively. Velocity values were kept small so that quasi-static conditions were guaranteed. Whenever the tensile strength in one of the elements is reached, this element is deleted to simulate the ongoing crack propagation (same approach as used in chapter 2).

3.3 Results of biaxial pull-out test simulation

a) Biaxial-Model-1

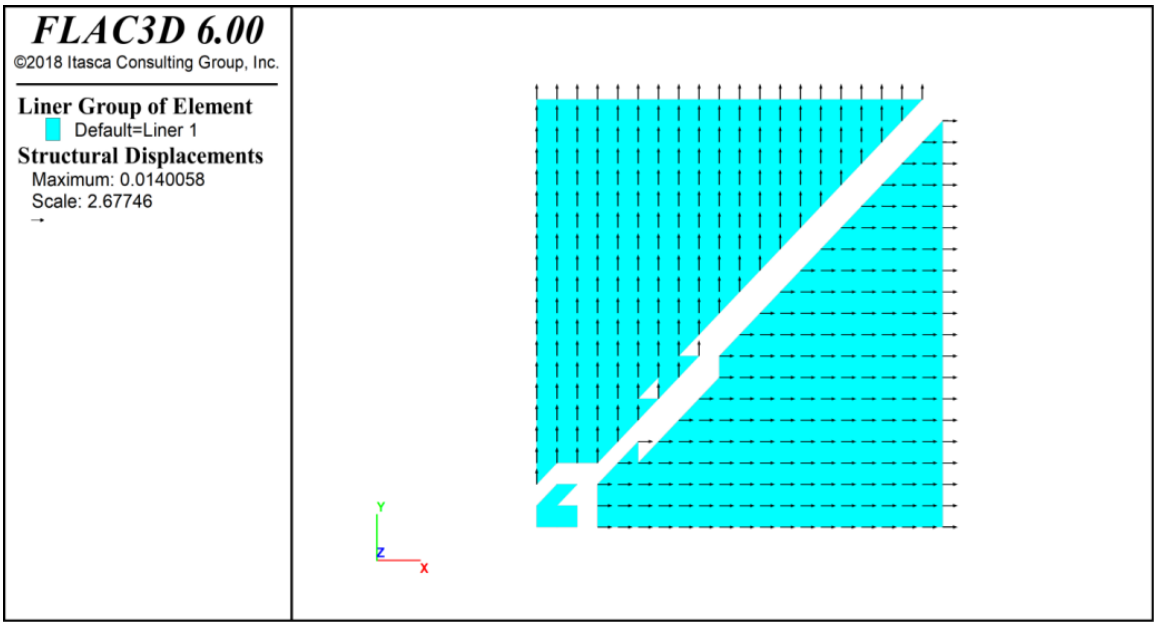

Figure 3.3: Failure of geomembrane at final stage for *R*=1 (Biaxial-Model-1)

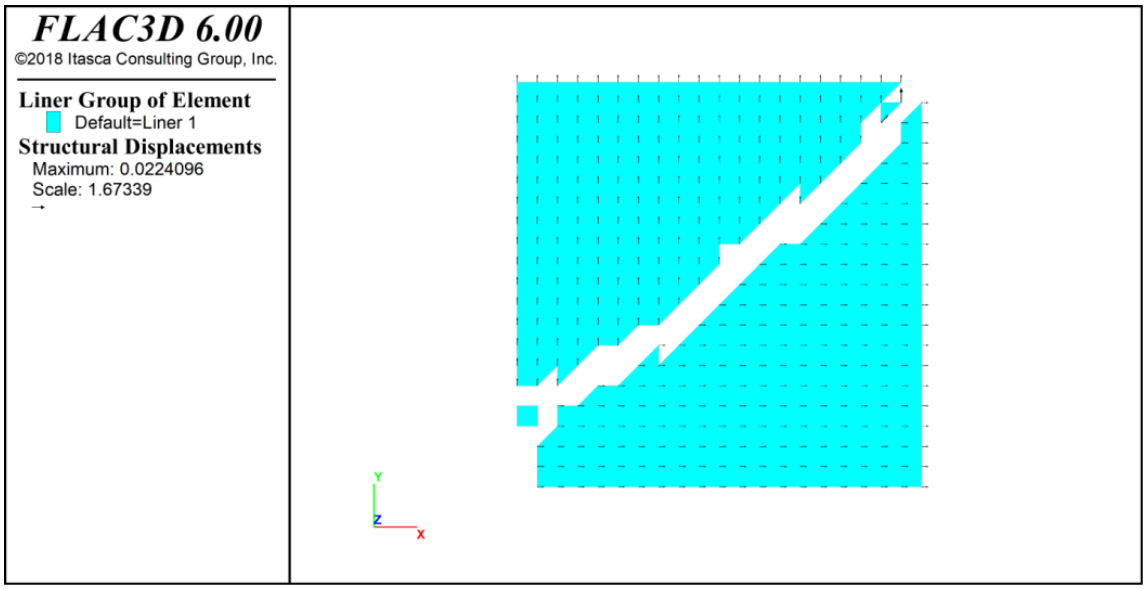

Figure 3.4: Failure of geomembrane at final stage for *R*=1.25 (Biaxial-Model-1)

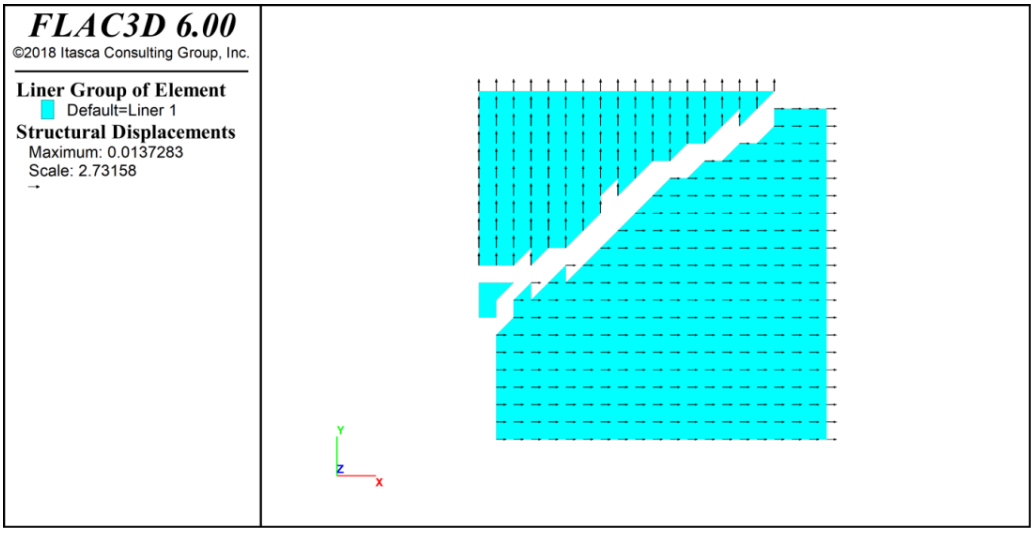

Figure 3.5: Failure of geomembrane at final stage for *R*=1.50 (Biaxial-Model-1)

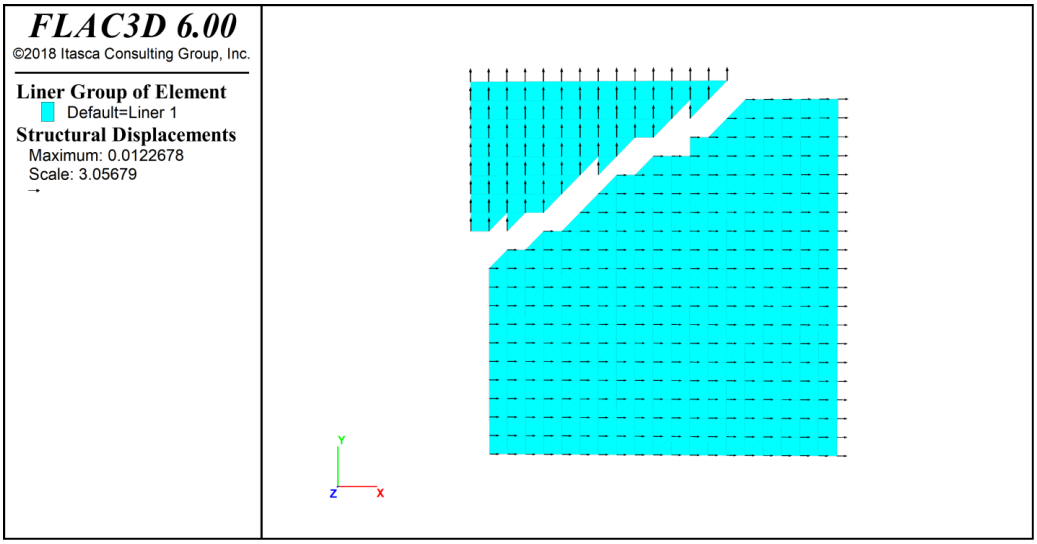

Figure 3.6: Failure of geomembrane at final stage for *R*=1.75 (Biaxial-Model-1)

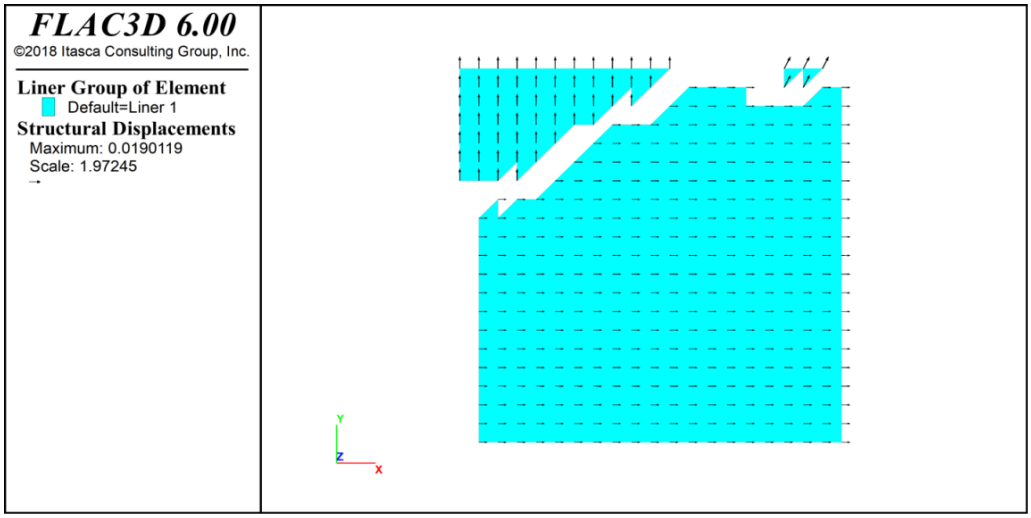

Figure 3.7: Failure of geomembrane at final stage for *R*=2 (Biaxial-Model-1)

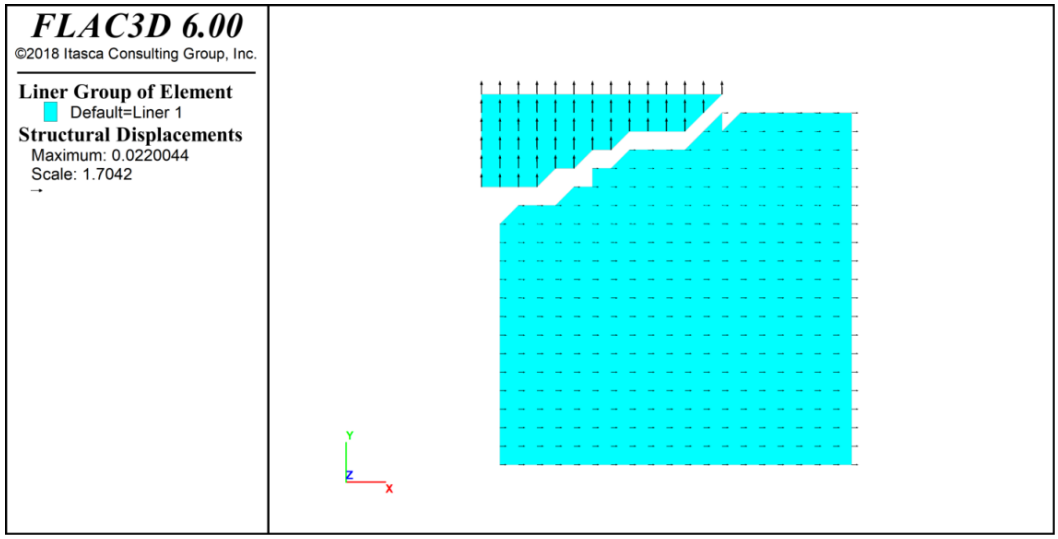

Figure 3.8: Failure of geomembrane at final stage for *R*=4 (Biaxial-Model-1)

As expected, the orientation of crack development follows the ratio of applied forces R. Fig. 3.9.

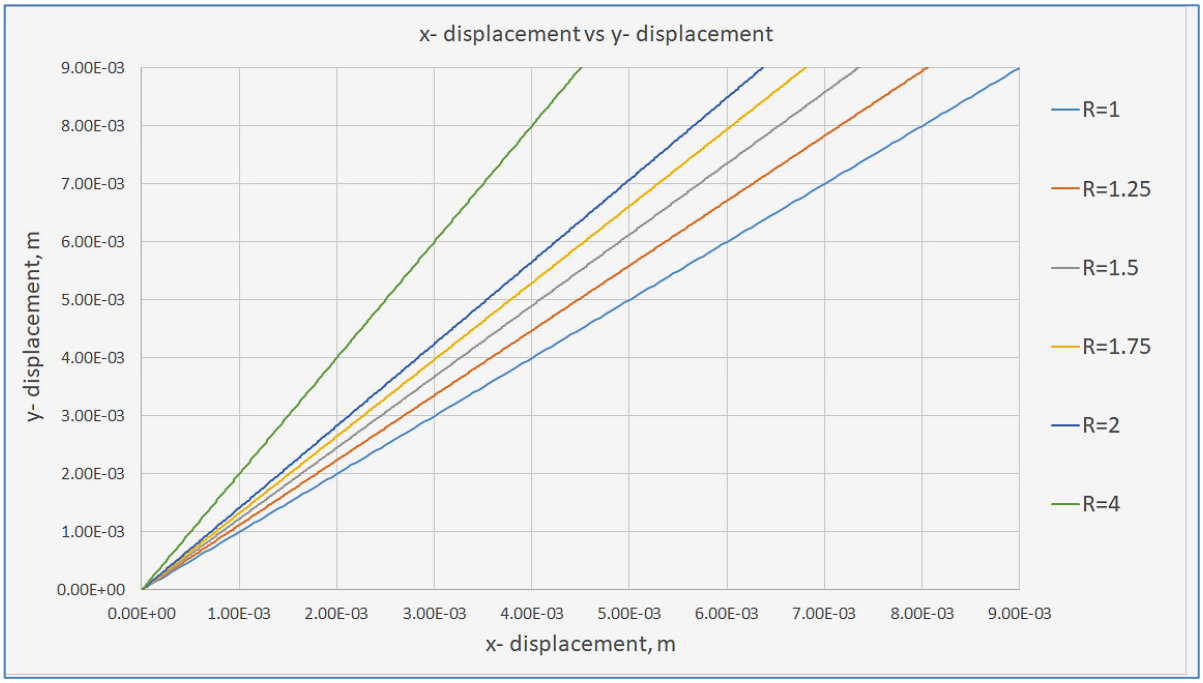

Figure 3.9: x-displacement versus y-displacement for different force ratio *R* (Model-1)

Fig. 3.10, and 3.11 illustrate the development of the displacement for the individual model runs.

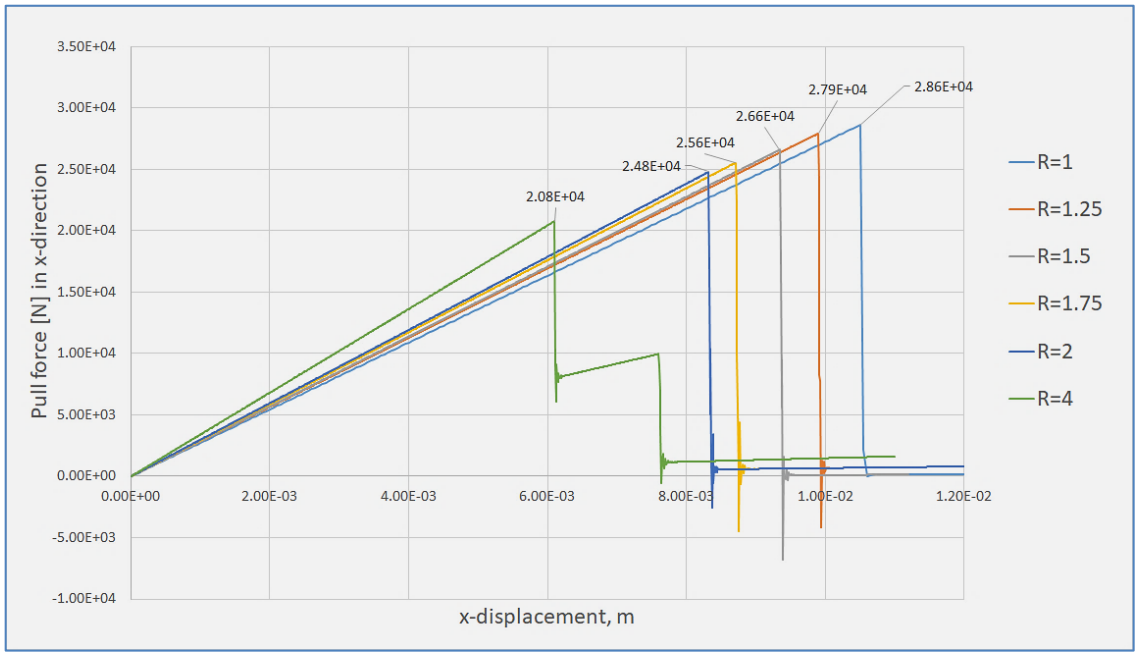

Figure 3.10: Pull force (N/m) in x-direction versus x-displacement for different force ratio *R* (Biaxial-Model-1)

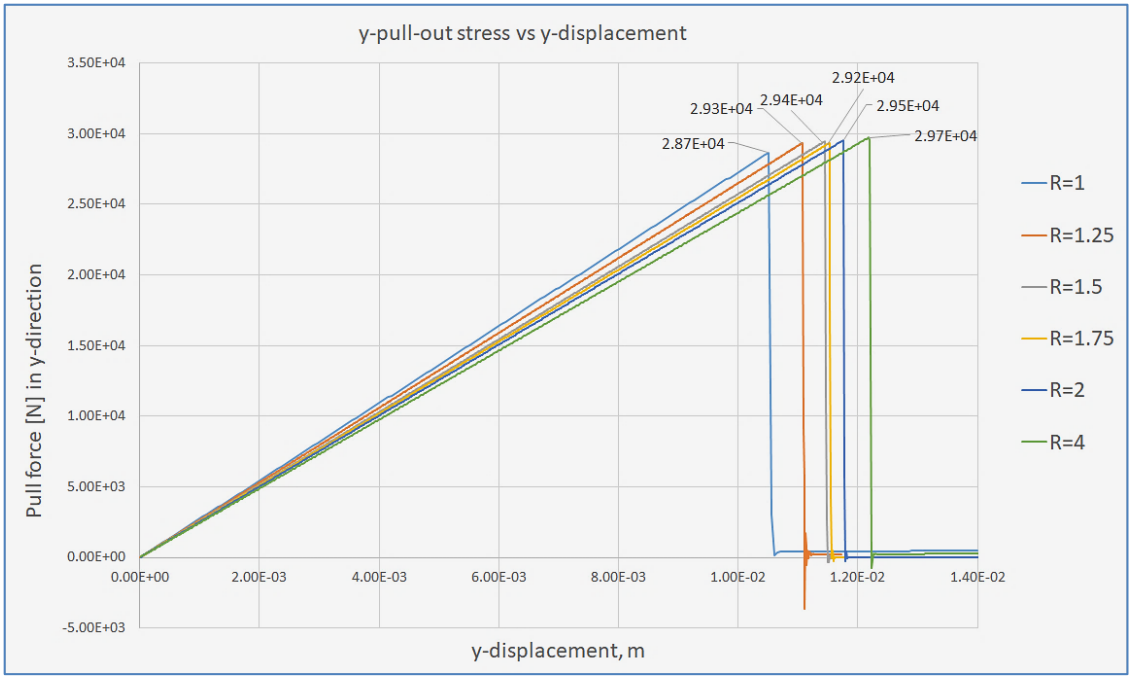

Figure 3.11: Pull force (N/m) in y-direction versus y-displacement for different force ratio *R* (Biaxial-Model-1)

The y-displacement is always greater (or equal in the case of $R = 1$) than the x-displacement following the ratio of R. The pull force in the x-direction reduces from $2.86 \cdot 10^4$ N/m for $R = 1$ to $2.08 \cdot 10^4$ N/m for $R = 4$, whereas the pull force in the y-direction is nearly constant at about $2.9 \cdot 10^4$ Pa independent of the ratio of R. The corresponding failure stress has to consider the real

thickness of the geotextile (here: 0.003 m). This means $2.9 \cdot 10^4$ Pa/m / 0.003 m = $0.966 \cdot 10^7$ Pa which corresponds to the failure strength of 10^7 Pa given in Tab. 3.1. Note also that the horizontal extension of the modeled geotextile is 1 x 1 m so that registered force in N corresponds to a line load of N/m.

b) Biaxial-Model-2

The simulation results of Biaxial-Model-2 are nearly identical to those of Biaxial-Model-1. This holds for both, the deformations and the failure stress or force. The pull force in the x-direction decreases from $2.9 \cdot 10^4$ N/m to $2.12 \cdot 10^4$ N/m with an increasing ratio of *R*. The pull force in the y-direction is - independent of *R* - constant with nearly $3 \cdot 10^4$ N/m. The corresponding failure stress has to consider again the real thickness of the geotextile (here: 0.003 m). This means $3 \cdot 10^4$ Pa/m / 0.003 m = 10^7 Pa, which corresponds to the failure strength of 10^7 Pa as given in Tab. 3.1.

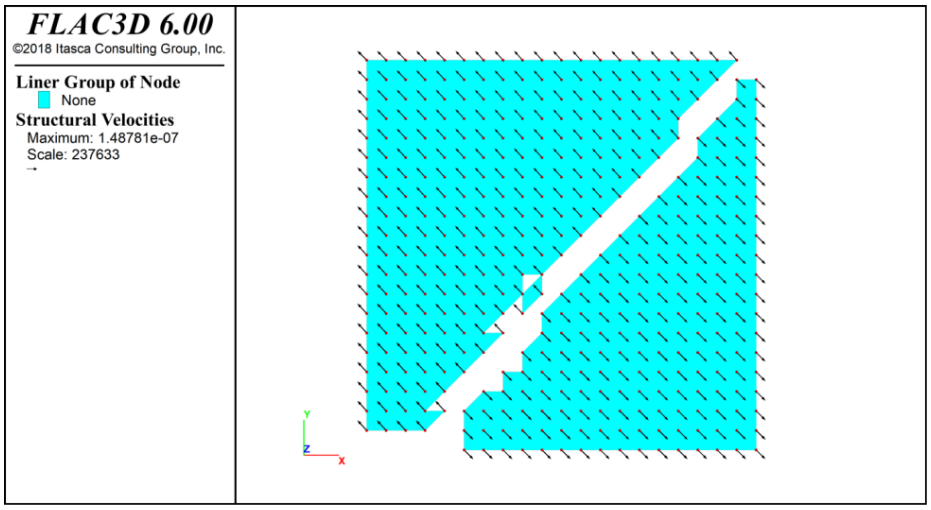

Figure 3.12: Failure of geomembrane at final stage for *R*=1.0 (Biaxial-Model-2)

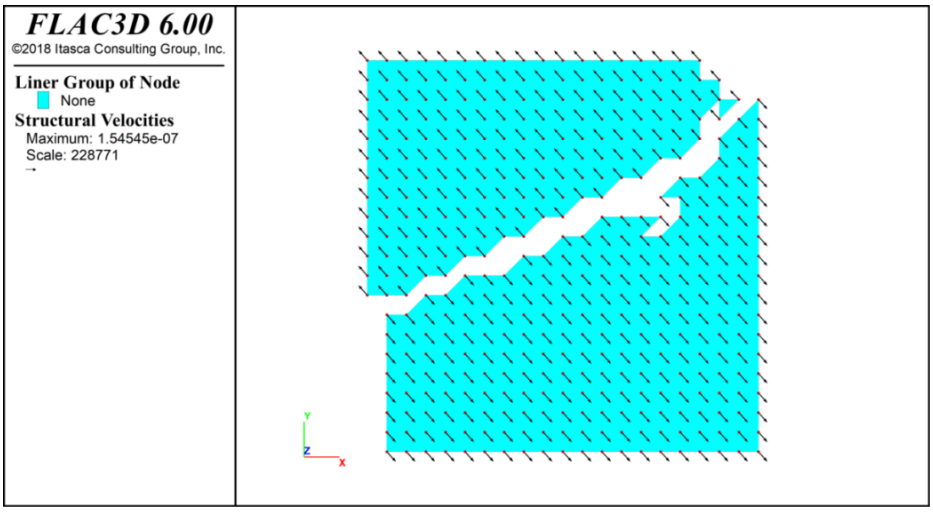

Figure 3.13: Failure of geomembrane at final stage for *R*=1.25 (Biaxial-Model-2)

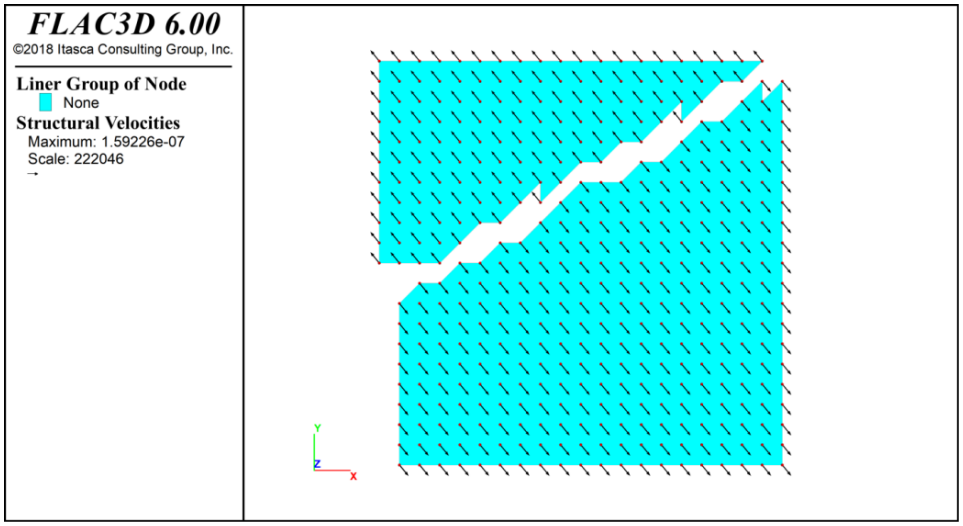

Figure 3.14: Failure of geomembrane at final stage for *R*=1.5 (Biaxial-Model-2)

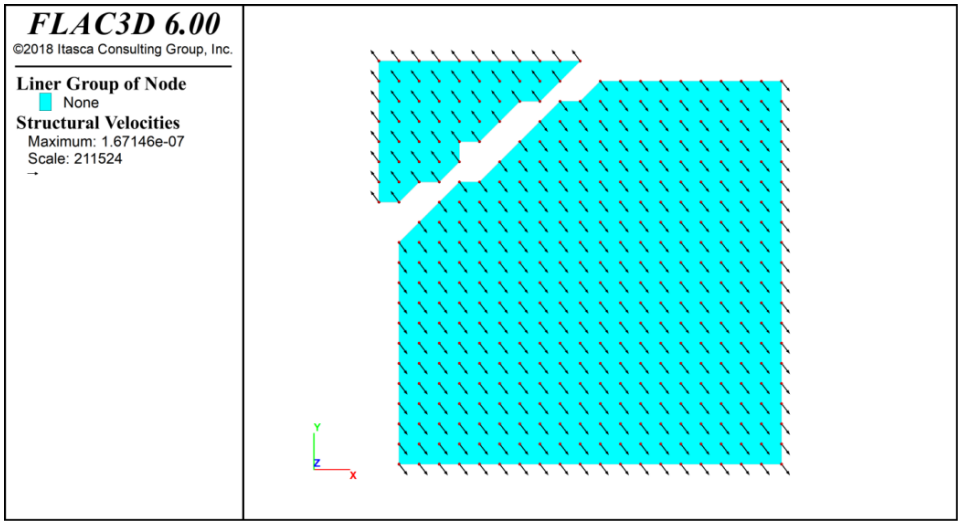

Figure 3.15: Failure of geomembrane at final stage for *R*=1.75 (Biaxial-Model-2)

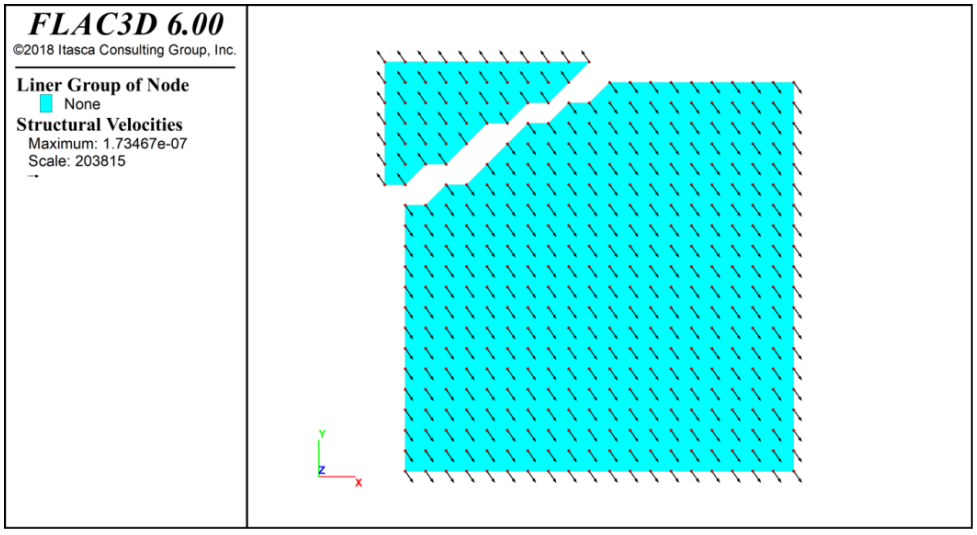

Figure 3.16: Failure of geomembrane at final stage for *R*=2.0 (Biaxial-Model-2)

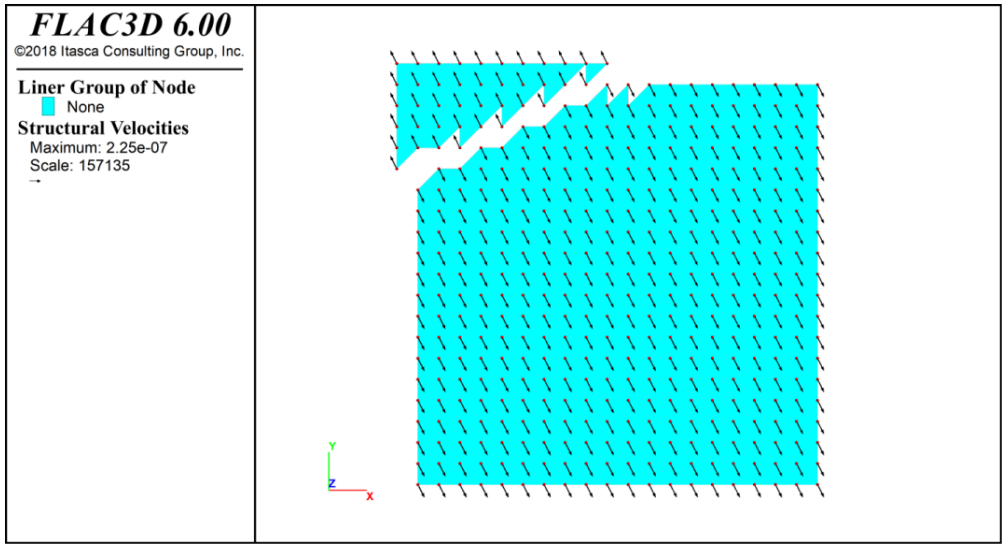

Figure 3.17: Failure of geomembrane at final stage for *R*=4.0 (Biaxial-Model-2)

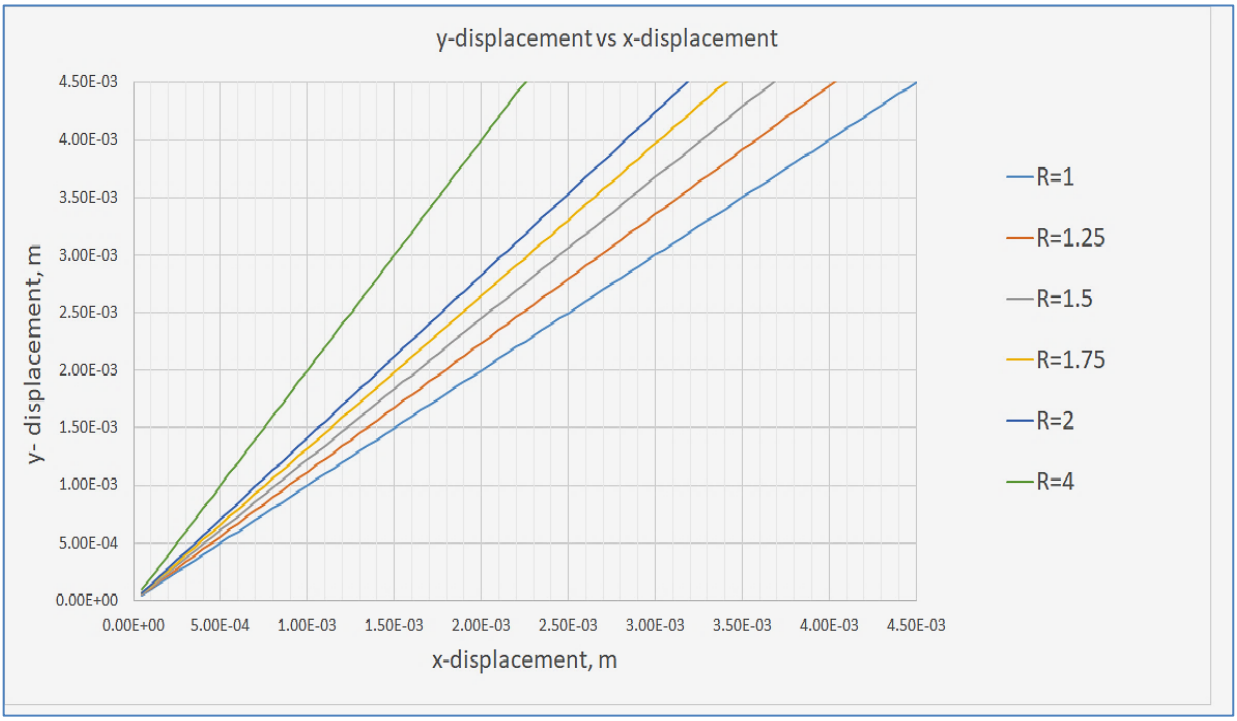

Figure 3.18: x-displacement versus y-displacement for different force ratio *R* (Model-2)

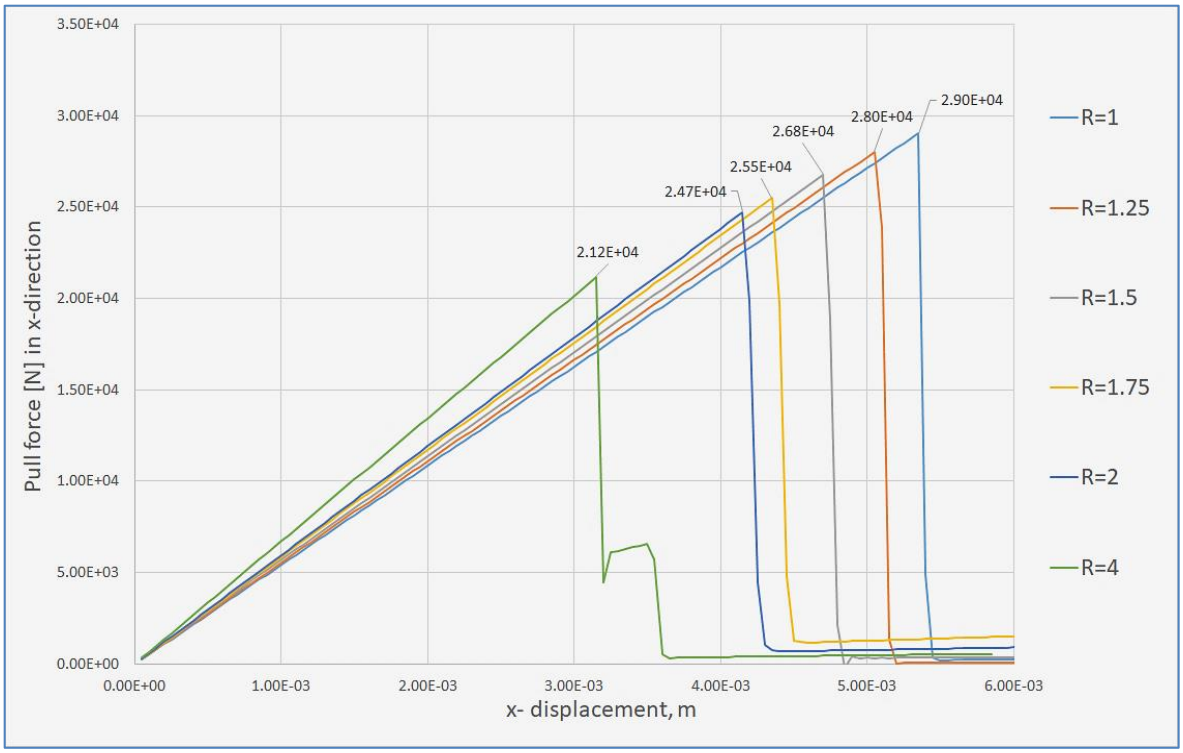

Figure 3.19: Pull force (N/m) in x-direction versus x-displacement for different force ratio R (Biaxial-Model-2)

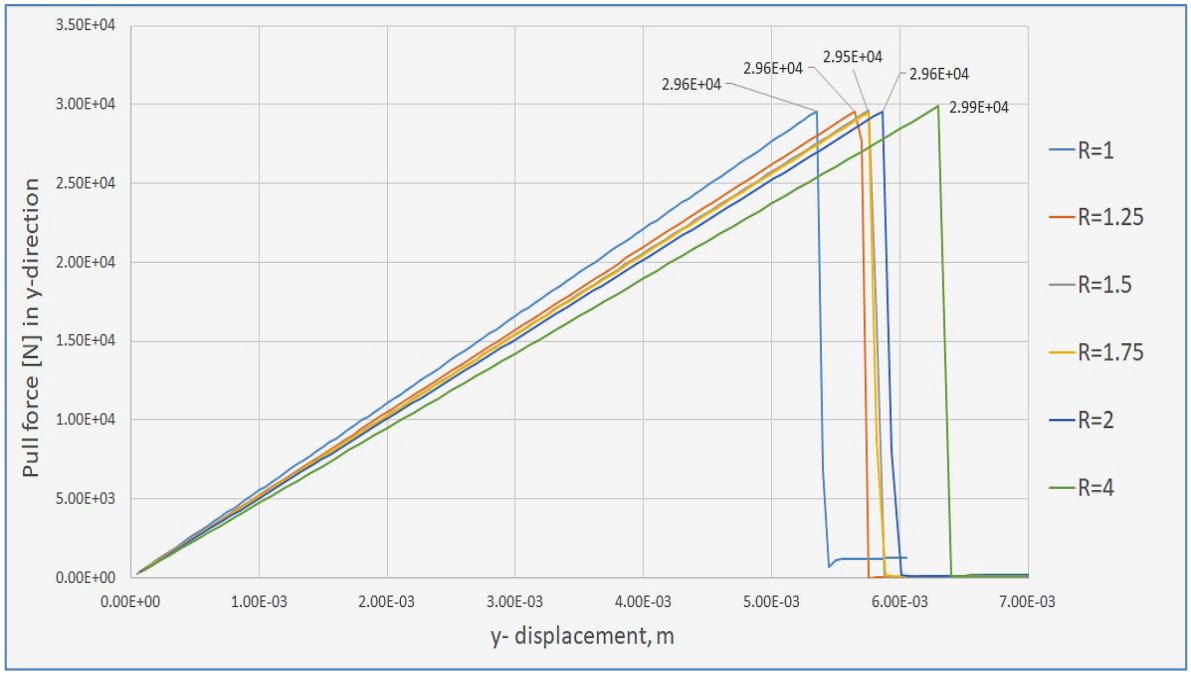

Figure 3.20: Pull force (N/m) in y-direction versus y-displacement for different force ratio R (Biaxial-Model-2)

3.4 Summary and Conclusions

Fig. 3.21 summarizes the obtained simulation results for both models. In all simulation cases, the observed failure load is between $2.9 \cdot 10^4$ and $3 \cdot 10^4$ N/m, corresponding to a failure stress of 10^7 Pa. This value, in turn, fits the strength of the material. The direction of crack development follows the ratio between the applied biaxial forces. The crack pattern is characterized by a single discrete crack, as expected. Both modeling procedures give nearly identical results.

It can be concluded that the liner element, in combination with the developed routine, which monitors the stresses in the individual liner elements and deletes them whenever they reach the limit value, can be applied in complex 3D models to simulate the behavior of the geomembrane under arbitrary biaxial loading.

Exemplary, Fig. 3.23 shows the crack development in stages until the geomembrane is separated into two parts. Crack development starts at the right upper corner and develops diagonally through the geomembrane. Please note that crack propagation patterns are stable and reproducible. Still, any very small disturbance (small scatter in material parameters) or even numerical noise can lead to local differences in crack propagation (compare, for instance, Fig. 3.22 and Fig. 3.23 latest stage).

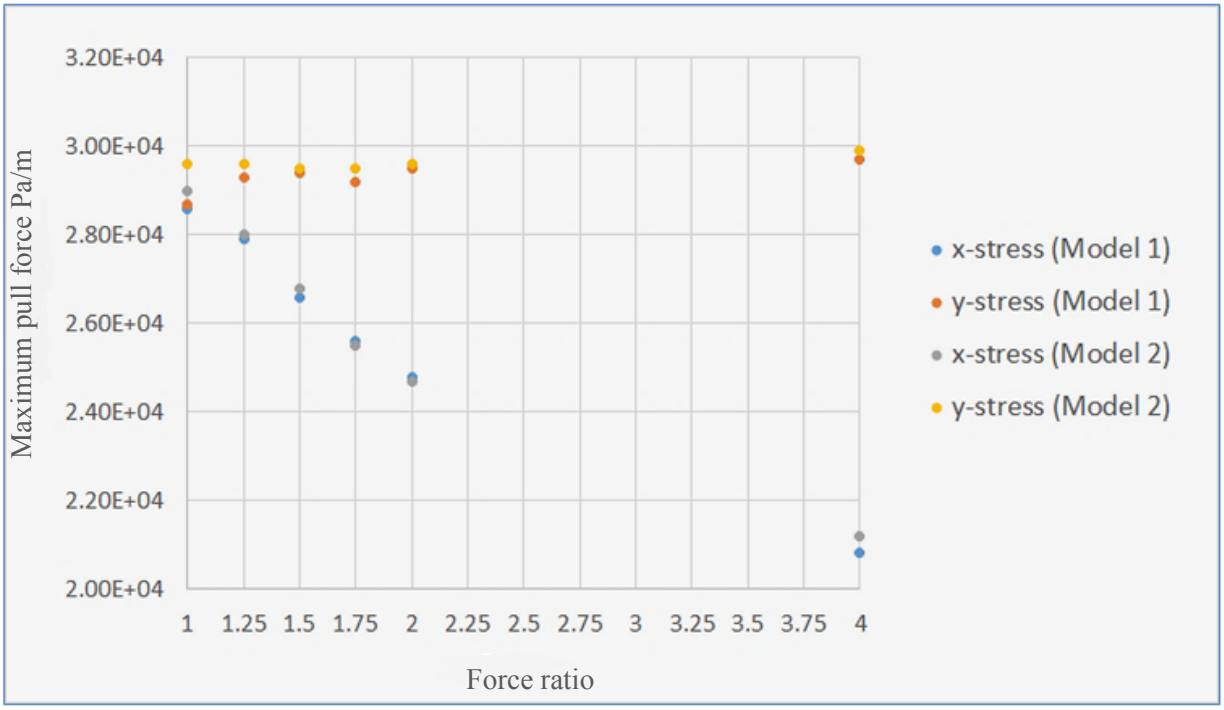

Figure 3.21: Pull forces (N/m) in y- and x-direction versus force ratio *R* (Biaxial-Model-1 and Biaxial-Model-2)

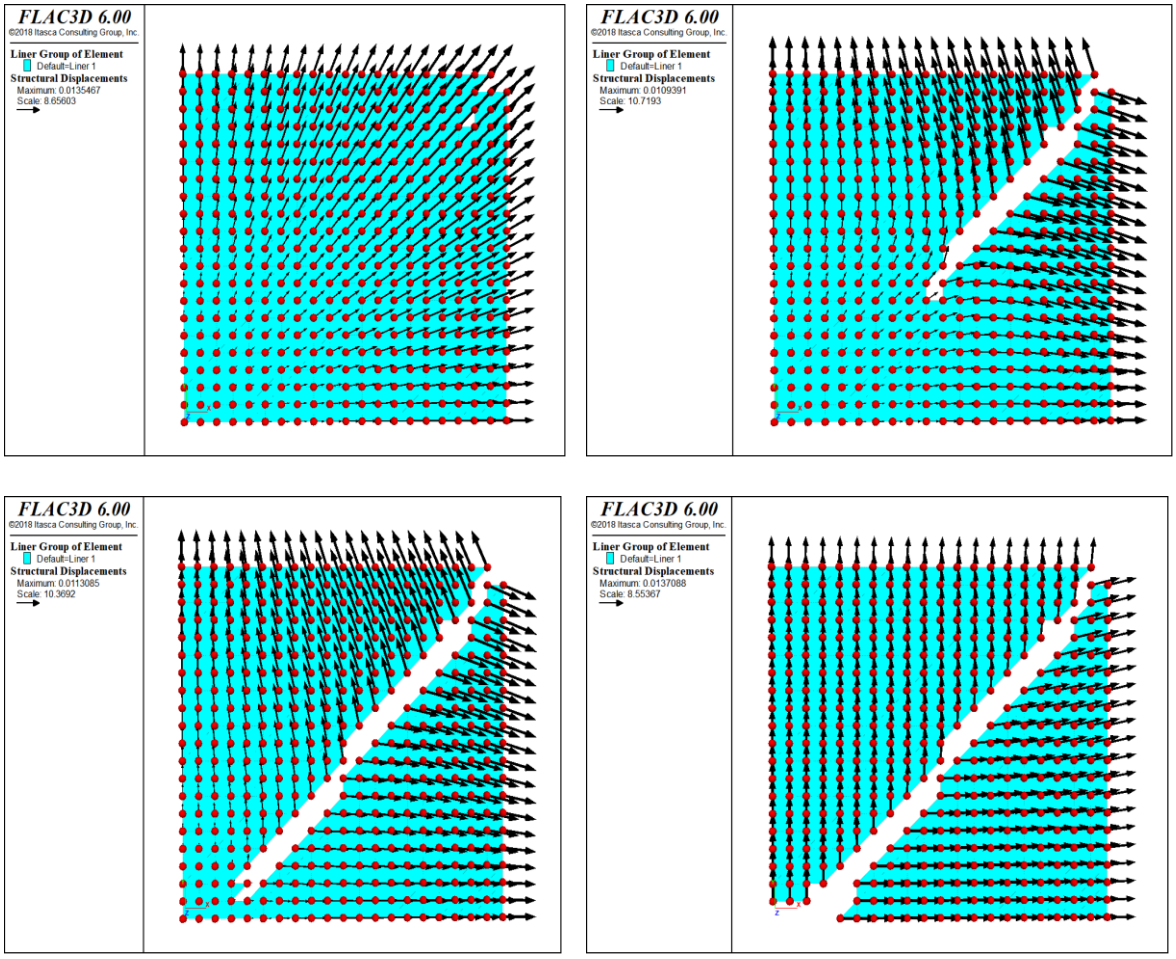

Figure 3.22: Selected stages of crack propagation (Biaxial-Model-1, *R*=1)

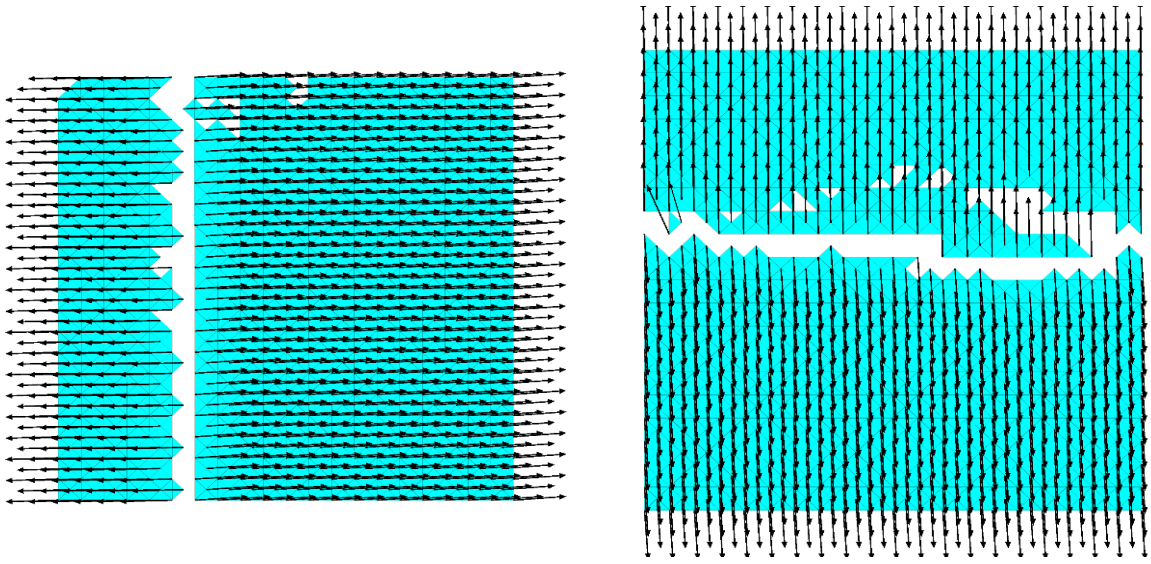

Figure 3.23: Biaxial-Model-2 at final stage (left: uniaxial pull in x-direction, right: uniaxial pull in y-direction)

If only a uniaxial tensile load is applied, the fracture develops more or less perpendicular to the applied load as expected. Due to the fact that the model is isotropic and homogeneous, theoretically, any element has the same chance to break. Please note that the fractures can slightly deviate or branch due to numerical noise and some very minor rotation due to imbalances. This numerical effect can also be interpreted as very small local inhomogeneity in the strength of the material (small variation in thickness and/or material properties).

CHAPTER 4: PARAMETER STUDY OF EMBEDDED GEOMEMBRANE

4.1 Introduction

To verify the developed 'liner' modeling strategy further, a bigger model (see Fig. 4.1) is set up which contains an underlying stiff material and an overlying soft material. The geomembrane is simulated by the 'liner' element as described in detail in chapters 2 and 3. FLAC^{3D} is used for the simulations. Special attention is paid to the stress-strain behavior of the geomembrane as well as potential damage.

The simulations include large deformations and show how the chosen interface parameters influence the movement of the soft overlying material. The softening or creeping behavior of the overlying material (a 130 m high block) is duplicated in a simplified manner by assigning a high Poisson's ratio to the elastic overlying material. This produces large horizontal displacements in dependence on the interface properties.

Apart from the two interfaces on both sides of the geomembrane, all other model elements behave as pure elastic. This chapter aims to document (1.) the robustness of the two-sided interface logic covering a huge parameter range and (2.) to illustrate the impact of the frictional characteristics on both sides of the geomembrane on the overlying material and the geomembrane behavior.

4.2 Model set-up

The model consists of two blocks: over- and underlying material (they may represent a waste dump and the ground in a simplified manner) and the 'liner' element representing the geomembrane. The model works in the large strain mode. The dimensions of this model are shown in Fig. 4.1 and 4.2 (zone edge length is 20 m):

- Overlying material: 520 x 520 x 130 m
- Underlying material: 1000 x 1000 x 20 m
- Geomembrane: 800 x 800 m

The properties as given in Tab. 4.1 are assigned to the over- and underlying material. High stiffness values are assigned to the underlying material and very low to the overlying material to provoke large potential horizontal displacements like expected for instance during long-term creep. Tab. 4.2 shows the assumed properties of the geomembrane. The parameters of the two

interfaces are given in Tab. 4.3. The interfaces are defined as follows: Side 1 (interface below: interface between underlying material and geomembrane) and Side 2 (interface above: interface between overlying material and geomembrane).

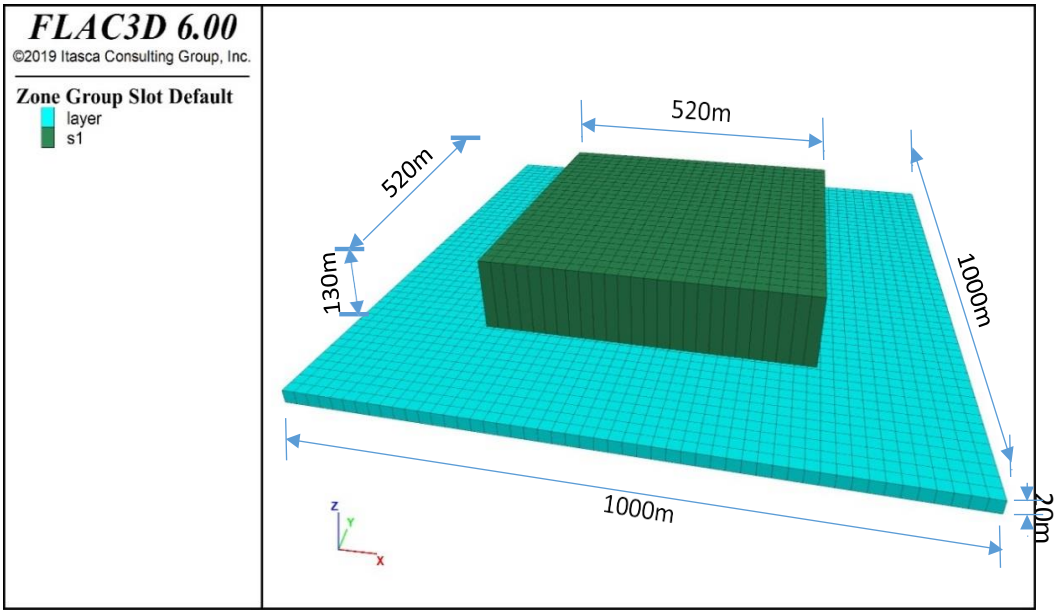

Figure 4.1: Model overview

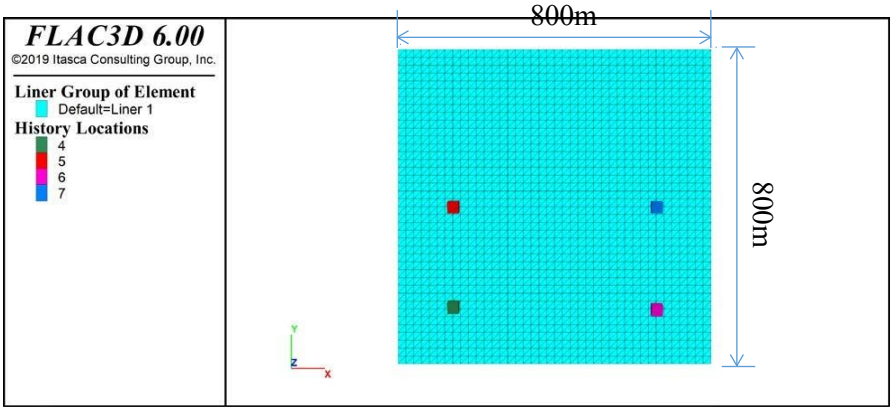

Figure 4.2: 'liner' element (geomembrane) with history locations

Table 4.1: Model properties for over- and underlying materials

Parameter	Overlying material	Underlying material
	Elastic	Elastic
E (Young's modulus), Pa	10^7	10^{10}
ν (Poisson's ratio)	0.49	0.3
ρ (Density), g/cm^3	2000	2000

Histories with ID 4, 5, 6, and 7 (see Fig. 4.2) are installed at the outer boundary of the overlying material. They are used to observe the displacements. ID 4 and 6 are located at the corner of the

overlying material, while ID 5 and 7 are located along the centerline. ID 4 and 5 belong to the bottom of the overlying material, ID 6 and 7 belong to the geomembrane.

Table 4.2: Geomembrane parameters

Parameter	Value
Thickness, mm	3
E (Young's modulus), Pa	$26 \cdot 10^9$
ν (Poisson's ratio)	0.33
ρ (Density), g/cm^3	1

The coupling-shear stiffness k_s and the coupling-normal stiffness k_n at the interfaces are set equal. The shear stiffness is set equal 10 to 100 times the equivalent zone stiffness of the neighboring elements:

$$k_s = k_n = \frac{K + \frac{4}{3}G}{\Delta z} \quad (10 \ldots 100) \tag{2}$$

where: - K and G are the bulk and shear modulus of neighboring elements; respectively,

- Δz is the smallest dimension of the adjacent zone in the normal direction.

Therefore, the value of $k_s = k_n$ varied from 10^8 Pa/m to 10^{12} Pa/m.

Table 4.3: Properties of geomembrane interfaces

Parameter	Side	Value
Coupling-yield-normal: normal coupling spring tensile strength, Pa	1	10^{10}
Coupling-yield-normal-2: normal coupling spring tensile strength, Pa	2	10^{10}
Coupling-stiffness-normal (k_{n1}): normal coupling spring stiffness, Pa/m	1	varies
Coupling-stiffness-normal-2 (k_{n2}): normal coupling spring stiffness, Pa/m	2	varies
Coupling-stiffness-shear (k_{s1}) of the below side: shear coupling spring stiffness, Pa/m	1	varies
Coupling-stiffness-shear-2 (k_{s2}): shear coupling spring stiffness per unit, Pa/m	2	varies
Coupling-cohesion-shear: shear coupling spring cohesion (stress unit), Pa	1	varies
Coupling-cohesion-shear-2: shear coupling spring cohesion (stress unit), Pa	2	varies
Coupling-cohesion-shear-residual: shear coupling spring residual cohesion, Pa	1	0
Coupling-cohesion-shear-residual-2: shear coupling spring residual cohesion, Pa	2	0
Coupling-friction-shear: shear coupling spring friction angle (φ_1), ^{o}	1	varies
Coupling-friction-shear-2: shear coupling spring friction angle on side 2 (φ_2), ^{o}	2	varies
Sliding tolerance	-	10^{-3}

4.3 Results

The general stress and deformation behavior of the geomembrane is illustrated exemplarily in Fig. 4.3 and 4.4. The displacements of the geomembrane reach the maximum value at the outer boundary of the overlying material (Fig. 4.3).

The displacement of the geomembrane increases from the center towards the outer boundary. The maximum principal stress of the geomembrane is located at the center of the geomembrane and descends towards the boundary when the friction angle below is greater than above. The maximum principal stress in the geomembrane concentrates at the boundary areas of the overlying material when the friction angle above is greater or equal to the one below. Exemplary, Fig. 4.5 shows the horizontal stress component (xx-stress) in the underlying material at the lower boundary of the overlying material.

a)

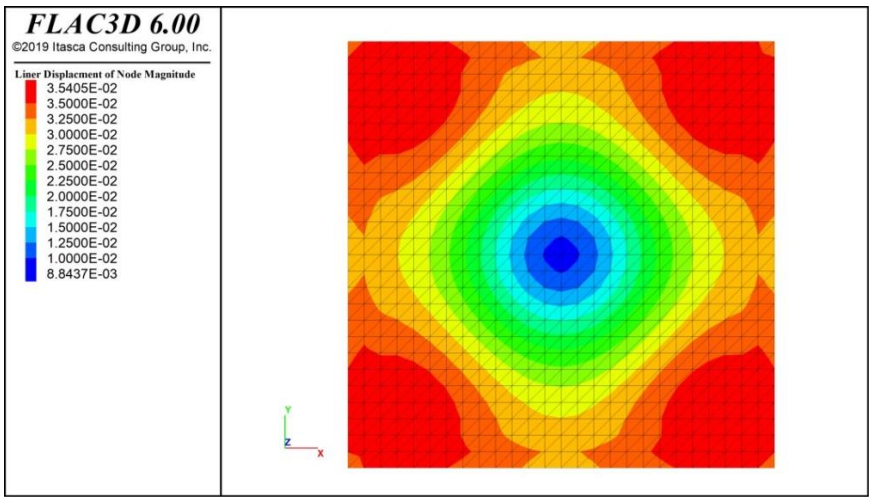

b)

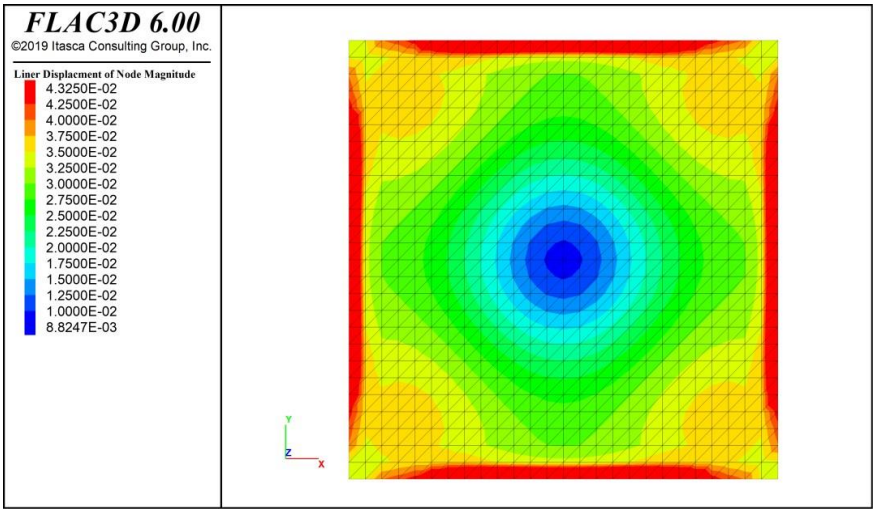

c)

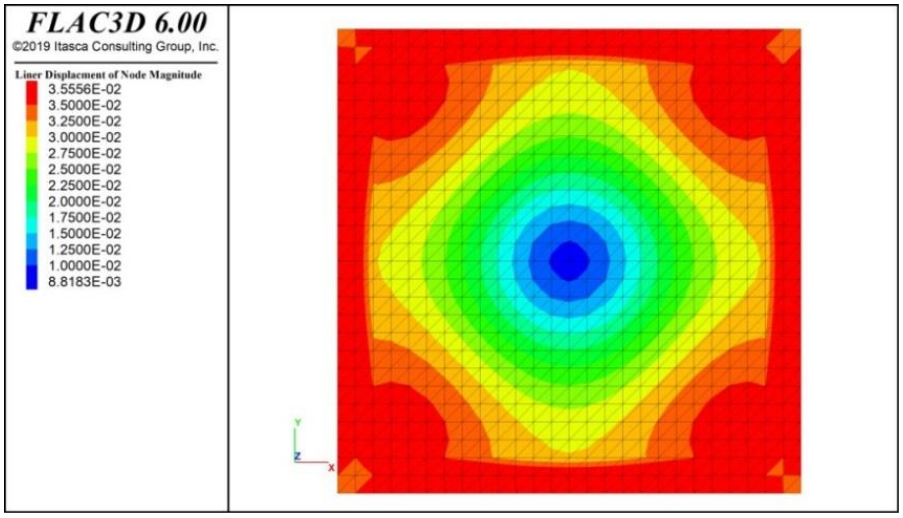

Figure 4.3: Total displacement (m) of geomembrane

a) *Geomembrane displacement magnitude in case the friction angle below is greater than above*
b) *Geomembrane displacement magnitude in case the friction angle below and above are equal*
c) *Geomembrane displacement magnitude in case the friction angle above is greater than below*

a)

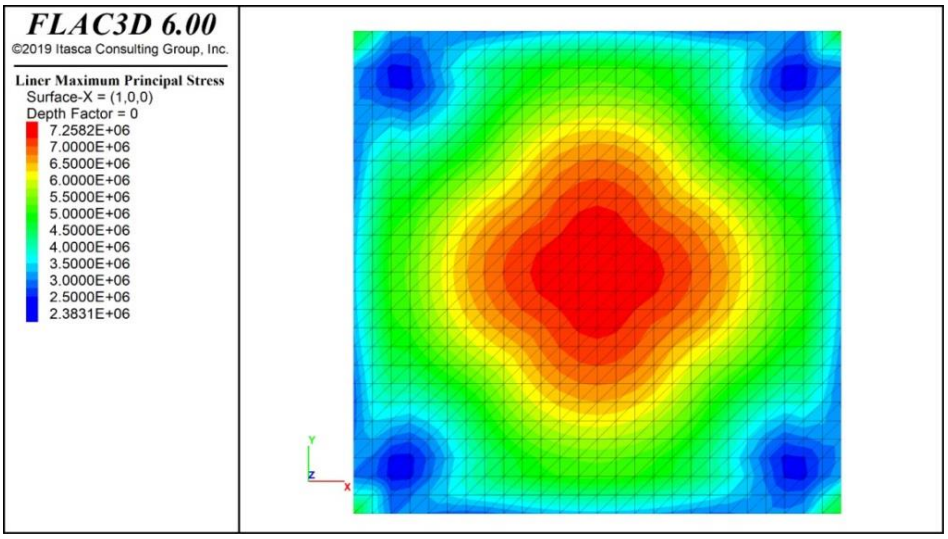

b)

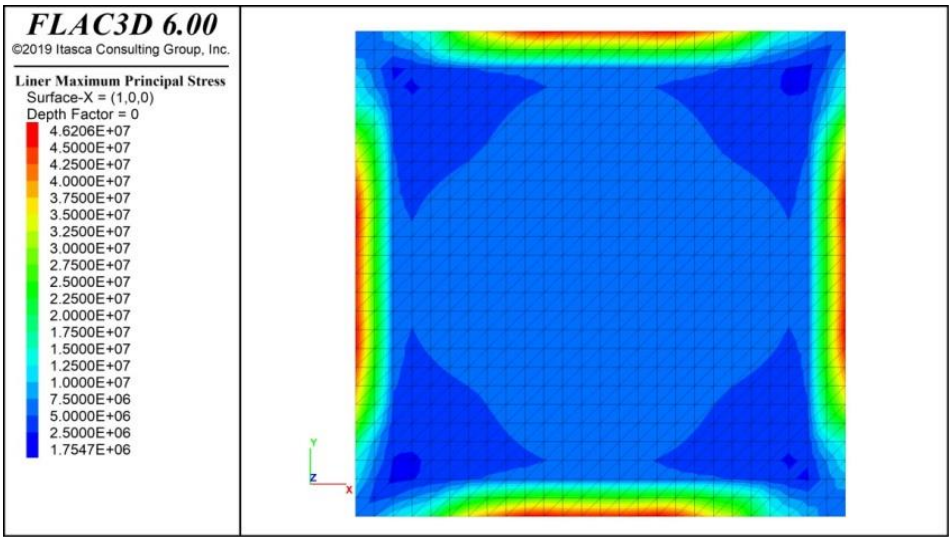

c)

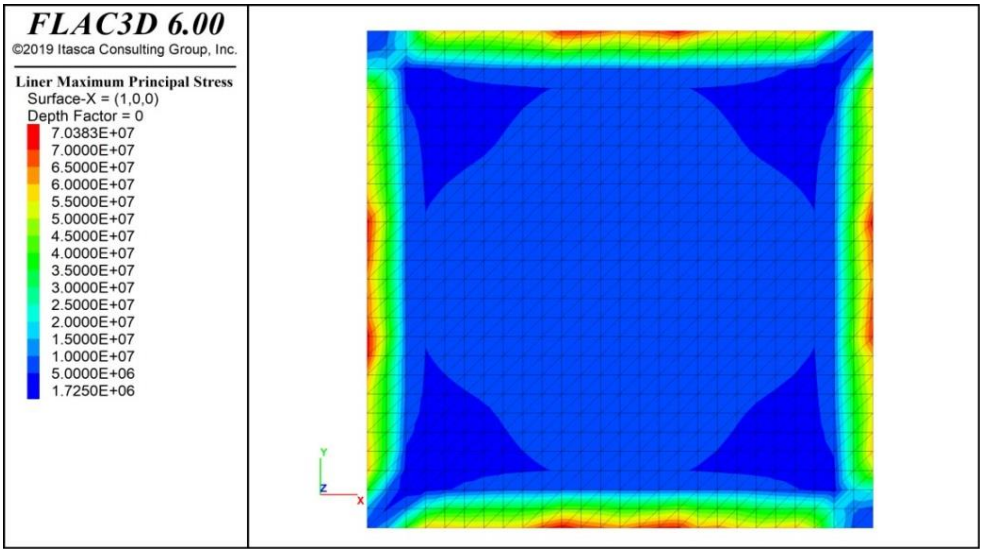

Figure 4.4: Maximum principal stress (Pa) of geomembrane

a) Geomembrane maximum principal stress in case the friction angle below is greater than above
b) Geomembrane maximum principal stress in case the friction angle below is equal to above
c) Geomembrane maximum principal stress in case the friction angle above is greater thanbelow

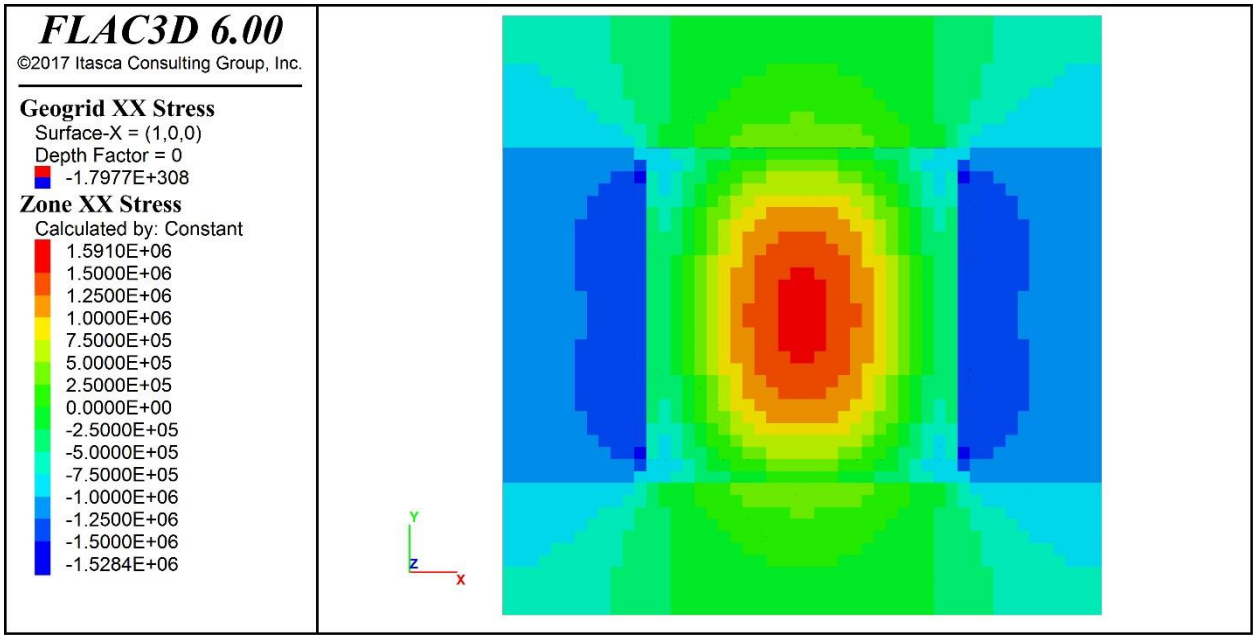

Figure 4.5: xx-stress (Pa) in the underlying material

4.3.1 Influence of interface stiffness

In a reference case (REF), the shear and normal stiffness of both interfaces are set to 10^9 Pa/m. In different simulation cases, interface stiffness $k_s = k_n$ was set to 10^8, 10^{10}, and 10^{12} Pa/m. Tab. 4.4 shows an overview of the individual simulations performed to verify the functionality and investigate the effect of interface stiffness.

Table 4.4: Overview of calculation cases

Case	Interface friction angle, °		Interface stiffness, Pa/m	
	Side 1 (below)	Side 2 (above)	Side 1 (below)	Side 2 (above)
1	0		Both sides are equal: 10^8, 10^{10}, 10^{12}	
2	90 (*)		Both sides are equal: 10^8, 10^{10}, 10^{12}	
3	90 (*)	0	Both sides are equal: 10^8, 10^{10}, 10^{12}	
4	0	90 (*)	Both sides are equal: 10^8, 10^{10}, 10^{12}	
5-1	20	Varying (10, 20, 30, 40, 50, 60)	Both sides are equal: 10^9	
5-2	Varying (10, 20, 30, 40, 50, 60)	20	Both sides are equal: 10^9	
6-1	30	Varying (10, 20, 30, 40, 50, 60)	Both sides are equal: 10^9	
6-2	Varying (10, 20, 30, 40, 50, 60)	30	Both sides are equal: 10^9	
7-1	40	Varying (10, 20, 30, 40, 50, 60)	Both sides are equal: 10^9	
7-2	Varying (10, 20, 30, 40, 50, 60)	40	Both sides are equal: 10^9	

(*) The interfaces and materials are glued together

Case 1 (extremely weak connection between geomembrane and surrounding material)

In this case, the friction angles of both sides are set to 0^o. The model parameters are shown in Tab. 4.5

Table 4.5: Interface parameters (case 1)

Parameter	k_n, Pa/m	k_s, Pa/m	φ,°
Side 1 (below)	10^8	10^8	0
Side 2 (above)	10^8	10^8	0
Side 1 (below)	10^{10}	10^{10}	0
Side 2 (above)	10^{10}	10^{10}	0
Side 1 (below)	10^{12}	10^{12}	0
Side 2 (above)	10^{12}	10^{12}	0

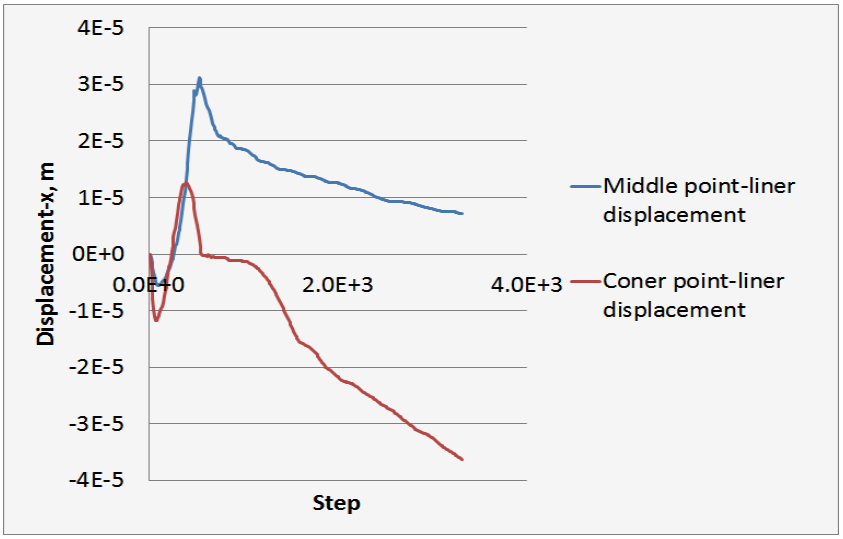

Figure 4.6: Displacements of liner nodes ID 6 and 7 vs. calculation steps (case 1-1: k_s=k_n=10^8 Pa/m)

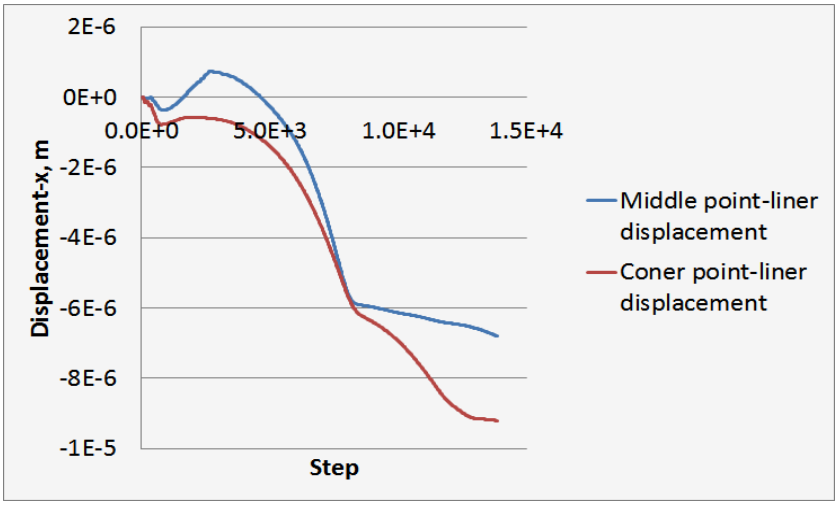

Figure 4.7: Displacements of liner nodes ID 6 and 7 vs. calculation steps (case 1-2: k_s=k_n=10^{10} Pa/m)

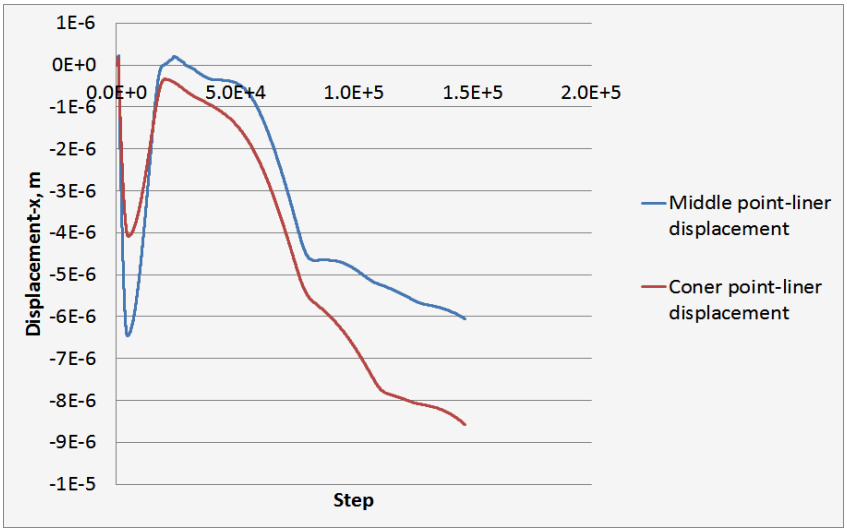

Figure 4.8: Displacements of liner nodes ID 6 and 7 vs. calculation steps (case 1-3: k=k_n=10^{12} Pa/m)

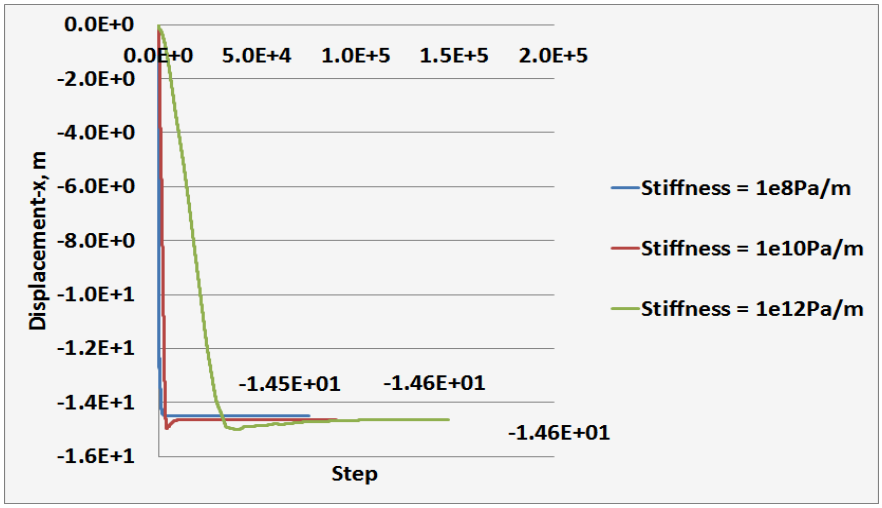

Figure 4.9: Displacements of gridpoint ID 5 vs. calculation steps (case 1)

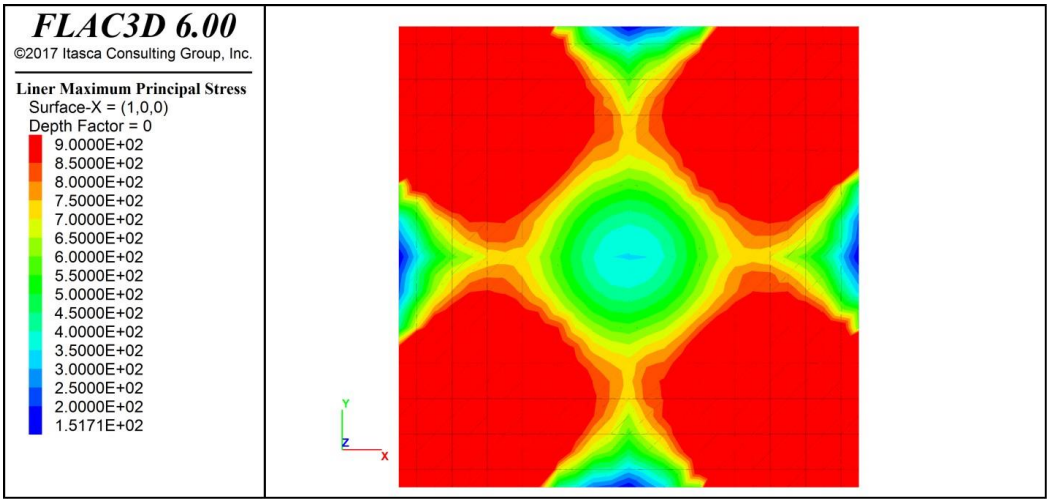

Figure 4.10: Maximum principal stress (Pa) in geomembrane (k_n=k_s=10^{12} Pa/m)

Table 4.6: Displacements of gridpoint ID 5 and geomembrane maximum principal stress values (case 1)

k_n=k_s, Pa/m	Gridpoint (ID 5) displacement, m	Geomembrane maximum principal stress, Pa
10^8	14.5	5000
10^{10}	14.6	1100
10^{12}	14.6	900

In this case, the overlying material can freely expand, and the geomembrane is not loaded. Results are independent of interface stiffness. Zero friction triggers numerical instabilities. It takes a very long time to reach a nearly stable situation, but as expected: displacements (strain) and stresses inside the geomembrane converge towards zero. Tab. 4.6 and Fig. 4.10 show an interim stage indicating this behavior.

Case 2 (extremely tight connection between geomembrane and surrounding material)

In this case, the friction angle at both sides is set to 90°. The parameters of the model are shown in Tab. 4.7.

Table 4.7: Interface parameters (case 2)

Parameter	k_n, Pa/m	k_s, Pa/m	φ, °
Side 1 (below)	10^8	10^8	90
Side 2 (above)	10^8	10^8	90
Side 1 (below)	10^{10}	10^{10}	90
Side 2 (above)	10^{10}	10^{10}	90
Side 1 (below)	10^{12}	10^{12}	90
Side 2 (above)	10^{12}	10^{12}	90

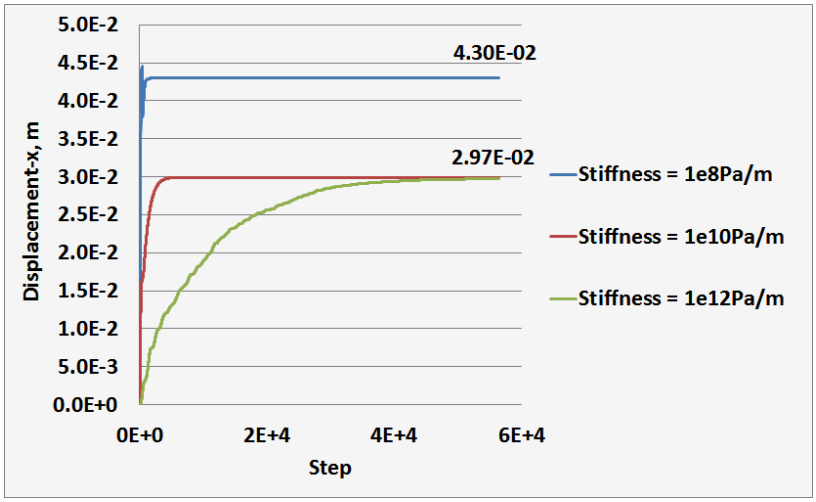

Figure 4.11: Displacements of liner node ID 7 vs. calculation steps (case 2)

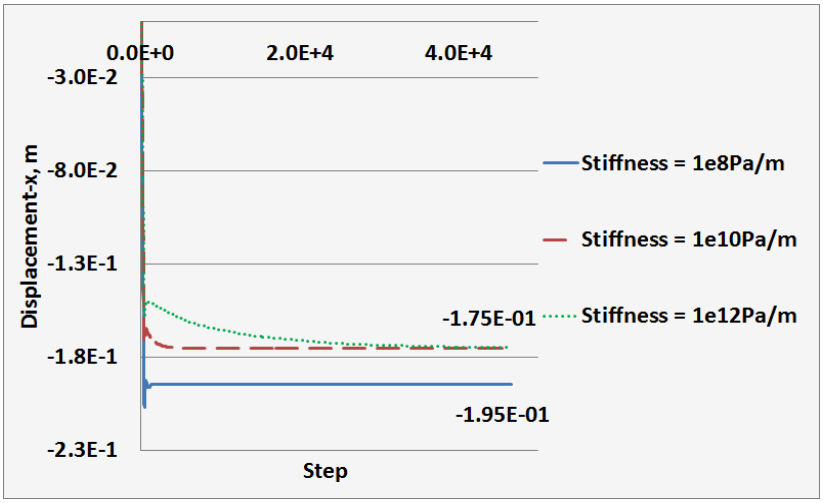

Figure 4.12: Displacements of gridpoint ID 5 vs. calculation steps (case 2)

Table 4.8: Displacements of ID 5 and ID 7 and maximum principal stress in geomembrane (case 2)

k_n=k_s, Pa/m	Liner node (ID 7) displacement, m	Gridpoint (ID 5) displacement, m	Geomembrane maximum principal stress, Pa
10^8	0.0430	0.195	$1.140 \cdot 10^7$
10^{10}	0.0297	0.175	$0.714 \cdot 10^7$
10^{12}	0.0297	0.175	$0.713 \cdot 10^7$

Due to the tight connection between the geomembrane on both sides, the displacements are small, and loading on the geomembrane is at a medium level.

Case 3 (tight connection below and extremely weak connection above the geomembrane)

The friction angle below is set to the extremely high value of 90°, whereas the friction angle below is set to 0°. The parameters of the model are shown in Tab. 4.9.

Table 4.9: Interface parameters (case 3)

Parameter	k_n, Pa/m	k_s, Pa/m	φ, °
Side 1 (below)	10^8	10^8	90
Side 2 (above)	10^8	10^8	0
Side 1 (below)	10^{10}	10^{10}	90
Side 2 (above)	10^{10}	10^{10}	0
Side 1 (below)	10^{12}	10^{12}	90
Side 2 (above)	10^{12}	10^{12}	0

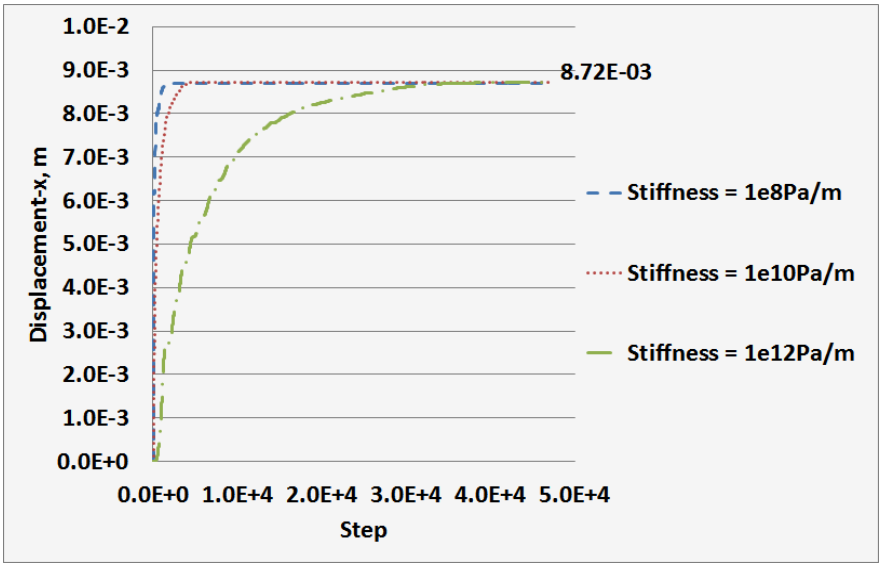

Figure 4.13: Displacements of liner node ID 7 vs. calculation steps (case 3)

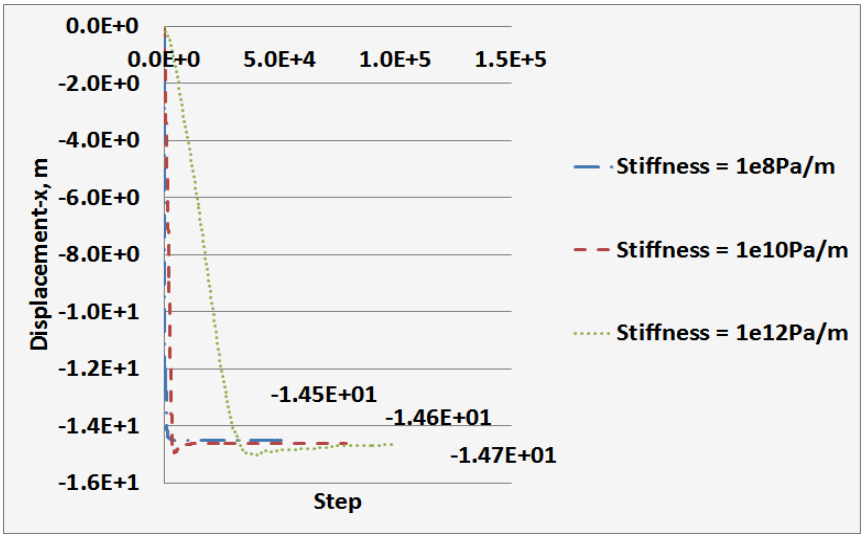

Figure 4.14: Displacements of gridpoint ID 5 vs. calculation steps (case 3)

Table 4.10: Displacements of ID 5 and ID 7 and maximum principal stress in geomembrane (case 3)

k_n=k_s, Pa/m	Liner node (ID 7) displacement, m	Gridpoint (ID 5) displacement, m	Geomembrane maximum principal stress, Pa
10^8	0.00872	14.5	$1.620 \cdot 10^6$
10^{10}	0.00872	14.6	$1.692 \cdot 10^6$
10^{12}	0.00872	14.7	$1.699 \cdot 10^6$

Results for the overlying material and the geomembrane are similar to case 1, which means free movement of overlying material and nearly no loading on the geomembrane (very small displacements and also small stresses).

Case 4 (weak connection below and extremely tight connection above the geomembrane)

The friction angle above is set to an extreme high value of 90°, and below 0°. The parameters of the model are shown in Tab. 4.11.

Table 4.11: Interface parameters (case 4)

Parameter	k_n, Pa/m	k_s, Pa/m	φ, °
Side 1 (below)	$1 \cdot 10^8$	$1 \cdot 10^8$	0
Side 2 (above)	10^8	10^8	90
Side 1 (below)	10^{10}	10^{10}	0
Side 2 (above)	10^{10}	10^{10}	90
Side 1 (below)	10^{12}	10^{12}	0
Side 2 (above)	10^{12}	10^{12}	90

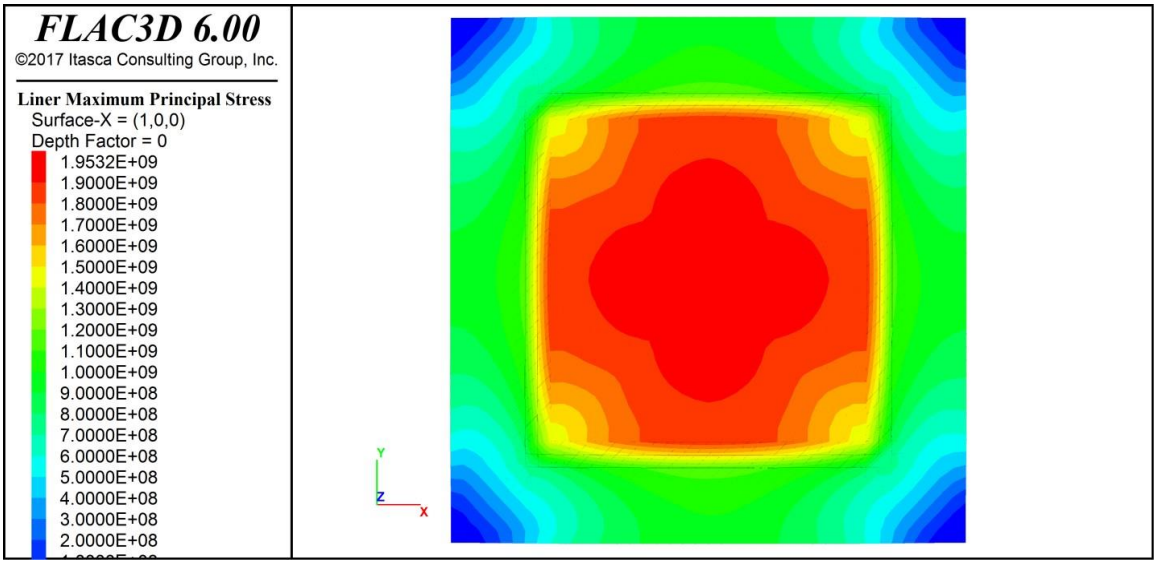

Figure 4.15: Maximum principal stress (Pa) in geomembrane (case 4)

Table 4.12: Displacements of ID 5 and ID 7 and maximum principal stress in geomembrane (case 4)

$k_n = k_s$, Pa/m	Liner node (ID 7) displacement, m	Gridpoint (ID 5) displacement, m	Geomembrane maximum principal stress, Pa
10^8	12.7	12.7	$1.959 \cdot 10^9$
10^{10}	12.9	12.5	$1.958 \cdot 10^9$
10^{12}	12.6	12.7	$1.957 \cdot 10^9$

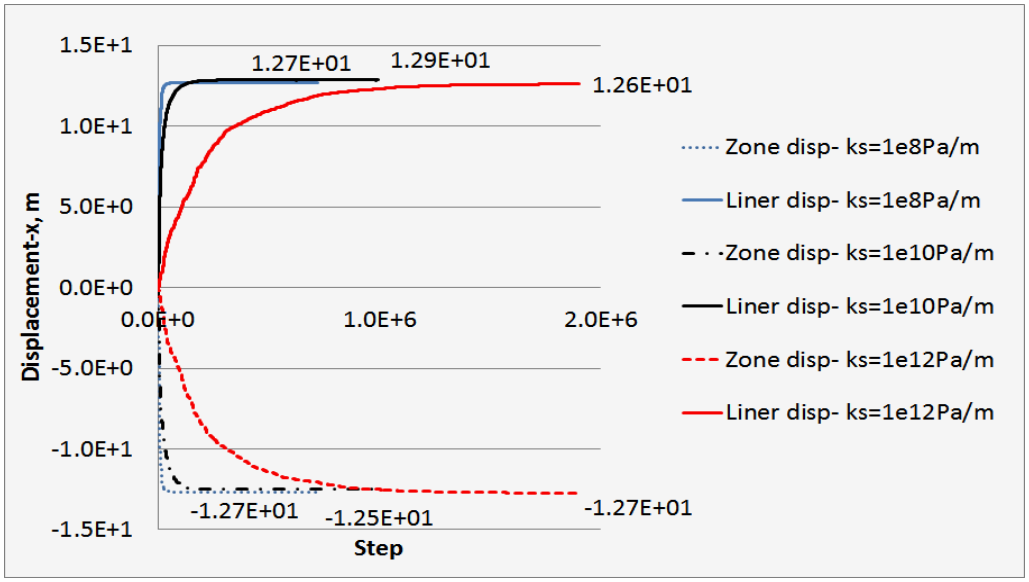

* *Notice: The solid lines refer to liner element displacements*

Figure 4.16: Displacements of liner nodes ID 7 and grid point ID 5 versus calculation steps (case 4)

In this case, the geomembrane and the bottom of the overlying material show the same displacements, somewhat lower than in cases 1 and 3. Displacements and stresses are very large.

4.3.2 Influence of interface friction

This chapter considers realistic values for friction at both sides of the geomembrane in a wider spectrum. The friction angle of one side was kept constant at 20°, 30°, or 40°, respectively, while the friction angle of the other side varied from 10° to 60°. The calculation cases with equal friction angles at both sides (20°-20°, 30°-30°, and 40°-40°) are called reference (REF) cases. Normal stiffness, k_n, and shear stiffness, k_s, were set to 10^9 Pa/m.

Case 5: Friction angle 20°:

Case 5-1: Variation of friction angle at the upper side of the geomembrane (friction angle below is fixed to 20°)

The friction angle of the interface below is kept constant at 20°, while the friction angle of the upper side of the interface varies between 10° and 60° (see Tab. 4.13). Results are shown in Fig. 4.17 and Tab. 4.13.

Table 4.13: Interface parameters (case 5-1)

Parameter	k_s, Pa/m	k_n, Pa/m	φ, °
Side 1 (below)	10^9	10^9	20
Side 2 (above)	10^9	10^9	10, 20, 30,40, 50, 60

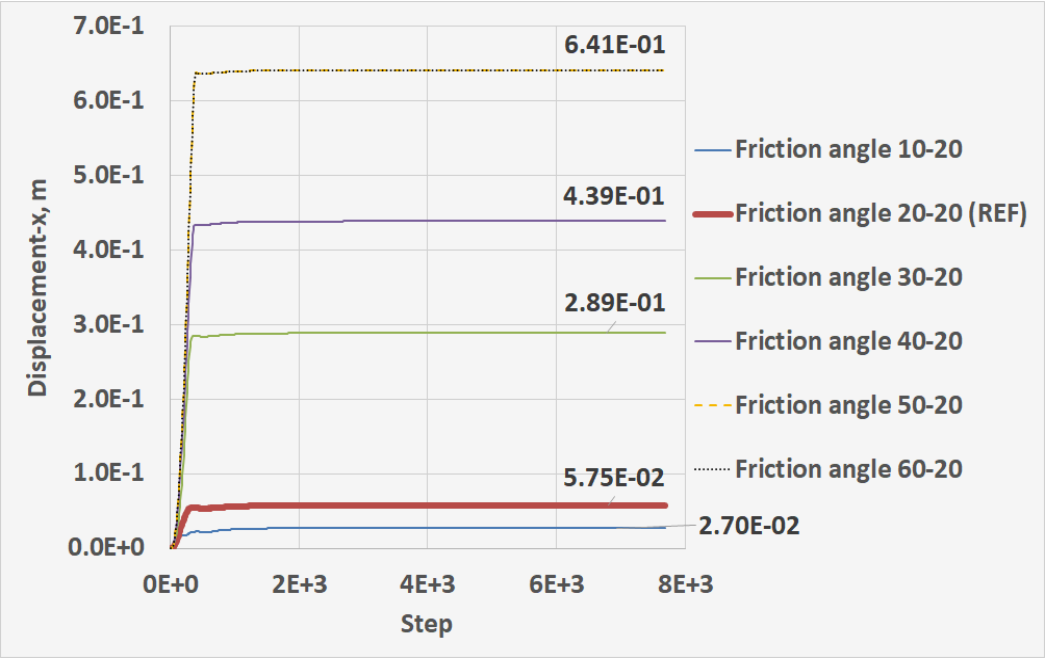

Figure 4.17: Displacements of geomembrane nodes (ID 7) vs. calculation steps (case 5-1)

Table 4.14: Liner node (ID 7) displacements and geomembrane maximum principal stress values (case 5-1)

Friction angle above and below geomembrane, φ_2 - φ_1, °	Liner node (ID 7) displacement, m	Geomembrane maximum principal stress, Pa
10-20	0.027	$7.73 \cdot 10^6$
20-20 (REF)	0.058	$2.25 \cdot 10^7$
30-20	0.289	$2.38 \cdot 10^8$
40-20	0.439	$2.799 \cdot 10^8$
50-20	0.641	$4.416 \cdot 10^8$
60-20	0.641	$4.416 \cdot 10^8$

An increase in friction angle above the geomembrane leads to increased loading of the geomembrane.

Case 5-2: Variation of friction angle at the lower side of the geomembrane (friction angle above is fixed to 20°)

The friction angle of the interface above the geomembrane is kept constant at 20°, while the friction angle of the interface below varies between 10° to 60° (see Tab. 4.15). Results are shown in Fig. 4.18 and Tab. 4.16.

Table 4.15: Interface parameters (case 5-2)

Parameter	k_s, Pa/m	k_n, Pa/m	φ, °
Side 1 (below)	10^9	10^9	10, 20, 30,40, 50, 60
Side 2 (above)	10^9	10^9	20

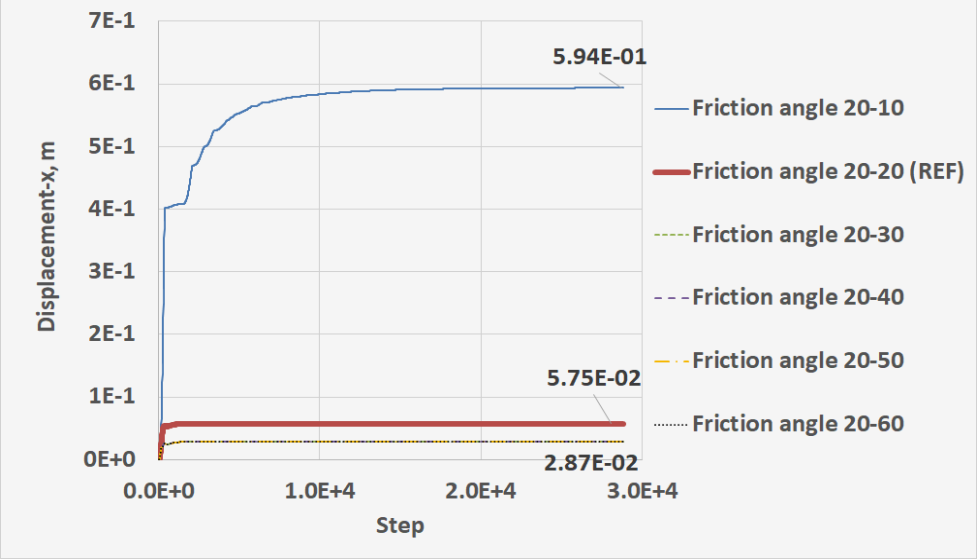

Figure 4.18: Displacements of geomembrane nodes (ID 7) vs. calculation steps (case 5-2)

Table 4.16: Liner node ID 7 displacements and maximum principal stress in geomembrane (case 5-2)

Friction angle above and below geomembrane, φ_2 - φ_1, °	Liner node (ID 7) displacement, m	Geomembrane maximum principal stress, Pa
20-10	0.594	$3.158 \cdot 10^8$
20-20 (REF)	0.058	$2.25 \cdot 10^7$
20-30	0.029	$0.726 \cdot 10^7$
20-40	0.029	$0.726 \cdot 10^7$
20-50	0.029	$0.726 \cdot 10^7$
20-60	0.029	$0.726 \cdot 10^7$

Displacements of the liner become smaller and remain constant whenever the friction angle of the side below becomes bigger than 30°.

Case 6: Friction angle 30°:

Case 6-1: Variation of friction angle at the upper side of the geomembrane (friction angle below is fixed to 30°)

The friction angle of the interface below the geomembrane is kept constant at 30°, while the friction angle of the interface above varies between 10° to 60° (see Tab. 4.17). Results are shown in Fig. 4.19 and Tab. 4.18.

Table 4.17: Interface parameters (case 6-1)

Parameter	k_s, Pa/m	k_n, Pa/m	φ, °
Side 1 (below)	10^9	10^9	30
Side 2 (above)	10^9	10^9	10, 20, 30,40, 50, 60

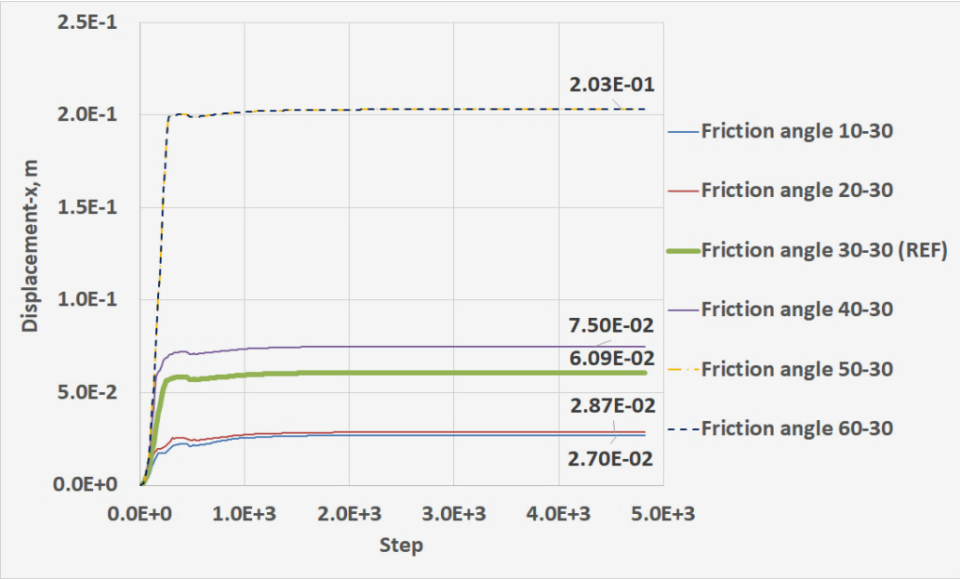

Figure 4.19: Displacements of geomembrane node (ID 7) vs. calculation steps (case 6-1)

Table 4.18: Liner node ID 7 displacements and maximum principal stress in geomembrane (case 6-1)

Friction angle above and below geomembrane, φ_2 - φ_1, °	Liner node (ID 7) displacement, m	Geomembrane maximum principal stress, Pa
10-30	0.027	$7.28 \cdot 10^6$
20-30	0.029	$7.26 \cdot 10^6$
30-30 (REF)	0.061	$2.61 \cdot 10^7$
40-30	0.075	$4.25 \cdot 10^7$
50-30	0.203	$1.31 \cdot 10^8$
60-30	0.203	$1.31 \cdot 10^8$

Loading of the geomembrane is increasing until the friction angle above the geomembrane reaches 50°.

Case 6-2: Variation of friction angle at the lower side of the geomembrane (friction angle above is fixed to 30°)

The friction angle of the interface above the geomembrane is kept constant at 30°, while the friction angle of the interface below varies between 10° and 60° (see Tab. 4.19). Results are shown in Fig. 4.20 and Tab. 4.20.

Table 4.19: Interface parameters (case 6-2)

Parameter	k_s, Pa/m	k_n, Pa/m	φ, °
Side 1 (below)	10^9	10^9	10, 20, 30,40, 50, 60
Side 2 (above)	10^9	10^9	30

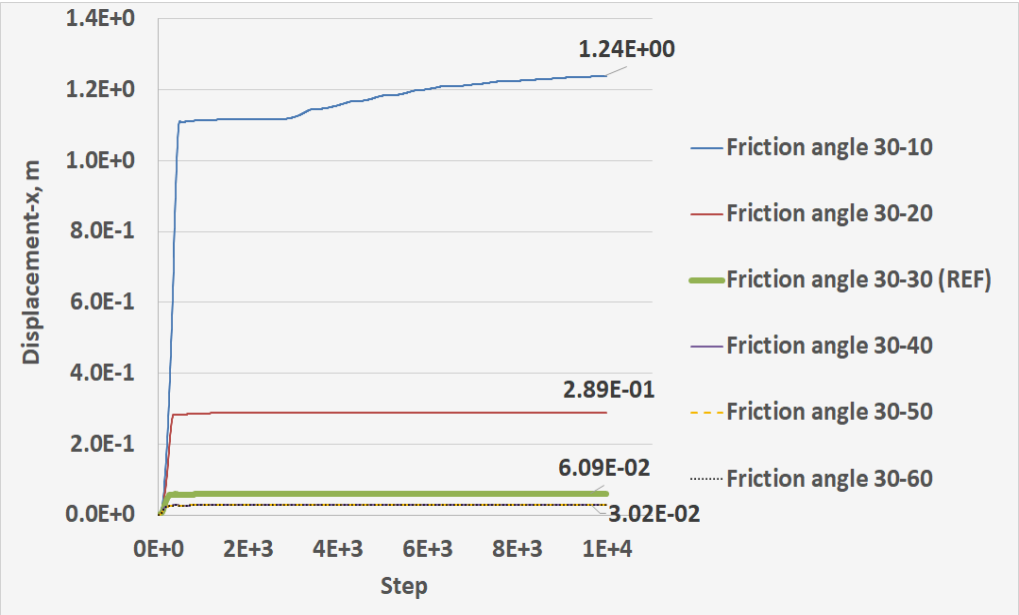

Figure 4.20: Displacements of the geomembrane nodes (ID 7) vs. calculation steps (case 6-2)

Table 4.20: Liner node ID 7 displacements and geomembrane maximum principal stress values (case 6-2)

Friction angle above and below geomembrane, φ_2 - φ_1, °	Liner node (ID 7) displacement, m	Geomembrane maximum principal stress, Pa
30-10	1.240	$7.78 \cdot 10^8$
30-20	0.289	$2.38 \cdot 10^8$
30-30 (REF)	0.061	$2.41 \cdot 10^7$
30-40	0.030	$7.22 \cdot 10^6$
30-50	0.030	$7.22 \cdot 10^6$
30-60	0.030	$7.22 \cdot 10^6$

The geomembrane loading reaches the minimum and remains constant when the friction angle below is bigger than 40^o.

Case 7: Friction angle 40^o:

Case 7-1: Variation of friction angle at the upper side of the geomembrane (friction angle below is fixed to 40^o)

The friction angle of the interface below the geomembrane is kept constant at 40°, while the friction angle of the interface above varies between 10^o to 60^o (see Tab. 4.21). Results are shown in Fig. 4.21 and Tab. 4.22.

Table 4.21: Interface parameters (case 7-1)

Parameter	k_s, Pa/m	k_n, Pa/m	φ, °
Side 1 (below)	10^9	10^9	40
Side 2 (above)	10^9	10^9	10, 20, 30, 40, 50, 60

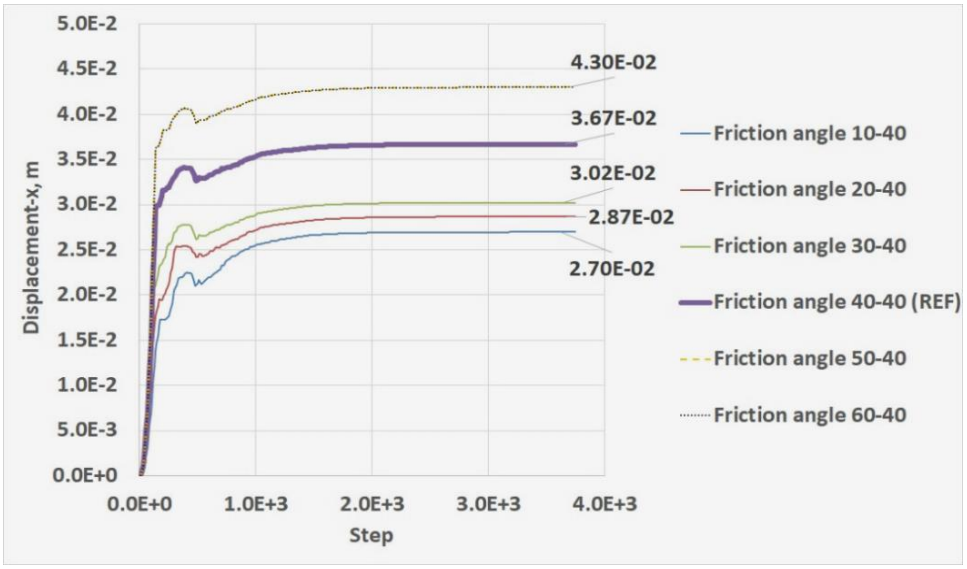

Figure 4.21: Displacements of geomembrane node (ID 7) vs. calculation steps (case 7-1)

Table 4.22: Liner node ID 7 displacements and maximum principal stress in geomembrane (case 7-1)

Friction angle above and below geomembrane, φ_2 - φ_1, °	Liner node (ID 7) displacement, m	Geomembrane maximum principal stress, Pa
10-40	0.027	$7.28 \cdot 10^6$
20-40	0.029	$7.26 \cdot 10^6$
30-40	0.030	$7.22 \cdot 10^6$
40-40 (REF)	0.037	$9.23 \cdot 10^6$
50-40	0.043	$1.38 \cdot 10^7$
60-40	0.043	$1.38 \cdot 10^7$

The geomembrane loading is only slightly increased with increasing friction angle above the geomembrane and remains constant when the friction angle above is bigger than 50°.

Case 7-2: Variation of friction angle at the lower side of the geomembrane (friction angle above is fixed to 40°)

The friction angle of the interface above the geomembrane is kept constant at 40°, while the friction angle of the interface below varies between 10° and 60° (see Tab. 4.23). Results are shown in Fig. 4.22 and Tab. 4.24.

Table 4.23: Interface parameters (case 7-2)

Parameter	k_s, Pa/m	k_n, Pa/m	φ, °
Side 1 (below)	10^9	10^9	10, 20, 30, 40, 50, 60
Side 2 (above)	10^9	10^9	40

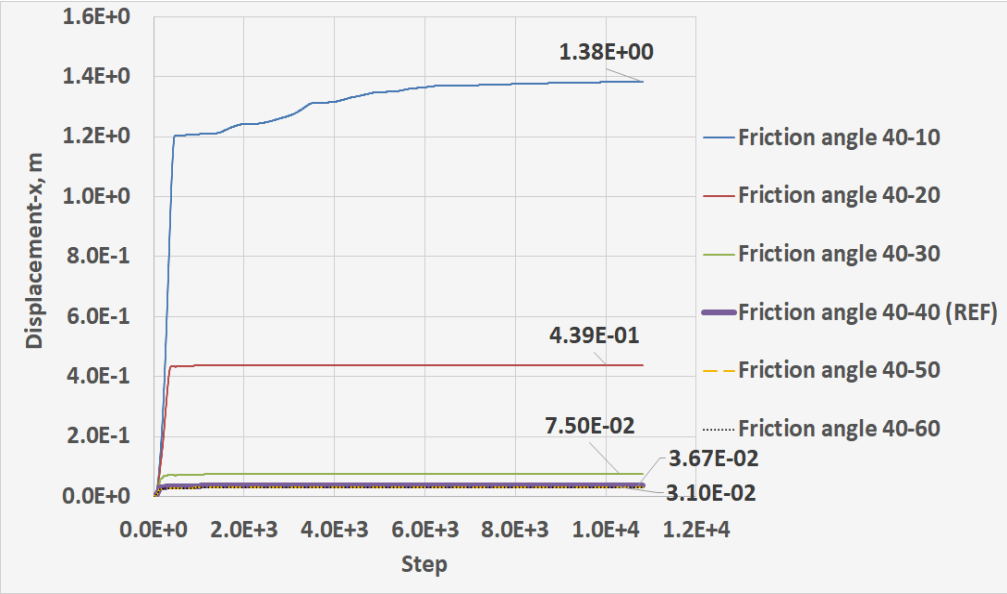

Figure 4.22: Displacements of geomembrane node (ID 7) vs. calculation steps (case 7-2)

Table 4.24: Liner node ID 7 displacements and maximum principal stress in geomembrane (case 7-2)

Friction angle above and below geomembrane, φ_2 - φ_1, °	Liner node (ID 7) displacement, m	Geomembrane maximum principal stress, Pa
40-10	1.380	$9.02 \cdot 10^8$
40-20	0.439	$2.90 \cdot 10^8$
40-30	0.075	$4.25 \cdot 10^7$
40-40 (REF)	0.037	$9.23 \cdot 10^6$
40-50	0.031	$7.04 \cdot 10^6$
40-60	0.031	$7.04 \cdot 10^6$

Loading of the geomembrane decreases with increasing friction angle below the geomembrane and remains constant when the friction angle of the side below is bigger than 50^o.

4.4 Conclusions

(1) The developed simulation scheme to model the geomembrane via a 'liner' element with two interfaces on both sides gives stable and reliable results. Even extreme scenarios can be duplicated.

(2) Interface stiffness has only a minor impact on displacements of the overlying material and geomembrane deformation (loading), whereas friction has a significant influence.

(3) Minimized loading on the geomembrane is reached when friction below the geomembrane is bigger than above, thereby minimizing friction above.

(4) Realistic prediction of geomembrane behavior (strain, loading, potential failure, etc.) needs the separate consideration of frictional contact above and below the geomembrane.

Please note that calculated stresses and displacements inside the geomembrane are unrealistic for some constellations due to the fact that only the pure elastic response of the geomembrane is assumed.This procedure was applied to (1) demonstrate the robustness of the implementation and (2) illustrate the importance of considering the frictional behavior on both sides of the geomembrane.

CHAPTER 5: CONSTITUTIVE MODEL FOR SALT DUMP

5.1 Introduction

To investigate the behavior of geomembranes under extreme mechanical loading and to validate the above-described modeling strategy, the potential application of geomembranes as sealing below huge waste dumps characterized by large time-dependent displacements and deformations, respectively, is considered. Salt waste dumps, for instance, fulfill these requirements. Therefore, constellations typical for such salt waste dumps are used as the basis for the investigations described in the following chapters.

Salt-bearing rocks have unique characteristics such as low porosity, low permeability, high ductility, and especially erratic behavior (Zhang et al., 2021). Within the scope of this study and the requirement to consider long-term behavior (e.g., a lifetime of a landfill over 100 years or even longer), creep behavior has to be considered with priority. Therefore, special constitutive models have to be chosen.

Salt creep depends on many factors, including temperature, pressure, site-specific salt minerals, grain size, impurities, age, etc. Many authors studied these factors and created appropriate constitutive models to describe the creep behavior of salt rock, such as Sjaardema et al. (1987); Callaghan G.D. (1999); Boley (1999); Olivella et al. (2002); Wachter (2009); Günther et al. (2015) or Zhang et al. (2021) – just to mention a few.

Please note that this short overview concentrates on constitutive models specially designed to model crushed rock salt or salt dump material, not natural virgin rock salt.

Sjaardema et al. (1987) conducted hydrostatic consolidation tests on wet crushed salt from the Waste Isolation Pilot Plant (WIPP) managed by the U.S. Department of Energy and developed a constitutive model based on those test results. The calculations are used to show that wet crushed salt does not significantly retard the rate of closure of shafts and drifts until the crushed salt is confined to approximately 95 percent of the intact density. An approximate method for modeling the creep velocity of intact salt is developed based on closure data from empty drifts at the WIPP site to provide a more realistic estimate of the response of crushed salt.

Callahan (1999) conducted two new laboratory experiments called shear consolidation with fractional densities close to the initial fractional density expected in the dynamically compacted

crushed salt seal (approximately 0.9). These tests expand the database to include the fractional density ranges expected in-situ and provide information on the flow behavior of the crushed salt as density increases. The expanded database was adjusted to obtain material parameters for the crushed salt constitutive model.

Boley (1999) presented a new microphysics-based creep function to capture steady-state creep that accurately captures the stress-dependent transition from pressure solution to dislocation climbing as the relevant deformation mechanism. In addition, he formulated material equations for the unsteady creep strains so that the new material law also represents the compaction process of granular rock salt. He has developed a new strength model for rate-dependent material failure that allows easy differentiation of steady-state creep and brittle fracture as a function of strain rate, stress state, and temperature. It should be emphasized that the material parameters of the new material law can be determined with the help of conventional triaxial lab tests.

Olivella et al. (2002) developed a constitutive creep model and compared it with test results. The presented constitutive model focuses on creep deformation since saline media behave ductile and time-dependent. The model is able to predict strain rates that agree well with results from laboratory tests under isotropic and oedometric conditions. Macroscopic laws are written using a nonlinear viscous approach that includes a visco-plastic component based on the critical state theory. The visco-plastic term is intended for non-creep deformation mechanisms such as grain rearrangement and comminution.

Wachter (2009) developed a constitutive model named CAPCREEP for gravel rock salt. This constitutive model equation is formulated as a superposition model and couples additionally the deformation components. The dependence of the elasticity modulus on the compaction state is considered with Hook's law for elastic deformations. The influence of deviatoric stress and temperature was combined to formulate the visco-plastic stationary shear strain rate mathematically. For the visco-plastic volumetric strain rate, the influences of hydrostatic stress state, temperature, and compaction state are multiplicatively bonded. Instantaneously, plastic strain components are simulated through a cap model. For this purpose, the rate-sensitive strength of rock salt is transformed into a strength behavior accounting for the compaction state. The cap model consists of a convex ideal-plastic cone yield surface and a convex hardening cap yield surface with an associative flow rule connected discontinuously. For the consideration of the crossing of the cap and cone yield surfaces, a special flow rule is used.

Zhang et al. (2021) gave a comprehensive review of salt rock creep properties and constitutive models. This study analyzed the permeability variation of salt rock under the coupling effect of temperature and stress; dump age mechanism, and evolution process under the effect of creep-fatigue interaction and low-frequency cyclic loading; micro deformation mechanisms of rock salt, and the relationship between microstructural variations and macroscopic creep behavior during the creep process. They established a creep damage constitutive model in a simple form with fewer parameters, easy to apply, and considering damage and self-healing ability.

Günther et al. (2015) conducted improved triaxial tests with a two-step creep procedure (loading and unloading steps) at increasing temperatures. They verified the experimental results by numerical modeling, facilitating a more reliable extrapolation of the data. The result of this study allowed a more reliable estimate of stationary creep rate in a reasonable time. The model considers all relevant deformation properties of rock salt, such as creep and damage-induced rock failure.

5.1.1 Overview of constitutive models for rock salt

Creep, in general, describes time-dependent deformations due to loading. Creep can be divided into primary (transient creep), secondary (stationary creep), and tertiary creep (creep failure), as shown in Fig. 5.1.

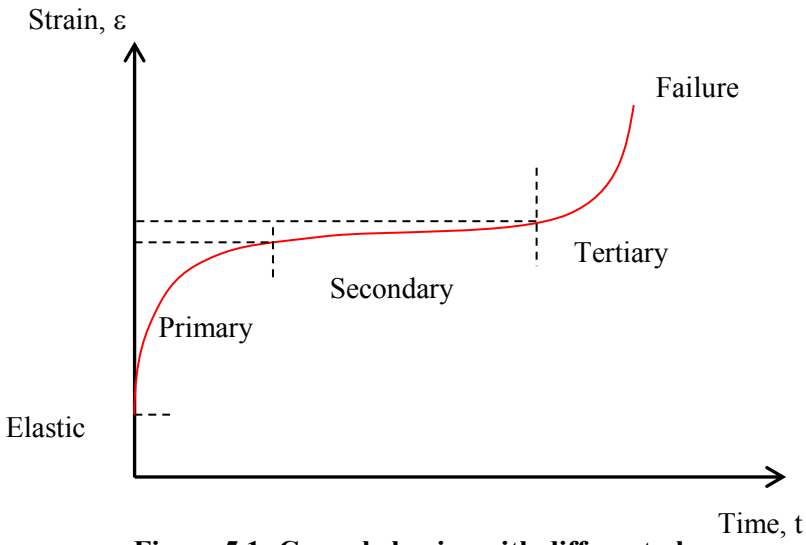

Figure 5.1: Creep behavior with different phases

Primary creep occurs short-termed (hours - days up to weeks - months) and is mainly governed by stress, moisture, and temperature. This results in a net hardening or softening. Tertiary creep (failure) is associated with microcrack development due to dilation and material damage.

Secondary creep is a steady-state mechanism and, therefore, important for long-term predictions (years or more). Both primary and steady-state creep (= secondary creep) represent the effect of dislocation motion in salt crystals (i.e., dislocation creep). For low differential stress conditions, a diffusion creep mechanism may be important.

According to Fig. 5.1, the strain ε is calculated as sum of elastic (ε^{el}), primary (ε^{pr}), secondary (ε^{sd}) and tertiary component (ε^{te}):

$$\varepsilon = \varepsilon^{el} + \varepsilon^{pr} + \varepsilon^{sd} + \varepsilon^{te} \tag{3}$$

where: ε^{el} represents elastic strain, ε^{pr} (also called transient creep strain, ε^{t}), ε^{sd} (also called stationary creep strain, ε^{s}), ε^{te} (also called creep failure strain or damage strain, ε^{d}) represents the viscous strain components.

Elastic behavior is described by Hook's law, and the elastic deformation occurs immediately after exerting load without any time delay. After unloading, the deformations recover completely. The elastic deformation is also related to a volume change (volumetric strain ε_{vol}), which corresponds to the normal octahedral stress σ_o and bulk modulus K via a linear relationship.

$$\sigma_o = \frac{1}{3}\cdot(\sigma_{xx} + \sigma_{yy} + \sigma_{zz}) = K\cdot\frac{\Delta V}{V_o} = K\cdot\varepsilon_{vol} \tag{4}$$

The elastic behavior of isotropic material can be completely expressed by the aforementioned parameters E (Young modulus), K (bulk modulus), G (shear modulus), and ν (Poisson ratio). Equation 5 and equation 6 show the relations between these four elastic constants:

$$G = \frac{E}{2(1+\nu)} \tag{5}$$

$$K = \frac{E}{3(1-2\nu)} \tag{6}$$

Visco-plastic behavior

According to Günther (2009), visco-plastic behavior occurs during the ductile deformation of rock salt. It involves the alteration of the microstructure and describes the macroscopic behavior of rock salt. In contrast to ideal crystals, the crystal lattice of real crystals contains defects (defects of the lattice geometry of the periodic order of the atoms within the crystal). Lattice defects have a great influence on the deformation behavior of real crystals. Following the spatial extension in the crystal lattice, the following defects can be distinguished: point defects (which

contain line, plane, and bulk defects), strain hardening, dislocation recovery, and damage and dilatancy.

According to equation 3, the creep deformation ε_{cr} is calculated as:

$$\varepsilon_{cr}=\varepsilon^{pr}+\varepsilon^{sd}+\varepsilon^{te} \tag{7}$$

The creep deformation rate $\dot{\varepsilon}_{\mathrm{cr}}$ is also used to describe that mechanical behavior. Odqvist et al. (1963) proposed the following equation to describe the strain hardening behavior of rock salt at the macroscopic scale:

$$\dot{\varepsilon}_{cr}= \frac{A_p}{(\varepsilon_{cr})^{\mu}} \cdot \sigma_{eff}^{n_p} \tag{8}$$

A_p is the proportionality factor that characterizes the viscosity

- μ describes the nonlinearity

- n_p is the exponent that determines the characteristic non-linear stress dependency for the creep rate

- σ_{eff} is the effective stress, given as:

$$\sigma_{eff}= \frac{3}{2}\, \dot{\varepsilon}_{cr} \cdot \frac{S_{ij}}{\dot{\varepsilon}_{ij}^{cr}} \tag{9}$$

Effective (equivalent) deformation and stress (ε_{v}, σ_{v}) are defined as follows (Backhaus, 1983):

$$\varepsilon_{eff}= \varepsilon_v= \sqrt{\frac{2}{3} \sum_{ij} \varepsilon_{ij}^2} \tag{10}$$

$$\sigma_{eff}= \sigma_v= \sqrt{\frac{3}{2} \sum_{ij} S_{ij}^2} \tag{11}$$

where: S_{ij} is the stress deviator,

$$S_{ij}=\sigma_{ij}-\frac{1}{3}\sigma_{kk}\delta_{ij} \tag{12}$$

where: δ_{ij} is the Kronecker delta,

$$\delta_{ij}=\begin{cases}0 \text{ if } i\neq j \\ 1 \text{ if } i=j\end{cases} \tag{13}$$

$$\sigma_{kk}=\sigma_{11}+\sigma_{22}+\sigma_{33} \tag{14}$$

$\dot{\varepsilon}_{cr}$ basically depends on the effective stress σ_{eff}, the temperature T, a structural parameter V which describes the hardening, and a structural parameter D which describes the damage.

$$\dot{\varepsilon}_{cr}=f(\sigma_{eff},T,V,D) \tag{15}$$

For the description of the temperature dependency of $\dot{\varepsilon}_{cr}$, very often the Arrhenius term is used:

$$f(T)=e^{-(\frac{R_g}{RT})} \tag{16}$$

In the Arrhenius term, R_g is the universal gas constant with 8.314 J/(mol K), T is the acting absolute temperature (K), and Q is the activation energy for the creep process (J/mol). The activation energy Q is temperature-dependent and increases non-linear with increasing temperature. In modeling, the assumption of mean activation energy Q = 54 kJ/mol in equation 14 is very common. This approach generally describes the temperature-dependency of creep with an accuracy that is sufficient for most practical tasks.

The actual creep phase of the material depends on the actual state of the microstructure. As long as the crystalline structure is also changing, the deformation properties change, leading to primary or transient creep, respectively, or damage-induced softening. Within a microstructural balance case, the structure does not change. Also, the deformation properties remain constant, resulting in secondary or stationary creep, respectively. The transition to a stationary microstructure is continuous and depends on whether the dislocations are eliminated, or new ones are created. In material modeling, this process can be described by means of corresponding structural parameters, which become constant during secondary creep. Material models without such a hardening parameter can only describe secondary creep but not transient creep. Since the microstructure of rock salt always strives to reach a stationary state, these simple material models are an important basic component of all complex material approaches. A few popular constitutive models applied for creep modeling of crushed or waste salt are given below:

Time-dependent strengthening model (Boresi et al., 1963) for the transient creep phase. This law describes the permanent decrease of the creep rate, which is typical for transient creep. It also considers the non-linear stress dependency.

$$\dot{\varepsilon}_{cr}^{pr}(t)=m\cdot a\cdot\sigma_{eff}^{n}\cdot t^{m-1} \tag{17}$$

where: - n is the stress exponent, e.g. n=5

- m is the time exponent, e.g. m=0.12

- a is the material constant, e.g. a=3.9·10^{-9}.

Strain-hardening models (Odqvist et al., 1963; Salzer, 1993; Hou, 1999) based on the strain-hardening model

$$\dot{\varepsilon}_{cr}^{pr} = A \frac{\sigma_{eff}^{n}}{\left(\varepsilon_{eff}\right)^{\mu}} \tag{18}$$

where: - μ describes the nonlinearity, e.g. μ=2 ÷ 7

- A is the viscosity factor, e.g. A=10^{-34}d^{-1} ÷ 10^{-21}d^{-1}

- n is the non-linear exponent, e.g. n=9 ÷ 15

Here ε_{eff} and $\dot{\varepsilon}_{cr}$ are the inelastic equivalent of deformation and deformation rates, respectively. Within this constitutive law, the transient creep rate is decreasing.

Basic rheological models

The modeling of the creep behavior by means of rheological models corresponds to the phenomenological description of the deformation behavior (e.g., elasticity, plasticity, viscosity...) without relating to the responsible physical deformation mechanism. The occurring elastic, plastic, and viscose deformation parts are described by a spring, a frictional block, and a dashpot. Within material models without damage and failure, these models contain several elements:

- Elastic isotropic compression- Hook element (spring element) time-independent, reversible:

$$\varepsilon_{ij}^{el} = \frac{1}{2G}\left(\sigma_{ij} - \frac{\nu}{1-\nu} \cdot \sigma_{kk} \cdot \delta_{ij}\right) \tag{19}$$

where: - δ_{ij} is Kronecker delta

- ν is the Poisson's ratio

- G is the shear modulus

- Visco-elastic transient deformation - Kelvin element, reversible:

$$\dot{e}_{ij}^{ve} = \frac{1}{2\eta_k} S_{ij} - \frac{G_k}{\eta_k} e_{ij}^{ve} \tag{20}$$

where: - η_k is the dynamic viscosity constant

- S_{ij} is the stress deviator

- e_{ij} is the strain deviator:

$$e_{ij}=\varepsilon_{ij}-\frac{1}{3}\varepsilon_{kk}\delta_{ij} \tag{21}$$

and $\varepsilon_{kk}=\varepsilon_{11}+\varepsilon_{22}+\varepsilon_{33}$ (22)

- Visco-plastic deformation- Maxwell element, irreversible:

$$\dot{e}_{ij}^{vp}=\frac{1}{2G_M}\dot{S}_{ij}+\frac{1}{2\eta_M}S_{ij} \tag{23}$$

The serial connection of Kelvin and Maxwell model leads to the phenomenological rheological Burgers model. In combination with the Hooke element, it depicts a basic rheological model for the creep behavior.

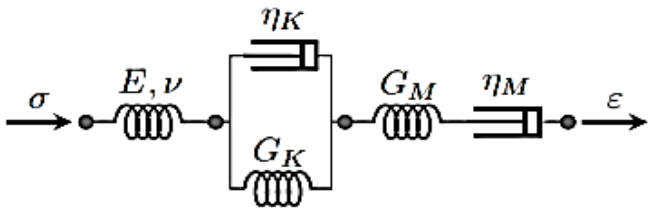

Figure 5.2: Burgers model: Rheological basic model for creep behavior of salt-like materials

Time-dependent creep-damage model (Wang, 2004) includes primary and secondary creep and an easy approach to include tertiary creep.

$$\varepsilon=\varepsilon^t+\varepsilon^s+\varepsilon^d \tag{24}$$

$$\varepsilon^t=\frac{\sigma}{C_1}\left[1-exp\left(-\frac{G}{C_2}t\right)\right] \tag{25}$$

$$\varepsilon^s=A_1\, exp\left(-\frac{Q_1}{RT}\right)\sigma^n t \tag{26}$$

$$\varepsilon^d=A_2\, exp\left(-\frac{Q_2}{RT}\right)\left(\frac{\sigma}{1-D}\right)^n t \tag{27}$$

where: - C_1 , C_2 , A_1 , A_2 , n are the material constants

- G is the shear modulus
- Q_1, Q_2 are the effective activation energies
- σ is the stress carried by the material
- t is the time
- R_g is the universal gas constant
- T is the absolute Kelvin temperature in K

- D is the damage factor, $0 \le D < 1$

WIPP model has been developed to describe the time- and temperature-dependent creep of natural rock salt. The model is described by Herrmann et al. (1980a and b). A different expression of the same creep law is given by Senseny (1985). The WIPP- reference creep law partitions the deviatoric strain-rate tensor, $\dot{\varepsilon}_{ij}^{d}$ into elastic and viscous parts ($\dot{\varepsilon}_{ij}^{de}$ and $\dot{\varepsilon}_{ij}^{dv}$), respectively.

$$\dot{\varepsilon}_{ij}^{d} = \dot{\varepsilon}_{ij}^{de} + \dot{\varepsilon}_{ij}^{dv} \tag{28}$$

The deviatoric strain rate is obtained as:

$$\dot{\varepsilon}_{ij}^{d} = \dot{\varepsilon}_{ij} - \frac{\dot{\varepsilon}_{kk}\delta_{ij}}{3} \tag{29}$$

where: - $\dot{\varepsilon}_{kk}$ is the volumetric strain rate

- δ_{ij} is the Kronecker delta (given by equation 13)

The elastic part is related to the deviatoric stress rate,

$$\dot{\varepsilon}_{ij}^{de} = \frac{\dot{\sigma}_{ij}^{d}}{2G} \tag{30}$$

where G is the elastic shear modulus.

The viscous part of the deviatoric strain rate is coaxial with the deviatoric stress tensor and is given by:

$$\dot{\varepsilon}_{ij}^{dv} = \frac{3}{2}\left\{\frac{\sigma_{ij}^{d}}{\bar{\sigma}}\right\}\dot{\varepsilon} \tag{31}$$

The scalar strain rate $\dot{\varepsilon}$ is composed of two parts, $\dot{\varepsilon}_p$ and $\dot{\varepsilon}_s$, corresponding to primary and secondary creep, respectively,

$$\dot{\varepsilon} = \dot{\varepsilon}_p + \dot{\varepsilon}_s \tag{32}$$

The primary creep rate depends on the magnitude of the secondary creep rate:

$$\dot{\varepsilon}_p = \begin{cases} \left(A - B\varepsilon_p\right)\dot{\varepsilon}_s \ \ if\ \dot{\varepsilon}_s > \dot{\varepsilon}_{ss}^{*} \\ \left(A - B\dfrac{\dot{\varepsilon}_{ss}^{*}}{\dot{\varepsilon}_s}\varepsilon_p\right)\dot{\varepsilon}_s \ \ if\ \dot{\varepsilon}_s < \dot{\varepsilon}_{ss}^{*} \end{cases} \tag{33}$$

The secondary creep rate is:

$$\dot{\varepsilon}_s = D\bar{\sigma}^n e^{-\frac{Q}{RT}} \tag{34}$$

where: - D, n, A, B and $\dot{\varepsilon}_{ss}^*$ are material constants,

- Q, R_g, T are the parameters as given for equation 16

- $\bar{\sigma}$ is the Von Mises stress

5.1.2 Overview of constitutive models for crushed salt

WIPP-crushed salt model is based on the model described by Sjaardema et al. (1987), with an added deviatoric component as proposed by Callahan and DeVries (1991). This model simulates volumetric and deviatoric creep compaction behavior. The primary creep rate is given by equation 33.

where A, B, $\dot{\varepsilon}_{ss}^*$ are the material constants

$A = 4.56$; $B = 127$; $\dot{\varepsilon}_{ss}^* = 5.39 \cdot 10^{-8}$ (s^{-1})

The secondary creep strain rate has the following form:

$$\dot{\varepsilon}_s = D\left(\frac{\bar{\sigma}}{F_d}\right)^n \cdot e^{-\frac{Q}{R_g T}} \tag{35}$$

where: - $\bar{\sigma}$ is the deviatoric stress magnitude

- F_d is the fractional density, defined as the ratio between the actual and ultimate salt density

- Q, R_g, T are the parameters as given by equation 16

A crushed salt model with creep, compaction, and strain softening by Lüdeling et al., 2014 implicates viscous compaction and intact salt behavior such as creep and visco-plastic deformation with strain hardening and softening. The sketch of the model is shown in Fig. 5.3.

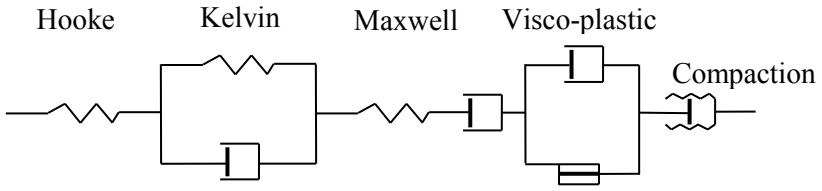

Figure 5.3: Sketch of the crushed salt model (Lüdeling et al., 2014)

In this model, the elasto-visco-plastic part consists of the Burgers model (formed by Hook, Kelvin, and Maxwell elements), which describes primary and secondary creep; the visco-plastic

element comprises a dashpot parallel to a Minkley slider element. The compaction rate $\dot{\boldsymbol{\varepsilon}}^{\mathbf{c}}_{\mathbf{ij}}$ of this model is defined as:

$$\dot{\varepsilon}^{c}_{ij}=C_o(1-e^{-C_1\sigma_o})\frac{e^{C_2P}-1}{1-P}\cdot\left[\delta_{ij}-\frac{3\sqrt{2}}{\sqrt{9\sigma_o^2+\sigma_{eff}^2}}\sigma^{d}_{ij}\right] \tag{36}$$

where: - σ^{d}_{ij} is the deviatoric stress

- σ_{eff} is the effective stress
- σ_o is the average isotropic stress
- P is the porosity
- δ_{ij} is the Kronecker delta (given in equation 11

C_o, of dimension (time)$^{-1}$, determines the overall rate, while C_1 (dimension (stress)$^{-1}$) and C_2 (dimensionless) give the dependence on isotropic stress and porosity. Those parameters are related to the b_i parameter in Sjaardema et al.'s (1987) model:

$$C_o=\frac{1}{3}b_o\frac{e^{B_2\rho_f}}{\rho_f}\ ;\ C_1=b_1\ ;\ C_2=-b_2\rho_f \tag{37}$$

where: - ρ_f is the density of intact salt

VISCOSALT2017 constitutive model was developed by Leppla (2021) for granular crushed salt. The constitutive law is based on a superposition that considers the dependency of stress, time, temperature, and density, including the effect of the time and stress-dependent compaction. The total strain (ε_{ij}) consists of instantaneous elastic (ε^{el}_{ij}), instantaneous plastic (ε^{pl}_{ij}) and visco-plastic (ε^{vpl}_{ij}) parts as shown in equation 38

$$\varepsilon_{ij}=\varepsilon^{el}_{ij}+\varepsilon^{pl}_{ij}+\varepsilon^{vpl}_{ij} \tag{38}$$

The instantaneous elastic strain is calculated by Hook's law, see equation 19.

For the instantaneous plastic strain, a cap model is used (Wallner, 1983). The visco-plastic strain consists of two parts, the deviatoric strain e, and the volumetric strain ε_{kk}. The deviatoric strain is affected by the deviatoric stress. The deviatoric strain consists of the transient part and the stationary part

The visco-plastic transient deviatoric strain rate $\dot{e}^{vpl,tr}_{ij}$ is defined as:

$$\dot{e}_{ij}^{vpl,tr} = \frac{D_1 \cdot n_{max}}{C_1'} \cdot e^{-\frac{t}{C_1}} \tag{39}$$

where: - n_{max} is the maximum pore volume

- C_1' and D_1 are constants determined by mathematical functions of regression analysis of load-controlled triaxial creep tests
- t is the time

The visco-plastic stationary strain rate $\dot{e}_{ij}^{vpl,st}$ is defined as:

$$\dot{e}_{ij}^{vpl,st} = e^{-\frac{Q}{RT}} \cdot \left[B_1 s + (B_2 \cdot s^{B_4} - B_1 \cdot s) \cdot \tanh(B_3 \cdot s) \right] \tag{40}$$

where: - B_1 to B_4 are constants determined by mathematical functions of regression analysis of load-controlled triaxial creep tests

- Q, R, T are the Arrhenius parameters as given by equation 16
- s is the deviatoric stress

The visco-plastic volumetric strain rate $\dot{\varepsilon}_{kk}^{vpl}$ is defined as:

$$\dot{\varepsilon}_{kk}^{vpl} = e^{-\frac{Q}{RT}} \cdot E_7 \cdot e^{E_8 \cdot I_1} \cdot \left(\ln \frac{\varepsilon_{kk,\,max}}{\varepsilon_{kk,\,max} - \varepsilon_{kk}} \right)^{-\left(E_5 + E_6 \cdot \varepsilon_{kk,\,max}\right)} \tag{41}$$

where: - Q, R, T are the Arrhenius parameters as given by equation 16

- I_1 is the first stress invariant
- E_5 to E_8 are constants determined by mathematical functions of regression analysis of load-controlled triaxial creep tests.
- $\varepsilon_{kk,\,max}$ is the maximum volumetric strain
- ε_{kk} is the volumetric strain

Besides those, there are many other constitutive models for rock salt or crushed salt, such as Norton power-law model (Norton, 1929), BGR model (Hunsche et al., 1994), Multimechanism Deformation model (Munson et al., 1979), Lubby2 model (Hou, 1997), Günther/Salzer model (Günther et al., 2015), Minkley model (Minkley et al., 2012), etc.

In this thesis, a new constitutive model called “Femesalz” based on the WIPP-salt model was developed to describe the specific creep behavior of a salt dump.

5.2 'Femesalz' constitutive model for crushed salt

5.2.1 Introduction

In order to simulate a geomembrane embedded under a salt dump, it is necessary to choose a suitable visco-elasto-plastic model for the above-situated waste dump to consider long-term creep behavior. In this chapter, a new constitutive law for mapping the behavior of piling salt for use in FLAC^{3D} is proposed. In addition to primary and secondary creep, this material law also includes changes in strength properties (cohesion, angle of friction, tensile strength, and angle of dilatation) dependent on the stress state. This means that softening and failure are also mapped.

The determination of the model parameters is based on lab tests performed with crushed salt. The laboratory tests, performed at the Rockmechanical Lab of the Geotechnical Institute of TU Bergakademie Freiberg comprised compaction tests on samples obtained from different positions inside a salt dump (Itasca, 2017). The determined characteristic values were used to determine the parameters for the constitutive law used for the studies documented in this thesis.

The constitutive law 'FemeSalz' is based on the CWIPP model approach (Itasca, 2016) and some extensions (Itasca, 2017). The constitutive model simulates primary and secondary creep as well as volumetric compaction (densification) of granular rock salt, but also includes plastic failure based on a Mohr-Coulomb failure criterion with hardening and softening. This makes it possible to depict real-time- and stress-dependent behavior.

The starting point for the development of the constitutive law is the total strain ε as the sum of the elastic, plastic, and viscous components:

$$\varepsilon = \varepsilon_{el} + \varepsilon_{v} + \varepsilon_{pl} \tag{42}$$

The mean stress σ_m and the von Mises equivalent stress σ_{eq} are used to describe the current stress state:

$$\sigma_m = \frac{1}{3} \cdot (\sigma_1 + \sigma_2 + \sigma_3) \tag{43}$$

$$\sigma_{eq} = \sqrt{\frac{2}{3} (\sigma_1 - \sigma_2)^2 + (\sigma_2 - \sigma_3)^2 + (\sigma_3 - \sigma_1)^2} \tag{44}$$

where σ_i are the principal stresses (i = 1, 2, 3; $\sigma_1 > \sigma_2 > \sigma_3$).

The current degree of compaction (fractional density), F_d, results from the ratio of the current density to the maximum achievable density of the fully compacted salt. Cohesion, friction angle,

dilatation angle, and tensile strength are dependent on compaction and deformation since states of failure (softening effect) and compaction (hardening effect) counteract. The hardening behavior is described by *Table* F_d (depending on the degree of compaction) and the softening is described by *Table* ε_{pl} (depending on the plastic deformation). The mostly non-linear relationships are controlled via these tables. The current parameter values are determined as follows:

$$Parameter\ value = Table_{F_d}(F_d) + F_d \cdot (Table_{pl}(\varepsilon_{pl}) - Table_{pl}(0)) \tag{45}$$

The compaction rate ($\dot{\varepsilon}_{v,c}$) is described with an exponential approach:

$$\dot{\varepsilon}_{v,c} = \frac{1}{\rho} \cdot b_0 \cdot \left(1 - e^{-b_1 \cdot \sigma_m}\right) \cdot e^{-b_2 \cdot \rho} \tag{46}$$

It depends on the current density ρ of the material and the mean stress σ_m. To describe compaction behavior, three empirical parameters b_o in kg/(s·m³), b_1 in Pa, and b_2 in kg/m³ are determined via isostatic compaction tests. In the case of residual salts, other influences during compaction (e.g., moisture content) may have to be considered. For this purpose, a calibration based on in-situ data is indicated.

The stationary (secondary) creep rate ($\dot{\varepsilon}_s$) as an essential mechanism in long-term behavior follows a modified approach according to Norton (1929):

$$\dot{\varepsilon}_s = D \cdot \left(\frac{\sigma_{eq}}{p_0 \cdot F_d}\right)^n \tag{47}$$

where: - D is a structural parameter in 1/s, σ_{eq} is the equivalent stress in Pa,

- p_o is a dimensional constant in Pa and n is the stress exponent.

The primary creep rate $\dot{\varepsilon}_p$ is defined by equation 33.

$$\dot{\varepsilon}_p = \begin{cases} \left(A - B\,\varepsilon_p\right)\dot{\varepsilon}_s & if \quad \dot{\varepsilon}_s \geq \dot{\varepsilon}_{ss}^* \\ \left(A - B\,\varepsilon_p\,\frac{\dot{\varepsilon}_{ss}^*}{\dot{\varepsilon}_s}\right)\dot{\varepsilon}_s & if \quad \dot{\varepsilon}_s < \dot{\varepsilon}_{ss}^* \end{cases} \tag{48}$$

where: - A and B are the dimensionless material constants

- $\dot{\varepsilon}_{ss}^*$ is the critical creep rate (given in equation 28)

An additional plastic flow function acts for potential shear failure:

$$f_s = \sigma_3 - \sigma_1 \cdot N_\phi + 2 \cdot c \cdot \sqrt{N_\phi} \tag{49}$$

where: - c is the cohesion,

- ϕ is the internal friction angle

$$N_\phi = \frac{1+\sin\phi}{1-\sin\phi} \tag{50}$$

The potential plastic function is defined as:

$$g_s = \sigma_3 - \sigma_1 \cdot N_\psi \tag{51}$$

where: - ψ is the dilatancy angle:

$$N_\psi = \frac{1+\sin\psi}{1-\sin\psi} \tag{52}$$

The plastic behavior for tensile stress failure is described by the yield function:

$$f_t = \sigma_t - \sigma_1 \tag{53}$$

The corresponding plastic potential function is: $g_t = -\sigma_t$

The tensile strength cannot be greater than the maximum possible tensile strength resulting from internal friction angle and cohesion:

$$\sigma_{t,\,max} = \frac{c}{\tan\phi} \tag{54}$$

A direct temperature dependency was not considered in the model approach. However, it can be integrated without bigger problems. The shear and bulk modulus of the salt are also dependent on compaction:

$$K = K_f \cdot e^{K_1(\rho - \rho_f)} \tag{55}$$

$$G = G_f \cdot e^{G_1(\rho - \rho_f)} \tag{56}$$

where: - K is the current bulk modulus,

- K_f is the bulk modulus for intact salt,

- K_1 is a material parameter in 1/(kg/m³),

- G is the shear modulus,

- G_f is the shear modulus for intact salt,

- G_1 is a material parameter in 1/(kg/m³),

- ρ the current density,

Table 5.1 provides all the input parameters of the FemeSalz model. So-called state variables, listed in Tab. 5.2, are used to evaluate the current compaction and plasticity state of the individual

zones. The constitutive law was programmed in C^{++} and is available as a Dynamic Link Library (dll). Compaction and triaxial tests were performed to verify the new salt constitutive model.

Table 5.1: Material parameters for 'FemeSalz' constitutive law

Name	**Explanation**
Bulk	Bulk modulus *K*(*)
Shear	Shear modulus *G*(*)
b-f	Bulk modulus intact salt K_f, Pa
s-f	Shear modulus of the intact salt G_f, Pa
b_o	Creep compaction parameter, kg/(s·m^3)
b_1	Creep compaction parameter, Pa
b_2	Creep compaction parameter, kg/m^3
a-wipp	Structural parameter *A* in primary creep
b-wipp	Structure parameter *B* in primary creep
crit_steady-state_creep_rate	Critical creep rate $\dot{\varepsilon}_{ss}^{*}$ in primary creep
d-wipp	Structure parameter *D* in stationary creep, s^{-1}
n-wipp	Stress exponent n in steady-state creep
Cohesion	Cohesion *c* (*), Pa
Friction	Friction angle ϕ (*), ^{o}
Dilatancy	Dilatation angle δ (*), ^{o}
Tension	Tensile strength σ_t (*), Pa
Rho	Density ρ (*), kg/m^3
rho-f	Density ρ_f of the intact salt, kg/m^3
c-ctable	Table ID for cohesion gain on compaction
c-ftable	Table ID for friction angle increase on compaction
c-dtable	Table ID for dilatancy angle increase on compaction
c-ttable	Table ID for tensile strength increase on compaction
y-ctable	Table ID for cohesion decrease in plastic distortion
y-ftable	Table ID for friction angle decrease at plastic distortion
y-dtable	Table ID for dilatancy angle decrease at plastic distortion
y-ttable	Table ID for tensile strength decrease in plastic distortion
Only readable:	
degree of compaction	The current degree of compaction
akk-plast-shear strain	Accumulated plastic shear strain
akk-plast tensile strain	Accumulated plastic tensile strain
prim-creep-rate	Primary creep rate
prim-creep-strain	Primary creep strain

(*) - Variable during calculation

Table 5.2: Zone state indicators for constitutive law 'FemeSalz'

Bit	**State**
1	Shear failure current (shear-n)
2	Tensile failure current (tension-n)
4	Shear failure past (shear-p)
8	Tensile failure past (tension-p)
64	Compaction actual (compaction-n)
128	Compaction past (compaction-p)

5.2.2 Compaction test

The compaction test was performed with a block of 1 x 1 x 1 m, as shown in Fig. 5.4. The block is fixed in the horizontal directions, and the vertical displacement is fixed at the bottom. The vertical compressive stress of $2.5 \cdot 10^6$ Pa was applied at the upper side. A creep time of up to 1 year was considered. Large-strain and creep options were used. Several constitutive models were applied: WIPP-law (considered as constitutive reference model), WIPP-crushed-salt-law, and 'FemeSalz'-law.

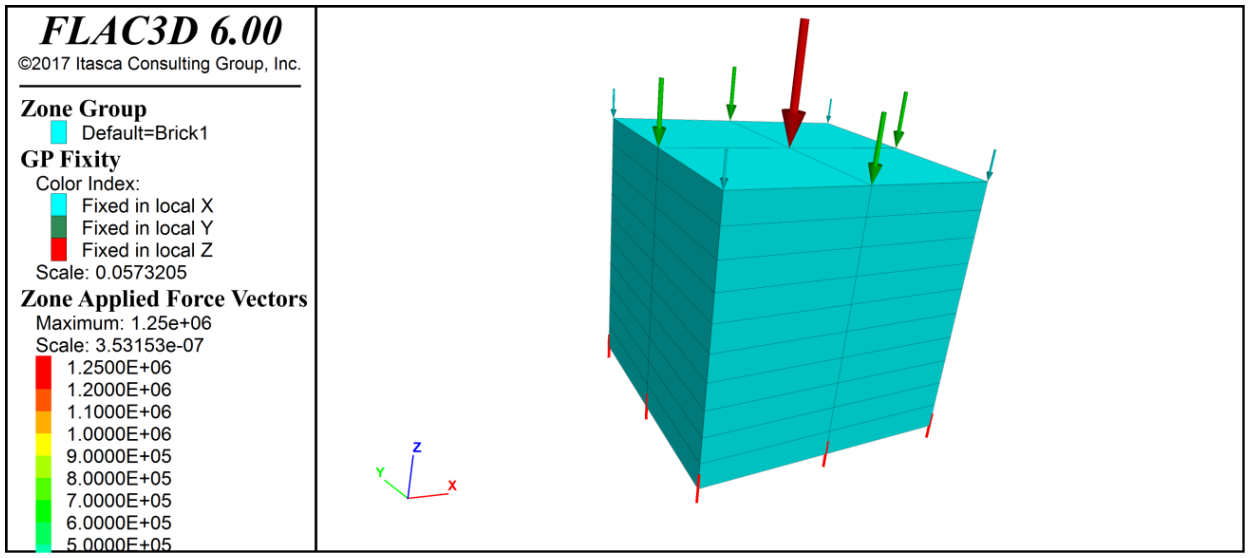

Figure 5.4: Set-up of compaction test

The maximum vertical displacement was captured after one day, one month, and one year for comparison. Simulation cases are shown in Tab. 5.3 and material properties are shown in Tab. 5.4. The results of the simulations are documented in Tab. 5.5 and Tab. 5.6.

Table 5.3: Simulation cases

Constitutive model		***G, K, ρ***	**Volumetric compaction**	**Calibrated tables**
Case 1	**WIPP (REF)**	constant	without	without
Case 2	**WIPP-crushed salt**	constant	without	without
Case 3	**WIPP-crushed salt**	varies	with	without
Case 4	**'FemeSalz'**	constant	without	without
Case 5	**'FemeSalz'**	varies	with	without
Case 6	**'FemeSalz'**	varies	with	with

Table 5.4: Material parameters for different simulation cases (see Tab. 5.3)

Case	Case 1	Case 2	Case 3	Case 4	Case 5	Case 6
Constitutive model	**WIPP (REF)**	**WIPP-crushed salt**	**WIPP-crushed salt**	**'Feme-Salz'**	**'Feme-Salz'**	**'FemeSalz'**
K, Pa	$4\cdot10^{9}$	$4\cdot10^{9}$	$4\cdot10^{9}$	$4\cdot10^{9}$	$4\cdot10^{9}$	$4\cdot10^{9}$
G, Pa	$2.8\cdot10^{9}$	$2.8\cdot10^{9}$	$2.8\cdot10^{9}$	$2.8\cdot10^{9}$	$2.8\cdot10^{9}$	$2.8\cdot10^{9}$
a-wipp	4.56	4.56	4.56	4.56	4.56	4.56
b-wipp	127	127	127	127	127	127
d-wipp, s^{-1}	$2\cdot10^{-32}$	$2\cdot10^{-32}$	$2\cdot10^{-32}$	$3.6\cdot10^{-41}$	$3.6\cdot10^{-41}$	$3.6\cdot10^{-41}$
n-wipp	4.9	4.9	4.9	4.9	4.9	4.9
$\dot{\varepsilon}^{*}_{ss}$, s^{-1}	$5.39\cdot10^{-8}$	$5.39\cdot10^{-8}$	$5.39\cdot10^{-8}$	$5.39\cdot10^{-8}$	$5.39\cdot10^{-8}$	$5.39\cdot10^{-8}$
T, K	300	300	300	300	300	300
R	1.987	1.987	1.987	1.987	1.987	1.987
Q, J	12000	12000	12000	12000	12000	12000
rho, kg/m^3	1600	1600	1600	1600	1600	1600
rho-f, kg/m^3	-	1600	2000	1600	2000	2000
G_f, Pa	-	$2.8\cdot10^{9}$	$14.0\cdot10^{9}$	$2.8\cdot10^{9}$	$14.0\cdot10^{9}$	$14.0\cdot10^{9}$
K_f, Pa	-	$4.0\cdot10^{9}$	$20.0\cdot10^{9}$	$4.0\cdot10^{9}$	$20.0\cdot10^{9}$	$20.0\cdot10^{9}$
b_0, $kg/s.m^3$	-	0	$2.0\cdot10^{8}$	0	$2.0\cdot10^{8}$	$2.0\cdot10^{8}$
b_1, Pa	-	$2\cdot10^{-13}$	$2\cdot10^{-13}$	$2\cdot10^{-13}$	$2\cdot10^{-13}$	$2\cdot10^{-13}$
b_2, kg/m^3	-	$-1.1\cdot10^{-2}$	$-1.1\cdot10^{-2}$	$-1.1\cdot10^{-2}$	$-1.1\cdot10^{-2}$	$-1.1\cdot10^{-2}$
Tables						**ID- pair value**
c-ctable	-	-	-	-	-	10 - (0; $2\cdot10^{4}$) (1; $8\cdot10^{5}$)
c-ftable	-	-	-	-	-	11 - (0; 30) (1; 45)
c-dtable	-	-	-	-	-	12 - (0; 0) (1; 0)
c-ttable	-	-	-	-	-	13 - (0; $1\cdot10^{4}$) (1; $4\cdot10^{5}$)
y-ctable	-	-	-	-	-	20 - (0; $8\cdot10^{5}$) (0.01; $8\cdot10^{5}$) (0.1; $4\cdot10^{5}$) (10;10^{5})
y-ftable	-	-	-	-	-	21 - (0; 45) (0.01; 35) (0.1; 30) (10; 30)
y-dtable	-	-	-	-	-	22 - (0; 5) (0.01; 15) (0.1; 0) (10; 0)
y-ttable	-	-	-	-	-	23 - (0; $4\cdot10^{5}$) (0.05; 10^{5}) (0.1 10^{2}) (10; 0)

Table 5.5: Results of simulations using 3 constitutive models without compaction

Case		Case 1	Case 2	Case 4
Constitutive model		WIPP (REF)	WIPP-salt	'FemeSalz'
Maximum x-displacement, m	1 day	$7.11\cdot10^{-4}$	-	-
	1 month	-	$7.11\cdot10^{-4}$	$5.74\cdot10^{-4}$
	1 year	$6.60\cdot10^{-3}$	$6.60\cdot10^{-3}$	$6.44\cdot10^{-3}$

Table 5.6: Results of simulation using 3 constitutive models with compaction

Case		Case 3	Case 5	Case 6
Constitutive model		WIPP-salt	'FemeSalz'	'FemeSalz' (with calibrated tables)
Maximum x-displacement, m	1 month	$2.04 \cdot 10^{-3}$	$9.17 \cdot 10^{-3}$	$9.17 \cdot 10^{-3}$
	1 year	$1.99 \cdot 10^{-2}$	$1.80 \cdot 10^{-2}$	$1.80 \cdot 10^{-2}$

According to the calculation results given in Tab. 5.4 and Tab. 5.5, for the different models, the maximum z-displacement values show no significant difference in relation to the reference model (WIPP). For the simulations without compaction, the models applying WIPP and WIPP-crushed-salt constitutive law have a maximum z-displacement after 1 year of 0.0066043 m, while for the 'FemeSalz' model, it is 0.0064379 m. For simulations with compaction, the maximum z-displacement of the WIPP-salt model is 0.019859 m, and that of 'FemeSalz' is 0.01799 m. The 'FemeSalz' model with calibrated tables also gives the same maximum z-displacement of 0.01799 m. This shows that the improved 'FemeSalz' constitutive model duplicates the creep behavior according to the WIPP-salt law.

5.2.3 Triaxial test and realistic waste dump simulation

The required parameters were determined via laboratory tests. A recalibration based on in-situ measurements in specific cases is advisable. The test was carried out following the relevant standards and guidelines like ISRM recommendations. The laboratory tests have been back analyzed via simulations. The model set-up of a classical triaxial test is shown in Fig. 5.5, and the applied input parameters are given in Tab. 5.4.

The numerical simulation of triaxial laboratory tests is carried out with a homogeneous model with 1 m width and height of 2 m. The model consists of 54 zones in total. Vertical displacement is fixed at the bottom of the model, and stress boundary conditions are applied to the other model faces.

Most parameters are relatively robust against changes in model geometry or resolution. However, some are not. Each specific model has to be regarded as an individual case. For instance: the stationary creep rate is strongly dependent on the salt dump geometry itself and the surface shape of the subsoil. Here, a recalibration of the corresponding parameter d-wipp for the final geometry must be carried out.

Fig. 5.6 shows the creep rates of a corresponding parameter study with d-wipp = $DW \cdot 10^{-42}$ (DW varies between 1 and 8). An almost linear dependency on DW can be clearly seen. Firstly, with this type of parameter study, the material properties are set so that the model behavior is

realistically depicted. Secondly, it enables the use of regression results which makes adjustments quick and easy.

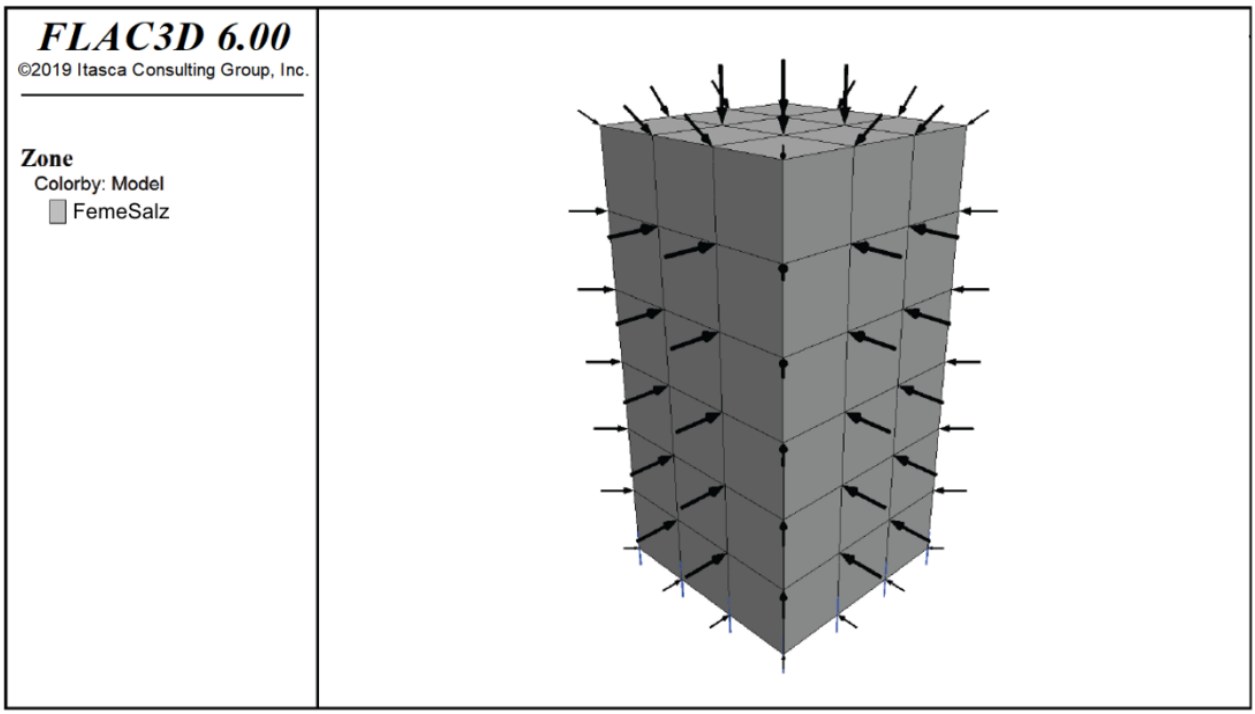

Figure 5.5: Model for simulating a triaxial test

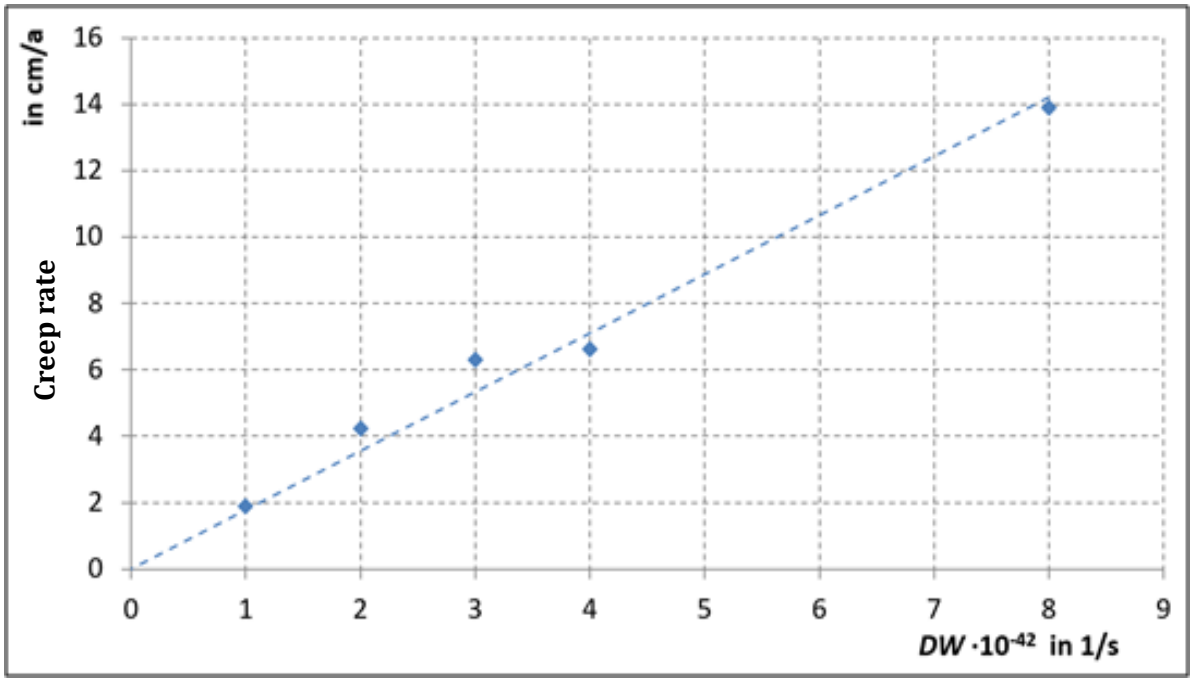

Figure 5.6: Results of parameter study: Creep rate at bottom of salt dump as function of DW (d-wipp = DW·10^{-4})

5.2.4 Numerical salt dump simulations

A realistic salt dump model is set up with an assumed installation of a geomembrane (here represented in a simplified manner only by an interface) at the bottom of the salt dump. The model geometry (see Fig. 5.7) is based on a real typical in-situ situation and created for carrying out comparative calculations. The model consists of a 180 m height salt dump and a ground with 3 layers. The 3 layers (downwards from the surface: 0 – 6 m, 6 – 50 m, and 50 m down to the model bottom) are named Soil I, Soil II, and Soil III.

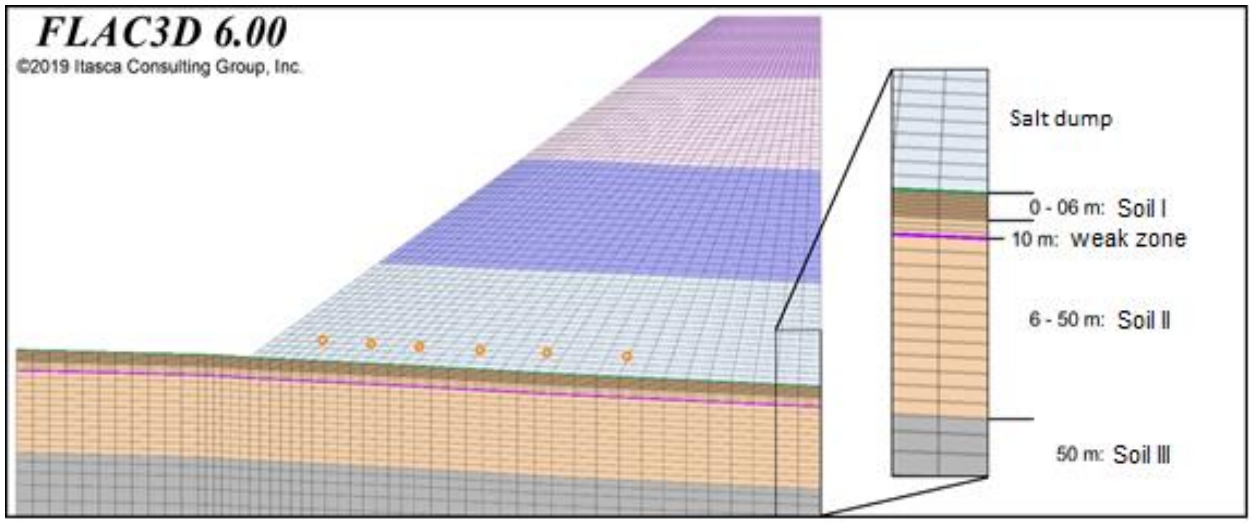

Figure 5.7: Salt dump geometry with monitoring points inside

In addition, a weak zone at a depth of 10 m was taken into account in the model using interface elements. Mohr-Coulomb behavior was assumed for the subsoil. Tab. 5.7 shows the parameters of the subsoil and Tab. 5.8 shows the properties of the geomembrane and subsoil interface. Note that the geomembrane in this model is represented in a simplified manner by interface elements only. The values for the contact stiffnesses (interfaces, geomembrane) depend on the mesh size according to the following formula:

$$k_n = (1 \ldots 2.5) \cdot k_s \geq 10 \cdot \frac{\left(K + \frac{4}{3}G\right)}{\Delta z_{min}} \tag{58}$$

where k_n and k_s are the interface stiffnesses in the normal and shear directions, respectively, and Δz_{min} is the minimum zone edge length perpendicular to the considered interface.

Table 5.7: Soil and rock mechanical parameters for the subsoil layers

Parameters	Soil I	Soil II	Soil III
Density (ρ), kg/m³	1950	1950	2100
Friction angle (ϕ), °	22.5	28.0	35.0
Cohesion (c), Pa	10^4	$3 \cdot 10^4$	10^5
Elastic modulus (E), Pa	$2 \cdot 10^7$	$2 \cdot 10^8$	$5 \cdot 10^8$
Poisson's ratio (ν)	0.3	0.3	0.3
Bulk modulus (K), Pa	$1.67 \cdot 10^8$	$1.67 \cdot 10^8$	$4.17 \cdot 10^8$
Shear modulus (G), Pa	$7.7 \cdot 10^7$	$7.7 \cdot 10^7$	$1.92 \cdot 10^8$

Table 5.8: Interface parameters

Properties	Geomembrane (interface elements)	Zone of weakness at 10 m depth
Normal stiffness (k_n), Pa/m	$3.6 \cdot 10^{11}$	$5.2 \cdot 10^{10}$
Shear stiffness (k_s), Pa/m	$2.8 \cdot 10^{11}$	$2.6 \cdot 10^{10}$
Friction angle (ϕ), °	30	22.5

Simulation Results

The simulations aim to depict a realistic behavior typically observed in-situ. Essentially, the settlement and deformation behavior of the salt dump (compaction and creep) and the deformations in the subsoil are considered. The results show that the proposed constitutive model:

- Provides realistic results comparable to other studies and field observations (Fischer et al., 2022),
- Can be used for simulations of long time periods with large deformations
- Can be used to predict waste dump deformations and the interaction with the subsoil
- Can be used for planning salt dump extensions

The results of the numerical simulations can be summarized as follows:

- The interior of the salt dump is completely compacted,
- Over time, settlements of over 30 m occur at the top edge of the salt dump,
- Stationary creep occurs at the foot of the salt dump with a creep rate of around 4 cm/a.
- Directly below the waste dump, subsoil material is being moved due to the link with the creeping salt dump,
- In the subsoil, shear displacements occur in the zone of weakness (interface) at a depth of 10 m,
- In the subsoil, the settlement reaches about 2 m below the core of the salt dump,

- A stationary overall state is reached after several years in which viscous creep of the salt dump dominates,
- No waste dump instabilities are observed.

These simulation results show good agreement with in-situ observations and measurement results (Fischer et al., 2022). Fig. 5.8 shows the evolution of the salt dump contour with increasing time. The rapid reduction in volume due to the compaction at the beginning can be clearly seen. In the further course, the volume changes only slightly; instead, the creep phase dominates, which is reflected in a change in the shape of the contour line.

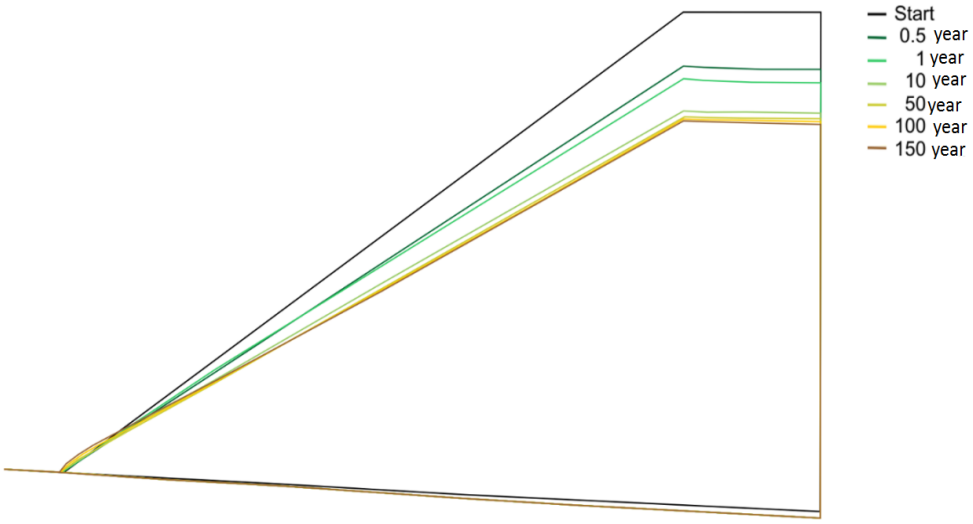

Figure 5.8: Evolution of the salt dump contour over time

In the upper salt dump area, the subsidence is over 30 m (see Fig. 5.9), which is also observed in-situ (Fischer et al. 2022). Under the full salt dump load, the settlement of the subsoil reaches more than 2 m (Fig. 5.10). This value corresponds to the chosen soil properties. Fig. 5.11 shows the development of the creep rates in a salt dump for the monitoring points. One can clearly see the downward trend towards a stationary displacement rate of about 4 cm/a at the front area of the salt dump.

Fig. 5.12 illustrates the compaction as a function of time. In the core of the salt dump, compaction is progressing very quickly, and after 5 years, the compaction is nearly completed with exception of the outer (near-surface) areas.

The stress distributions are shown in Fig. 5.13 to 5.15. The vertical stresses (Fig. 5.14) follow, as expected, the weight of the overlying rock mass.

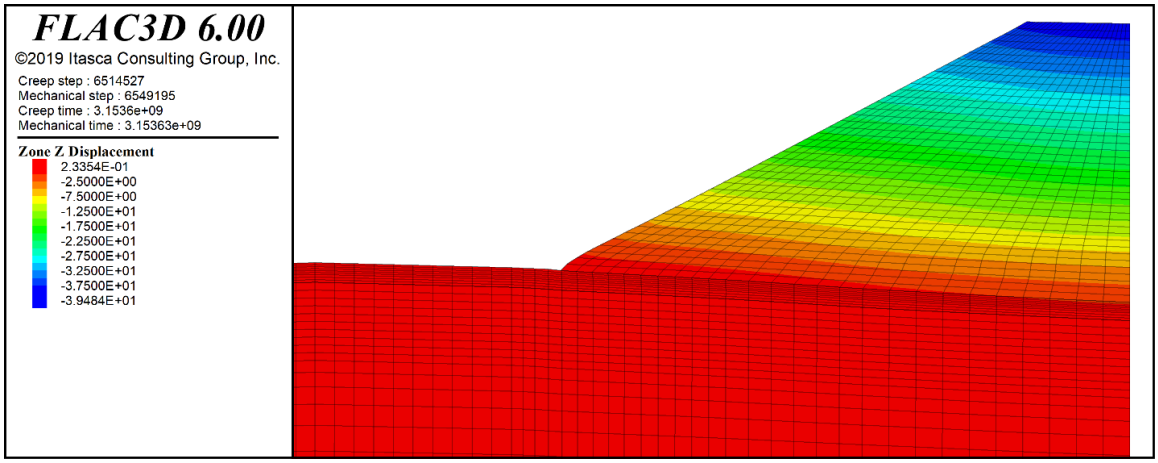

Figure 5.9: Vertical displacements (m) after 100 years

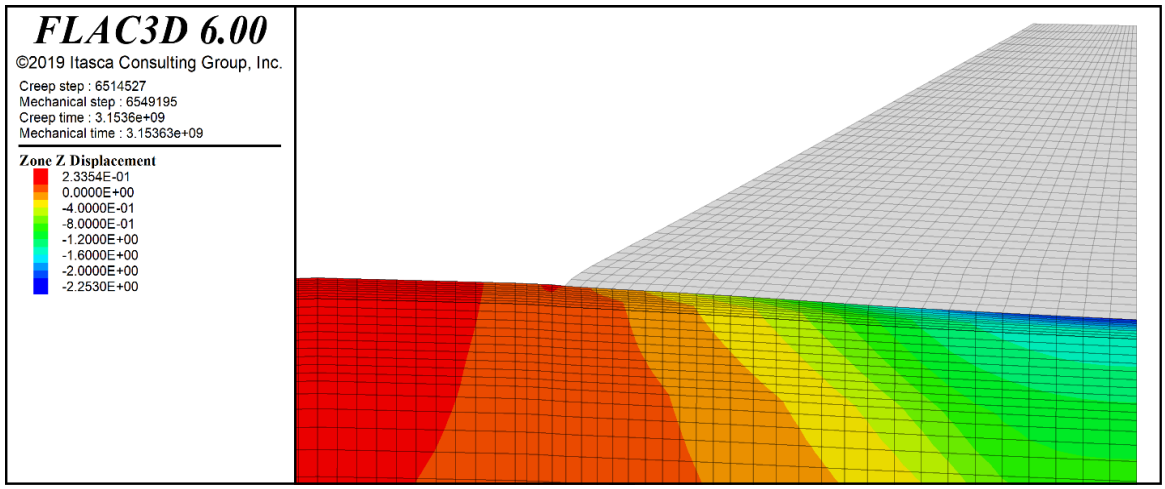

Figure 5.10: Vertical displacements (m) in the footwall after 100 years

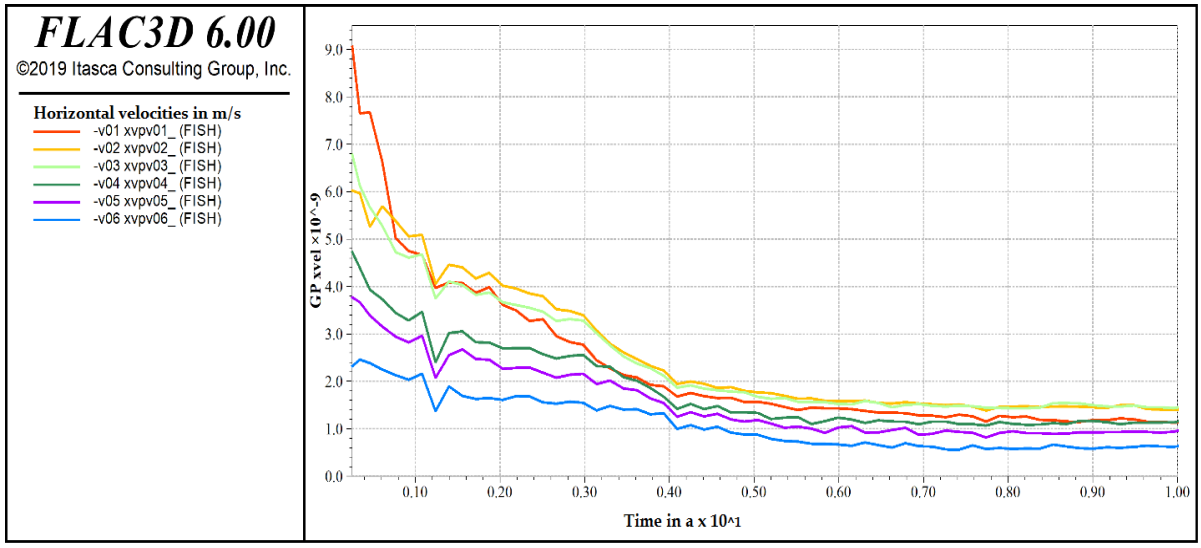

Figure 5.11: Horizontal velocities (m/s) versus time along a horizontal monitoring line in the waste dump ($1e^{-9}$ m/s = 3.15 cm/a)

a)

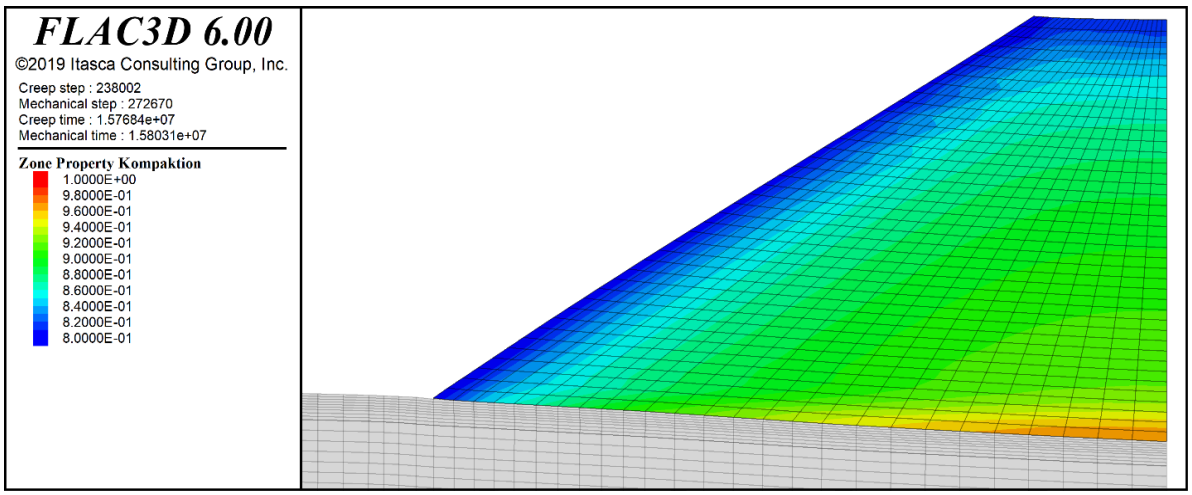

b)

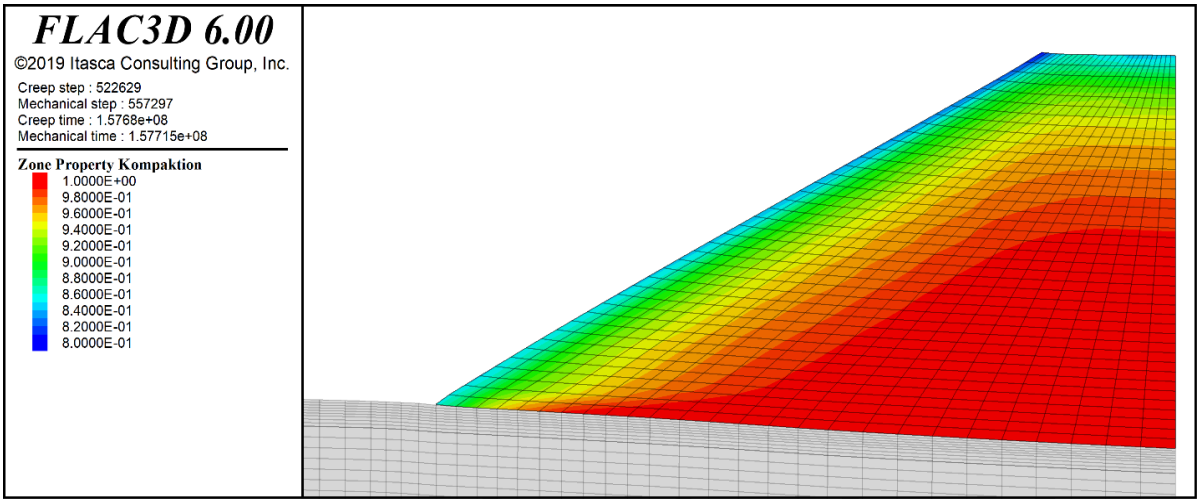

c)

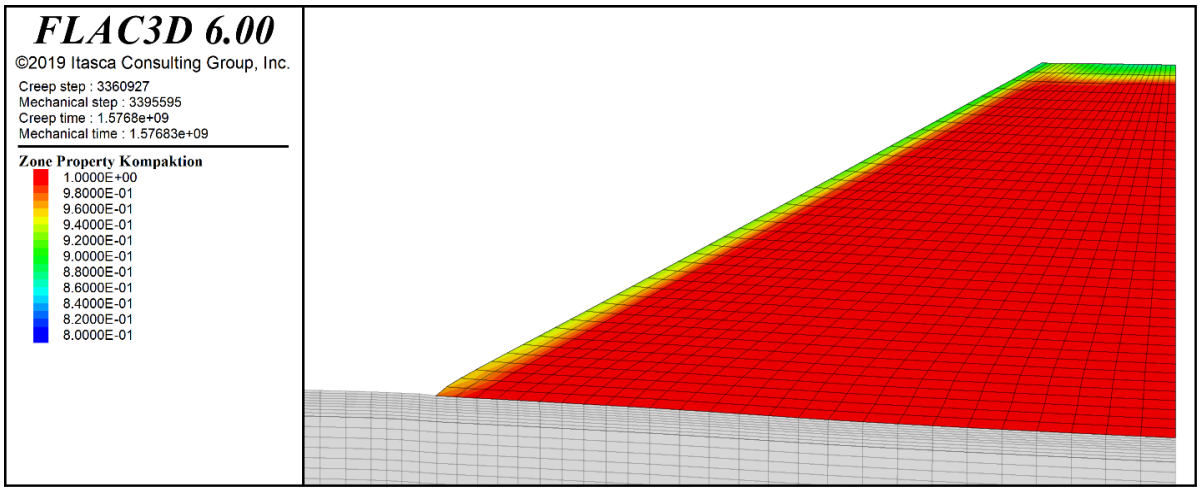

Figure 5.12: Degree of compaction of salt dump

a) 6 months after the salt dump *was created*

b) 5 years after the salt dump *was created*

c) 100 years after the salt dump *was created*

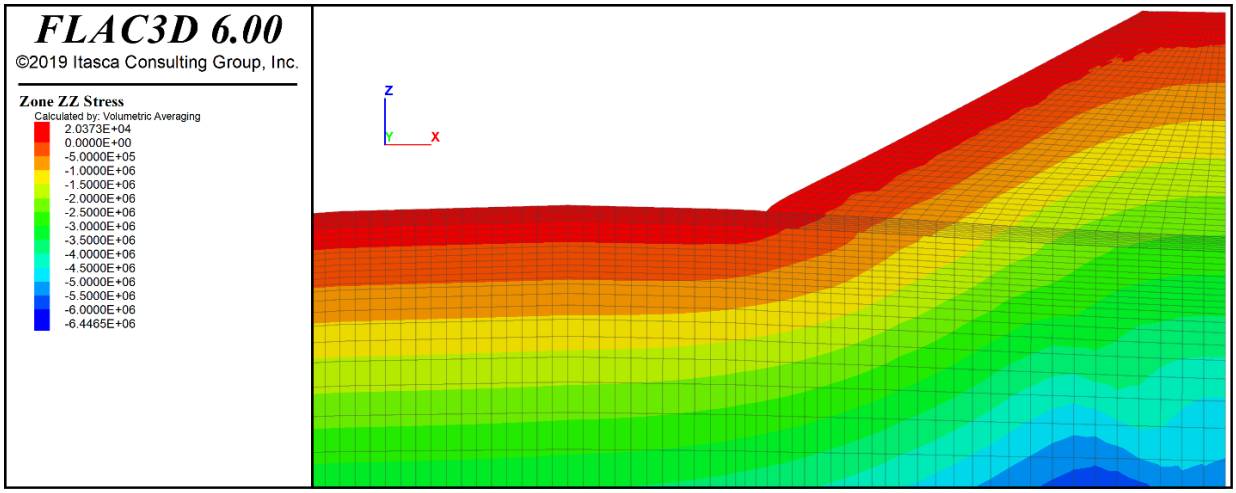

Figure 5.13: Vertical stresses (Pa) after 100 years

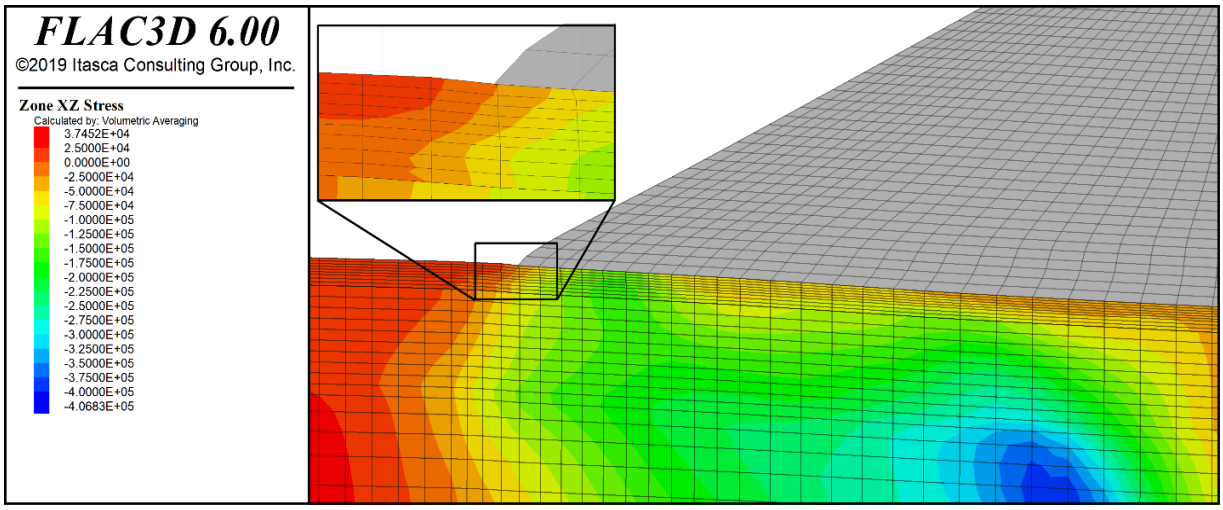

Figure 5.14: Maximum shear stresses (Pa) in subsoil after 100 years

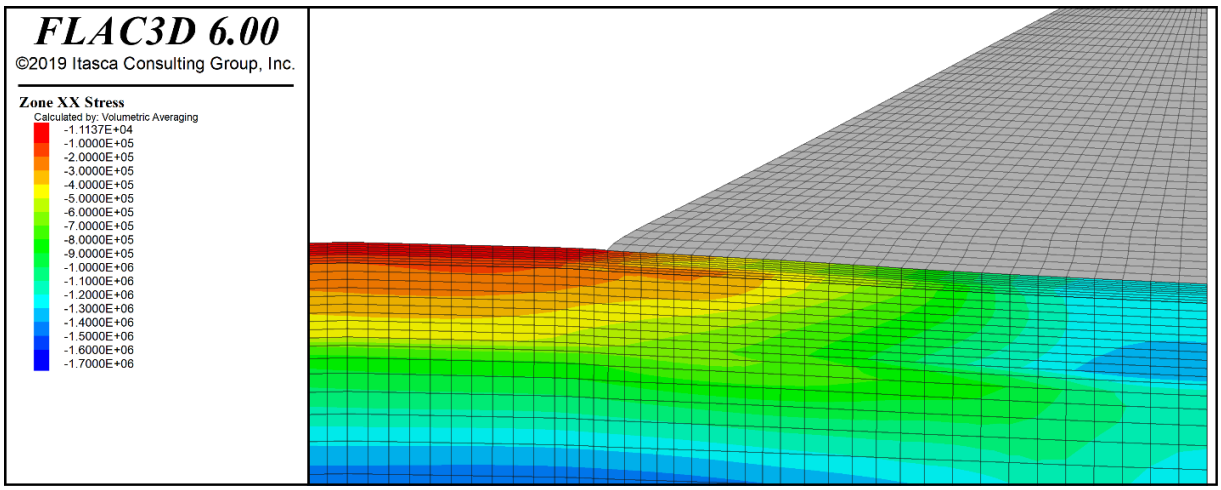

Figure 5.15: Horizontal stresses (Pa) in subsoil after 100 years

5.3 Summary

The verified and partially validated constitutive law 'FemeSalz' is available in FLAC^{3D} to simulate salt waste dumps, but also crushed salt behavior in general.

Based on the obtained results so far, a real-time simulation of the stockpiling process in every detail is not necessary for long-term considerations. The duplication of these processes in some stages may be sufficient.

Further application to more complex 3D geometries is possible and has been successfully tested (see chapter 6). Particular attention should be paid to the 3D meshing of the model.

The use of interface (simplified version) or much better the use of the ‘liner’ model (sophisticated version) makes it possible in FLAC^{3D} to include a geomembrane and to investigate the interaction between geomembrane and salt dump on one side and subsoil on the other side including the stress-strain and damage behavior of the geomembrane itself.

CHAPTER 6: SIMULATIONS CONSIDERING TOPOGRAPHY OF UNDERLYING MATERIAL

6.1 Introduction

So far, all the above-described simulations have considered only a flat horizontal underlying material (subsoil). The aim of this study is to investigate the loading on a geomembrane produced by piling up a dump on uneven ground. Exemplary, again, a salt dump is used due to the pronounced creep behavior, which produces strong displacements and strains, respectively. In particular, the loading on a geomembrane considering the 3D situation - which depicts real in-situ conditions – is compared with 2D calculations. Three different topographies were considered for the underlying material: flat horizontal ground, ground with a valley, and ground with a ridge (hill) structure. They are compared with each other and with 2D calculations.

6.2 Model set-up

The following three 3D models were set up:

- Model of a dump in a valley (model "3D-valley")
- Model of a dump over a mountain ridge (model "3D-mountain")
- Model of a dump on a horizontal plane ground (“3D-plain” model)

2D models:

- Model of a dump in a valley (model "2D-valley")
- Model of a dump over a mountain ridge (model "2D-mountain")
- Model of a dump on a horizontal plain ground (“2D-plain” model)

The 2D models run along the valley axis or over the ridge and thus duplicate the most pronounced topography. Fig. 6.1 and 6.2 show the geometrical model structure of the topographically exposed models (valley and mountain). The model with a plain base under the dump is analogous.

In the vertical direction, the models consist of the following layers (from top to bottom):

- Dump body
- Upper interface

- Geomembrane
- Lower interface
- Ground (contact area of the dump with 3 layers)

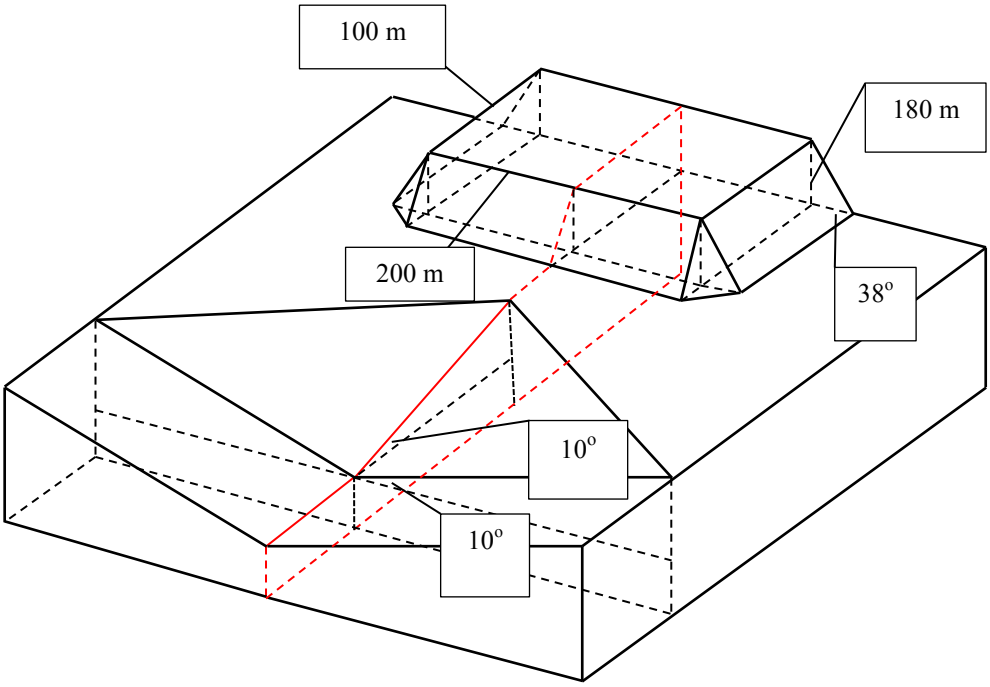

Figure 6.1: "valley" model: salt dump over valley structure (not true to scale), in red: corresponding 2D model

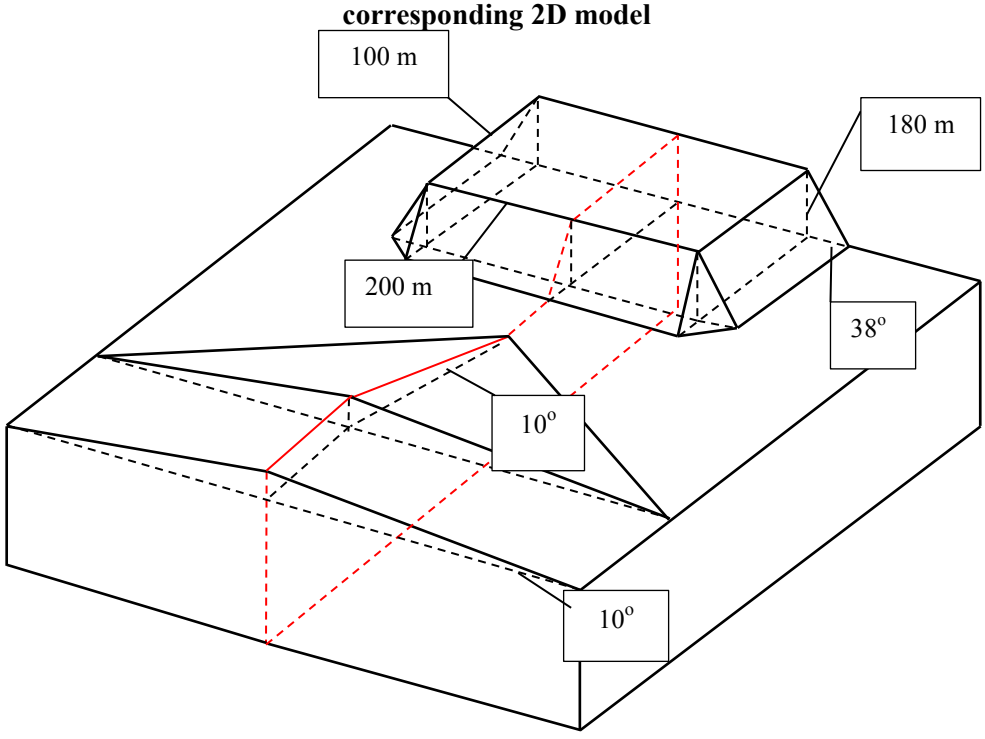

Figure 6.2: "mountain" model: salt dump over mountain structure (not true to scale), in red: corresponding 2D model

Fig. 6.3, 6.4, and 6.5 show the meshes of the 3 models. In each model, the stockpiling starts on a horizontal plane. Then the dumping either continues plain or into a valley or across a ridge. Fig. 6.6 and 6.7 show an example of the layer structure of the models for the case "3D-mountain". Due to the assumed symmetry of the valley and mountain ridge structure, only ½-models are calculated in each case (the axis of symmetry is the valley or ridge axis). This reduced the computing time for the creep process significantly.

The 3D numerical models consist of 20,386 zones and 25,450 nodes as well as 2,500 elements for the geomembrane. The equivalent 2D models have a thickness of only one element. The geometry follows the plane of symmetry in the 3D models (drawn as red lines in Fig. 6.1 and 6.2).

Fig. 6.8 and 6.9 show the corresponding 2D and 3D models. Fig. 6.10 shows the models "3D-mountain" and "3D-valley" viewed from the backside (view of the axis of symmetry).

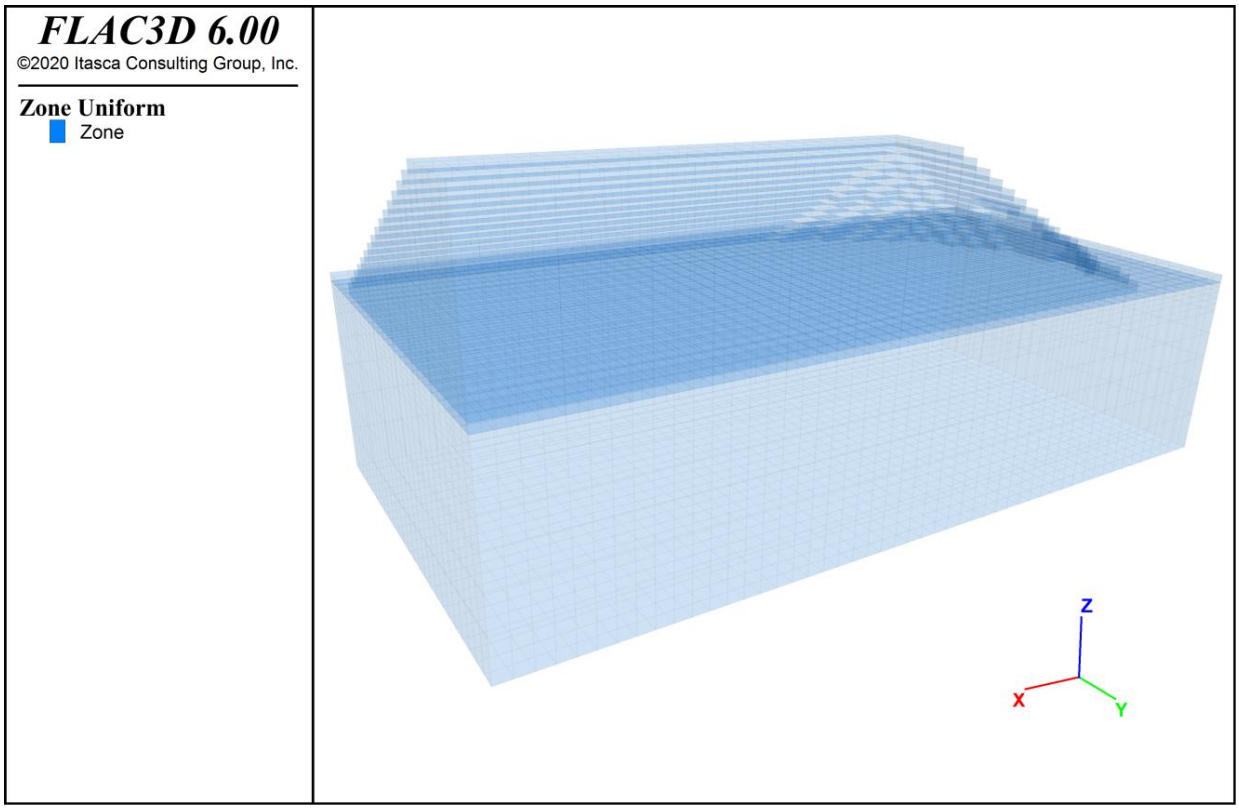

Figure 6.3: Mesh of "3D-plain" model with fully developed salt dump

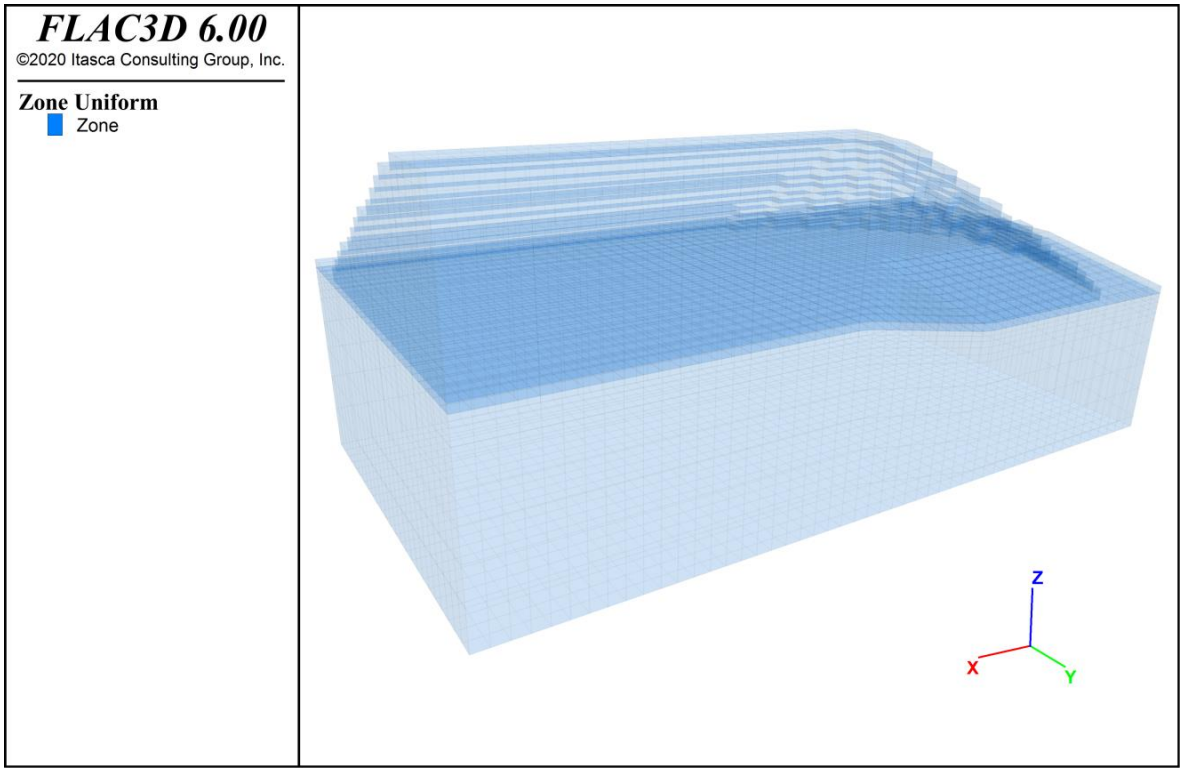

Figure 6.4: Mesh of "3D-valley" model with fully developed salt dump

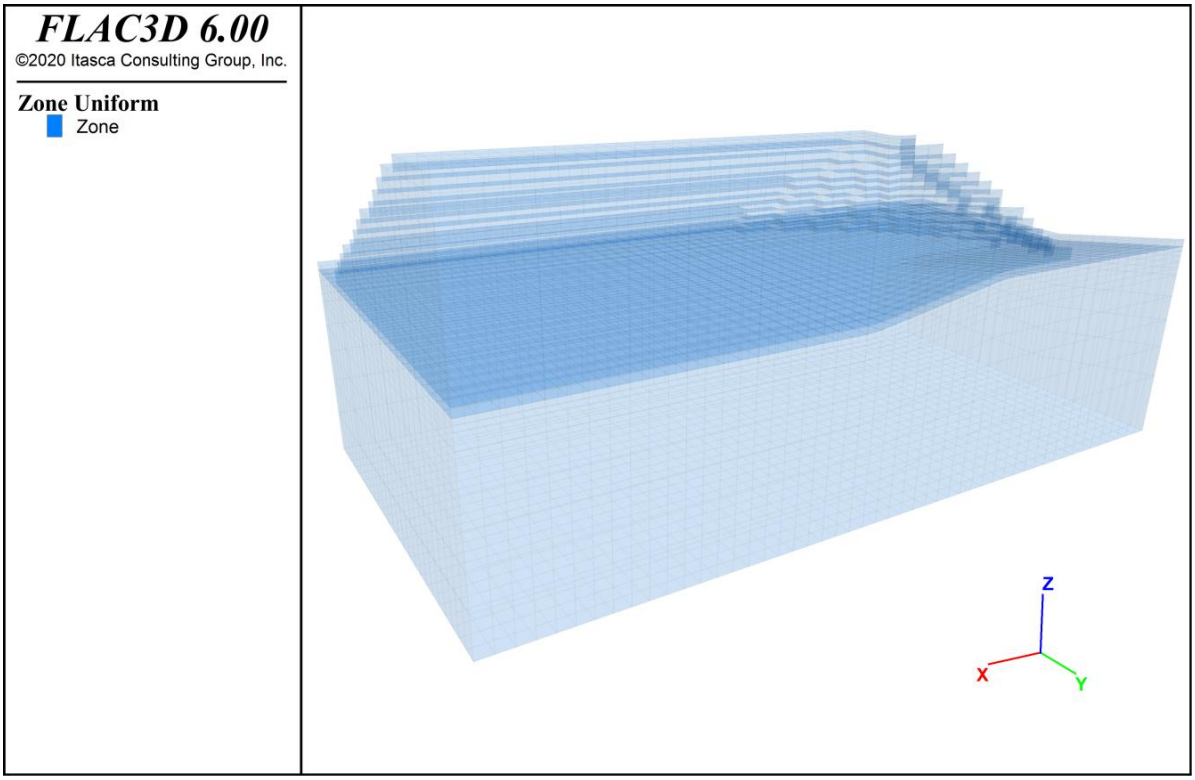

Figure 6.5: Mesh of "3D-mountain" model with fully developed salt dump

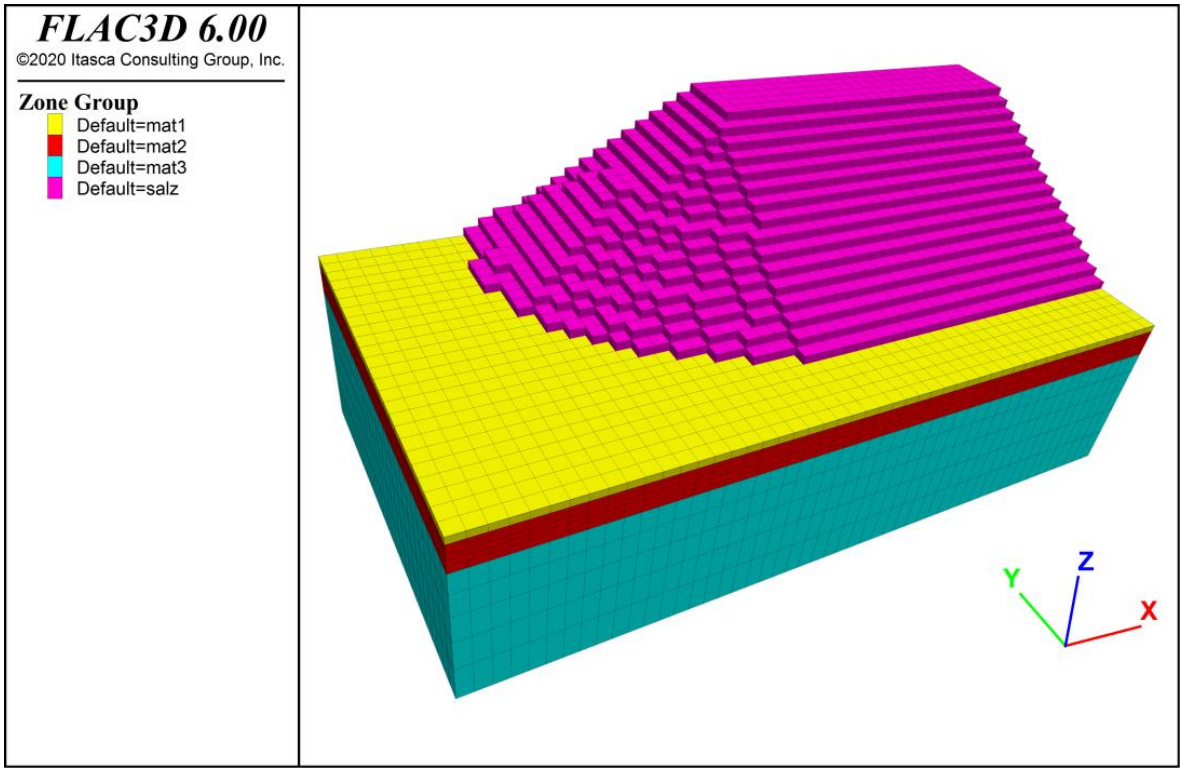

Figure 6.6: Model "3D-plain" with colored layers (mat1, mat2, mat3) and the salt dump body (salz) in the final state

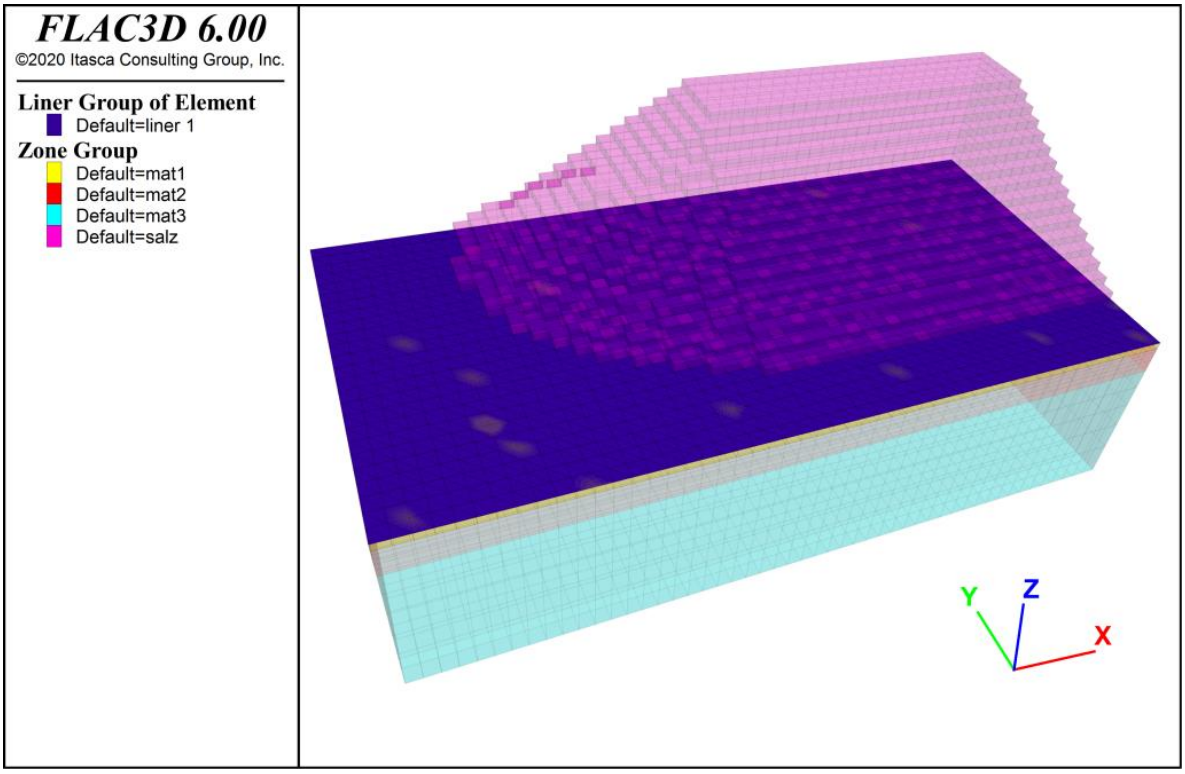

Figure 6.7: Model "3D-plain", transparent, colored layers (mat1, mat2, mat3) and the salt dump (salz), non-transparent green: geomembrane (liner 1), final state

a)

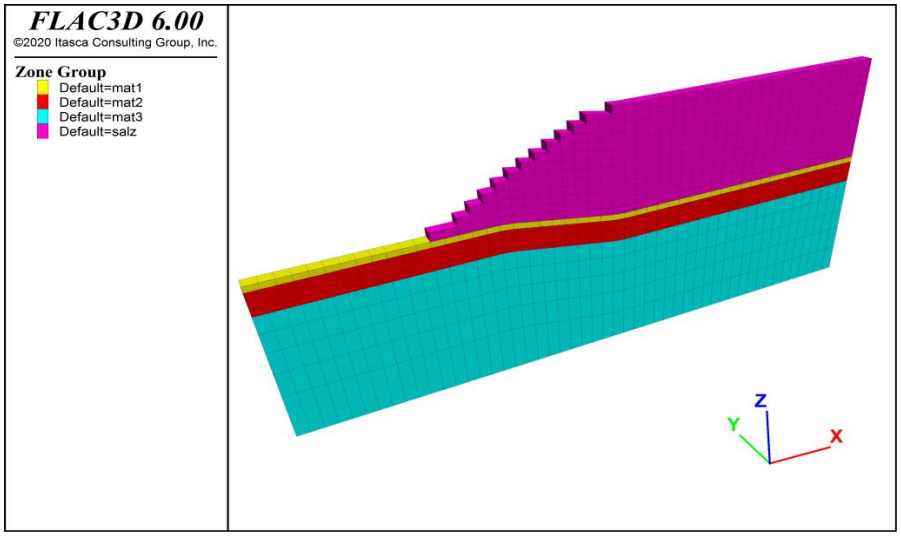

b)

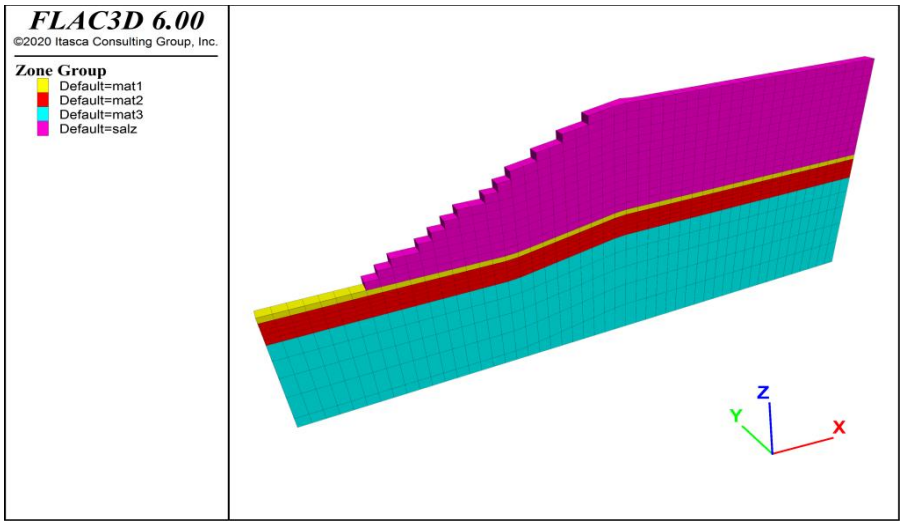

c)

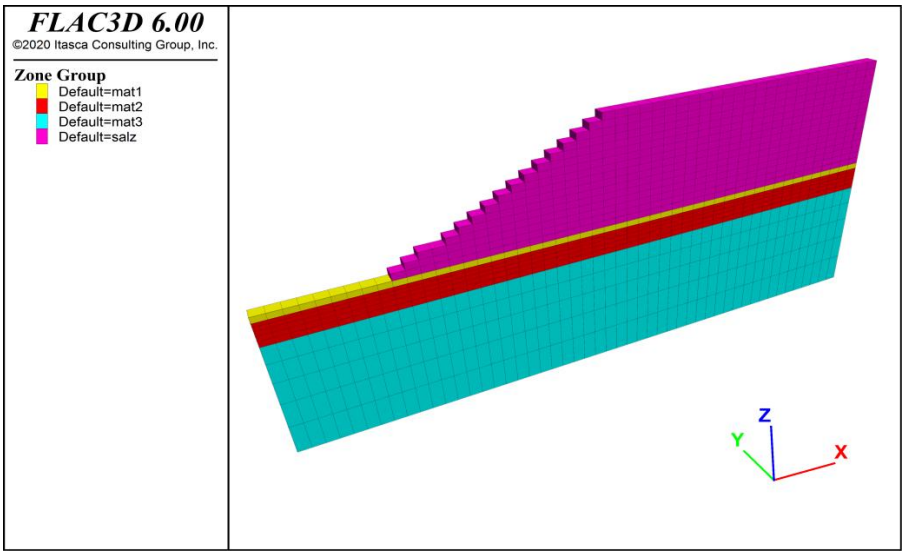

Figure 6.8: Layer structure of 2D models with 3 types of topography
a) mountain shape b) valley shape c) plain shape

a)

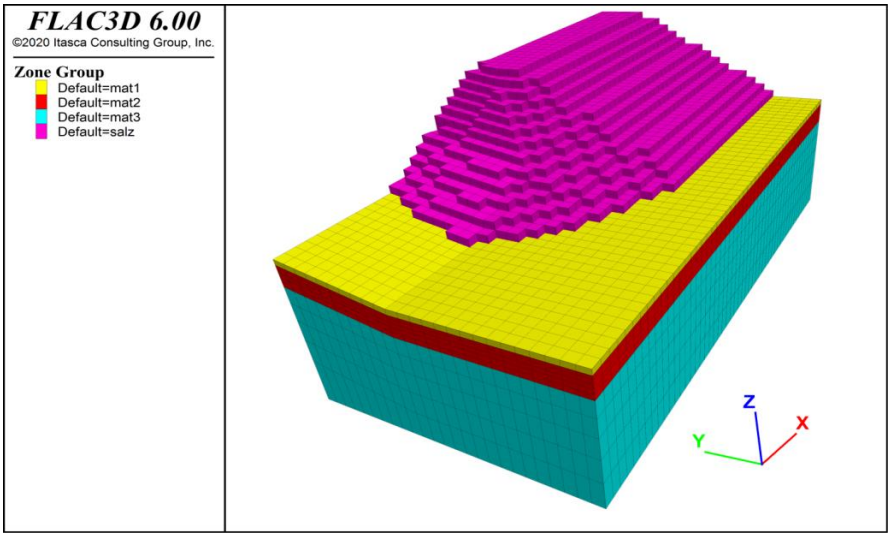

b)

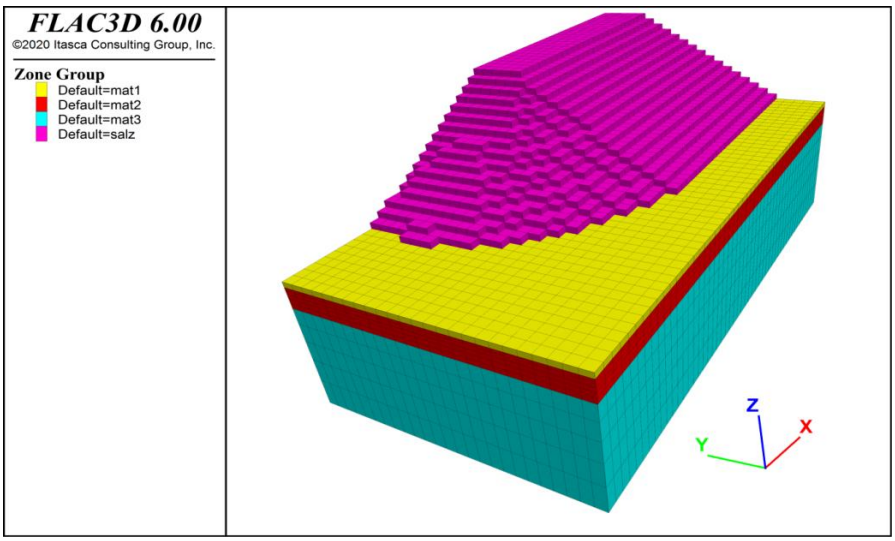

c)

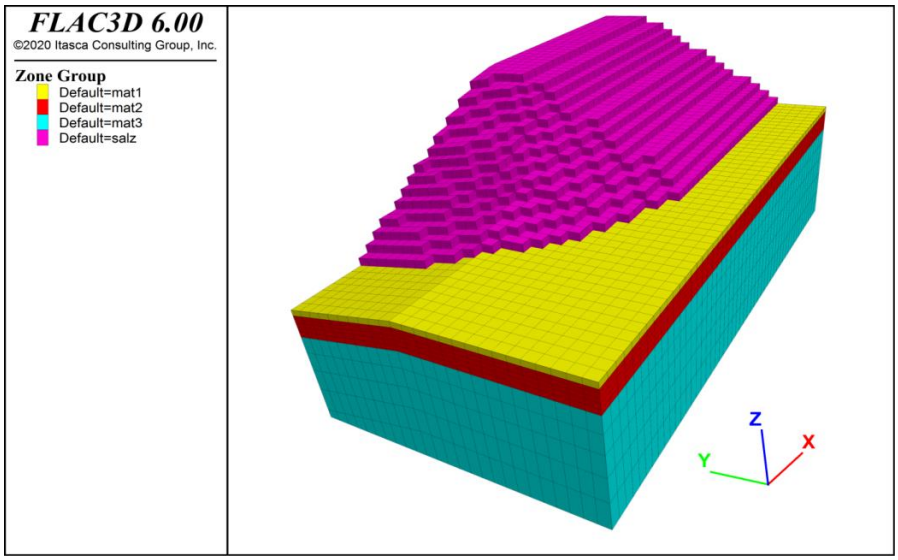

Figure 6.9: Layer structure of 3D models with 3 types of topography
a) mountain shape b) valley shape c) plain shape

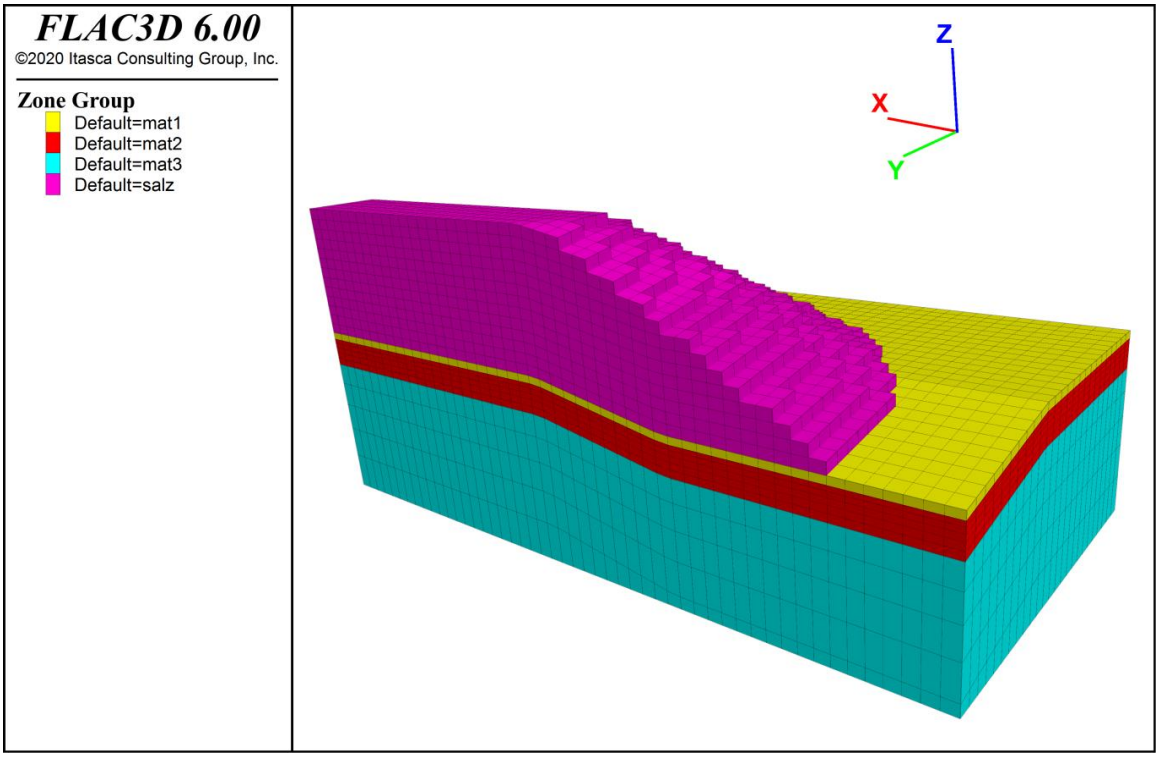

a)

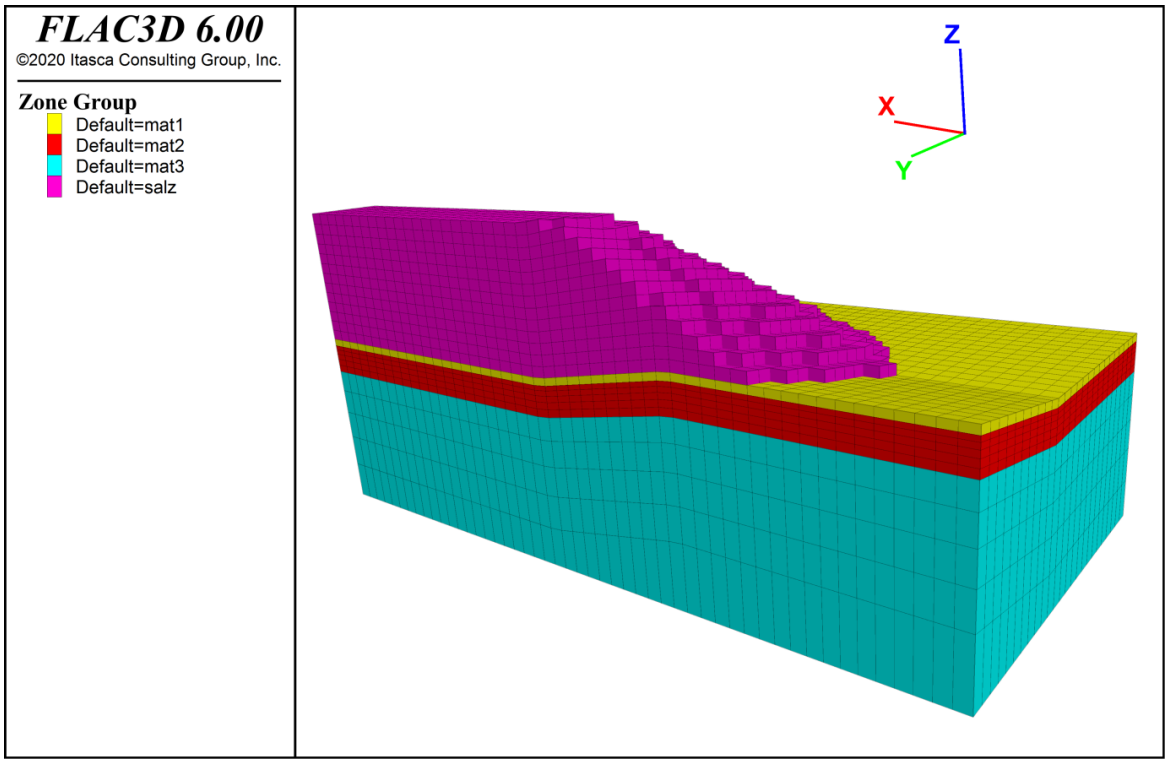

b)

Figure 6.10: Comparison of layer structure of 3D models viewed from the backside (plane of symmetry)

a) Valley shape b) Mountain shape

6.3 Model parameters and calculation sequence

The constitutive laws and parameters used for the simulations are based on a parameter study documented in chapters 2 to 5. In the present calculations, no use was made of the possibility of simulating the tearing of the geomembrane to enable a complete 2D versus 3D comparison, i.e., the geomembrane reacts purely elastic (geomembrane failure is avoided).

The salt dump is applied in one calculation step and then calculated for 100 years using the 'Femesalz' constitutive model in full interaction with the geomembrane (simulated via the 'liner' model) and the subsoil. The friction angles on both sides of the geomembrane are very important for the behavior. The following applies to the simulations presented here:

Table 6.1: Properties of the ground

Parameters	**mat1**	**mat2**	**mat3**
Density ρ, kg/m³	1.95	1.95	2.1
Friction angle ϕ, °	22.5	28.0	35.0
Cohesion c, kPa	10	30	100
Young's modulus E, MPa	20	200	500
Poisson's ratio	0.3	0.3	0.3
Bulk modulus K, MPa	16.7	167	417
Shear modulus G, MPa	7.7	77	192

Table 6.2: Properties of interfaces between geomembrane/dump and geomembrane/ground

Parameter		**Value**
Normal stiffness k_n, Pa/m (both sides)		10^9
Shear stiffness k_s, Pa/m (both sides)		10^9
Friction angle ϕ, °	Side above	20
	Side below	30

- Friction angle between geomembrane and salt dump: 20°
- Friction angle between geomembrane and ground: 30°

The following parameters represent the geomembrane itself:

- Thickness: 3 mm
- Young's modulus: 3 GPa
- Poisson's ratio: 0.33

The calculations were carried out consistently with FLAC^{3D} (version 6.0).

6.4 Calculation results

All calculation results are related to a salt dump lifetime of 100 years, with the salt dump being built up instantaneously in one step, i.e., at time zero. The salt dump creeps according to the applied creep law (secondary creep phase). There are relative movements between the geomembrane and the salt dump and between the geomembrane and the ground. The geomembrane sometimes experiences considerable expansion or tensile stresses, and these are very local and partially also above acceptable values. The 2D simulations depict a plane deformation state, i.e., it is assumed that the salt dump is infinitely extended perpendicular to the image plane. 2D and 3D simulation results are shown in Tab. 6.3.

Table 6.3: Comparison of maximum horizontal displacements in the dump and maximum tensile stresses in geomembrane (2D versus 3D calculations)

Model	Maximum horizontal displacement, m	Maximum tensile stress in geomembrane, MPa
2D-plain	32	35
3D-plain	25	20
2D-valley	24	120
3D-valley	18	45
2D-mountain	4	33
3D-mountain	6	90

The 2D simulations allow the following statements:

- Compared to the plain variant, the valley terrain generates locally significantly higher strains and tensile stresses in the geomembrane.
- On the other hand, a mountain terrain produces less strain and slightly reduced tensile stress in the geomembrane.
- The horizontal displacements of the salt dump are significantly reduced when dumped uphill.

The 3D simulations show (see also Tab. 6.3):

- Compared to the plain variant, spill into a valley creates elevated elongations and tensile stresses in the geomembrane, but smaller horizontal displacements of the salt dump.
- A mountain terrain creates higher strains and thus increases tensile stresses in the geomembrane.

- The horizontal displacements of the salt dump are significantly reduced when dumped uphill.

In both cases (2D and 3D), the salt dump slides over a large area on the geomembrane and a slip occurs between the ground and the geomembrane.

a)

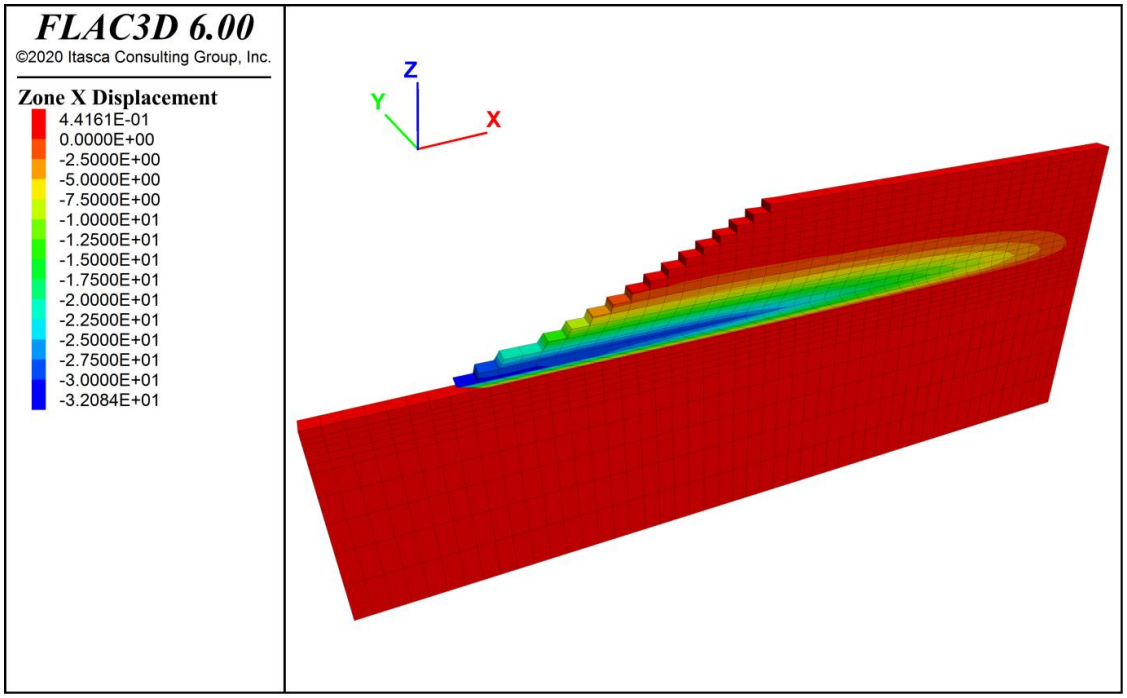

b)

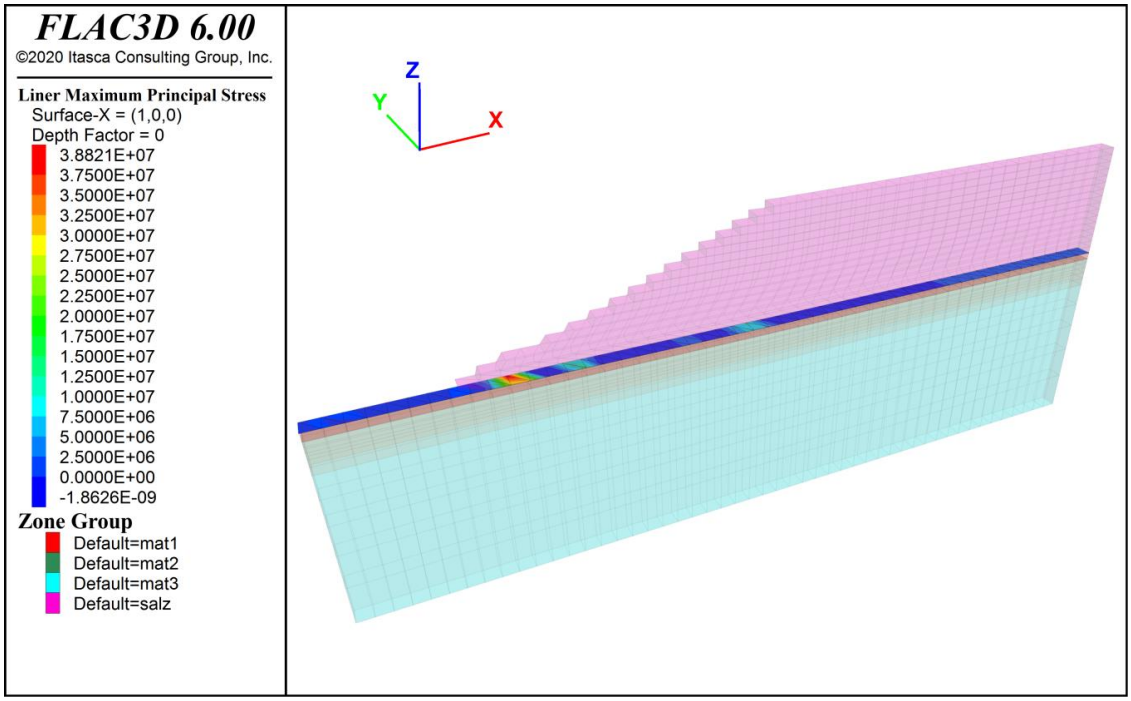

Figure 6.11: Model 2D-plain
a) Horizontal displacements in x-direction after 100 years,
b) Maximum principal stresses (Pa) in geomembrane

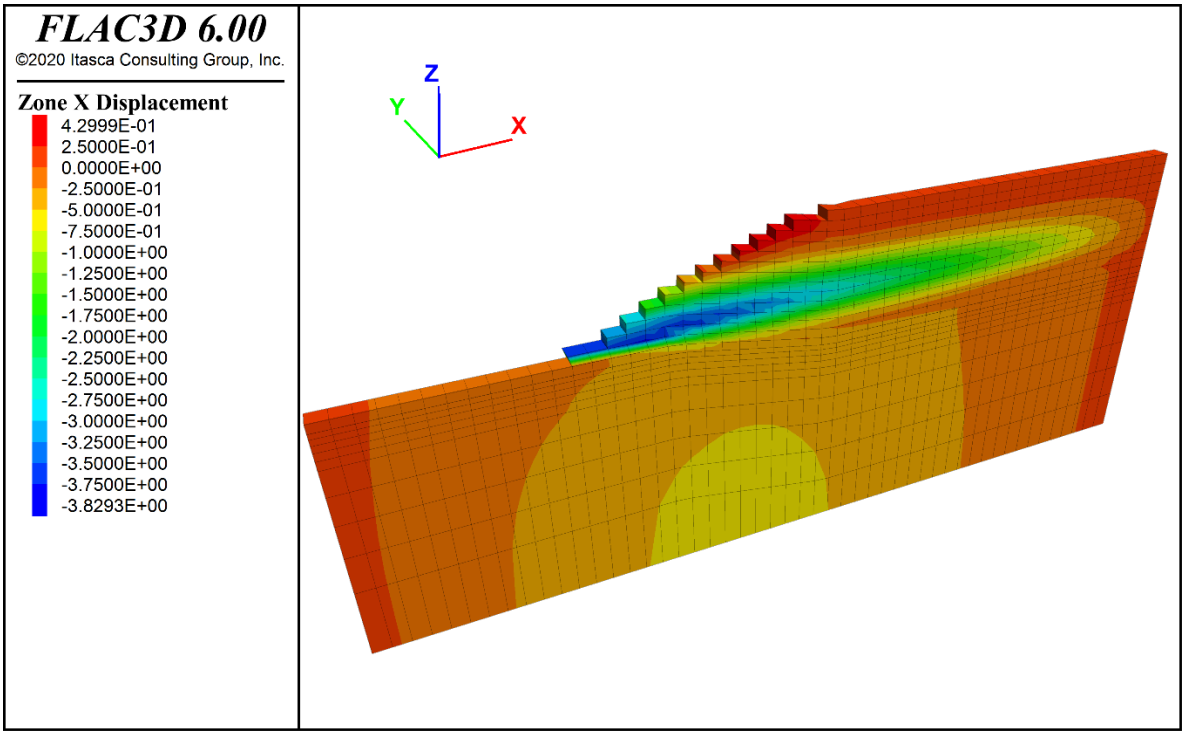

a)

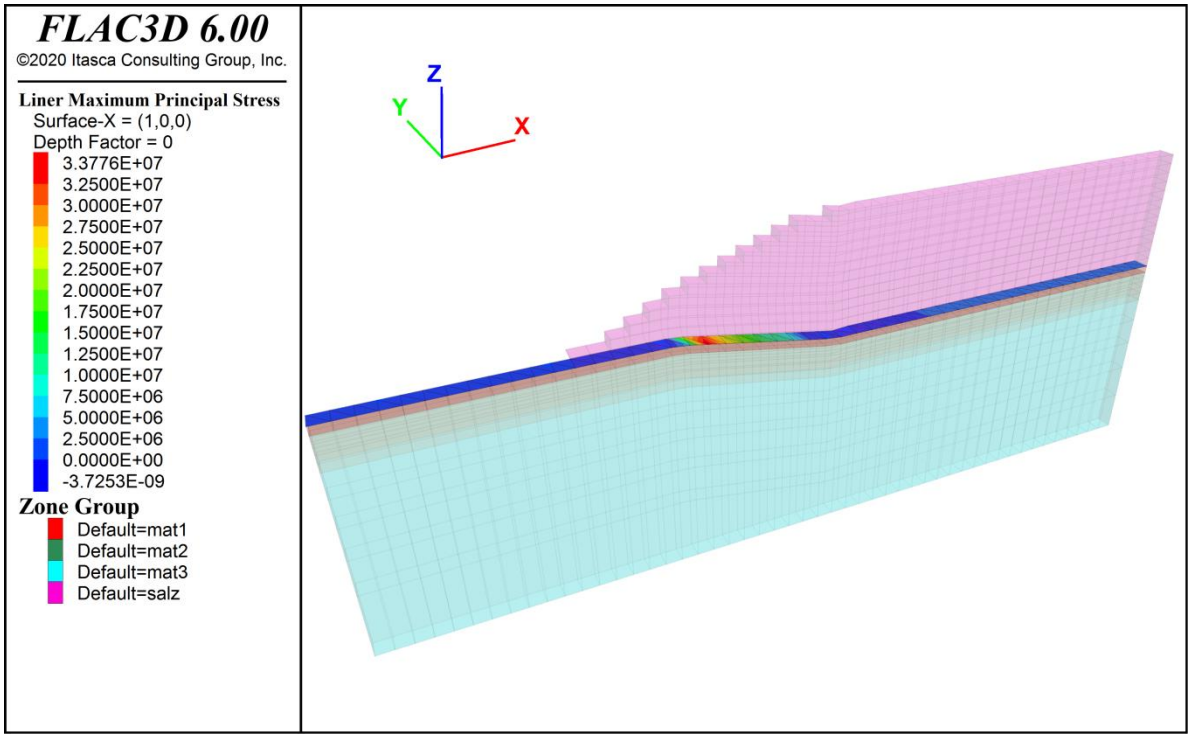

b)

Figure 6.12: Model 2D-mountain:
a) Horizontal displacements in x-direction after 100 years,
b) Maximum principal stresses (Pa) in geomembrane

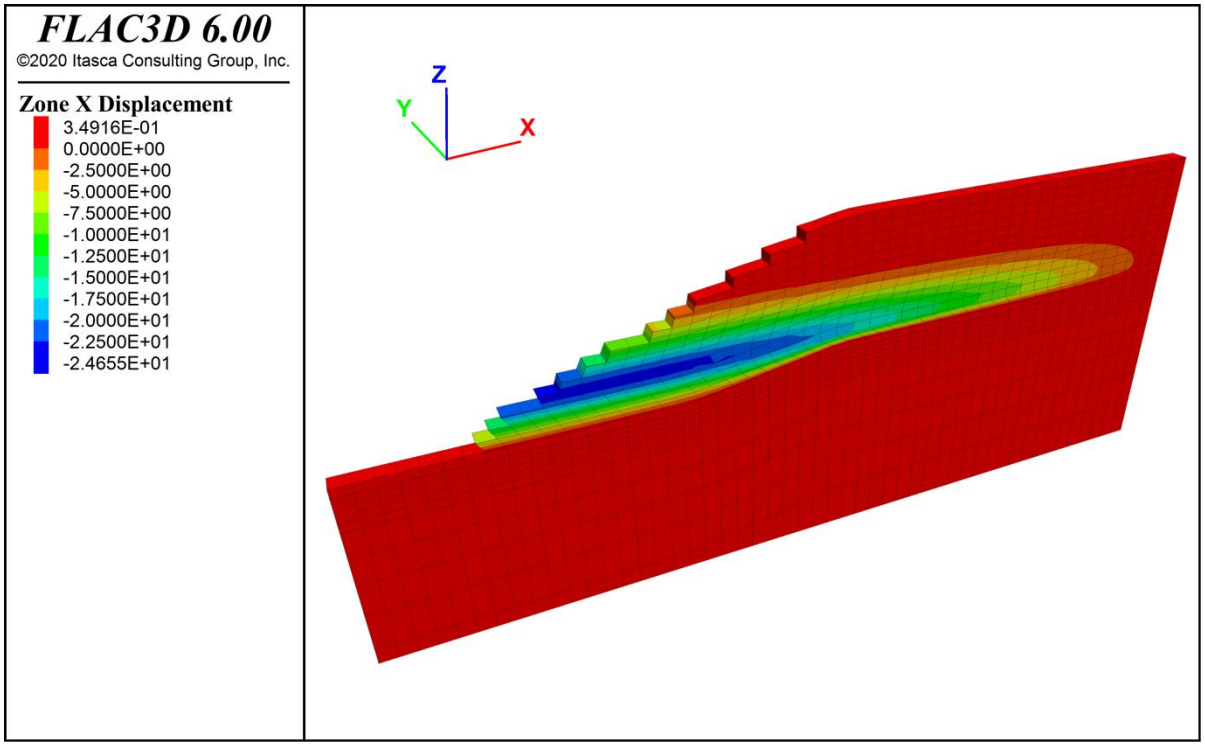

a)

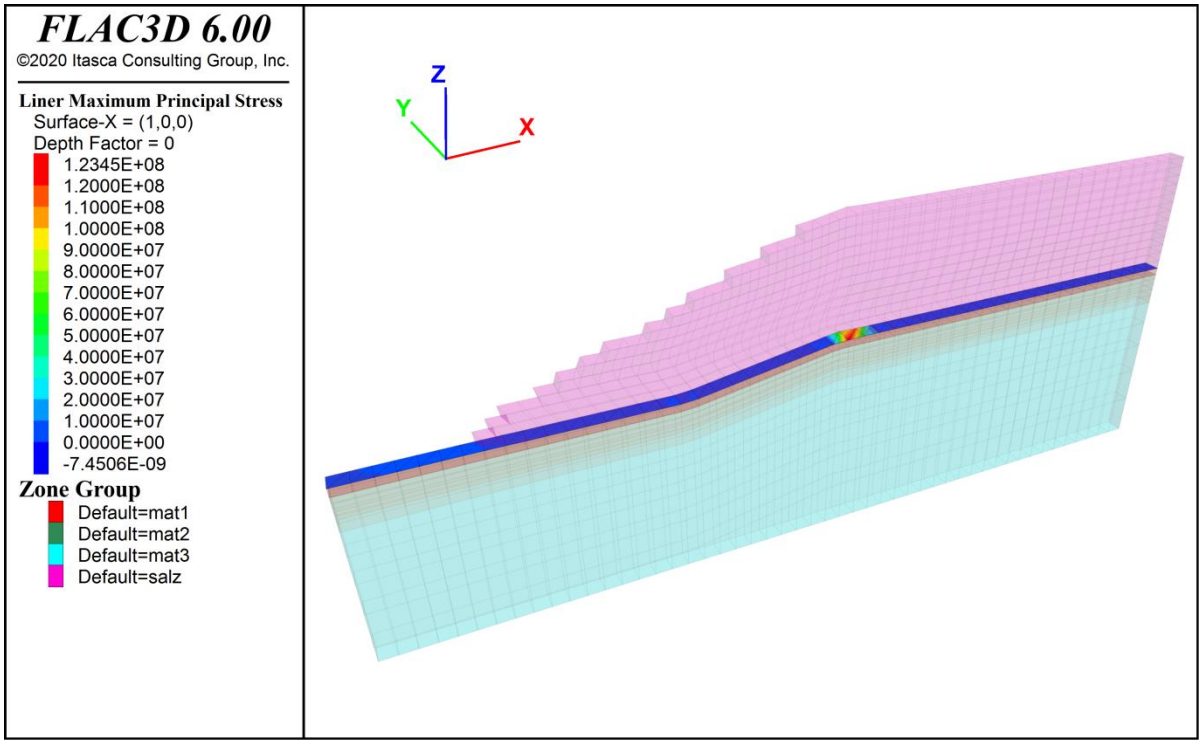

b)

Figure 6.13: Model 2D-valley:
a) Horizontal displacements in x-direction after 100 years,
b) Maximum principal stresses (Pa) in geomembrane

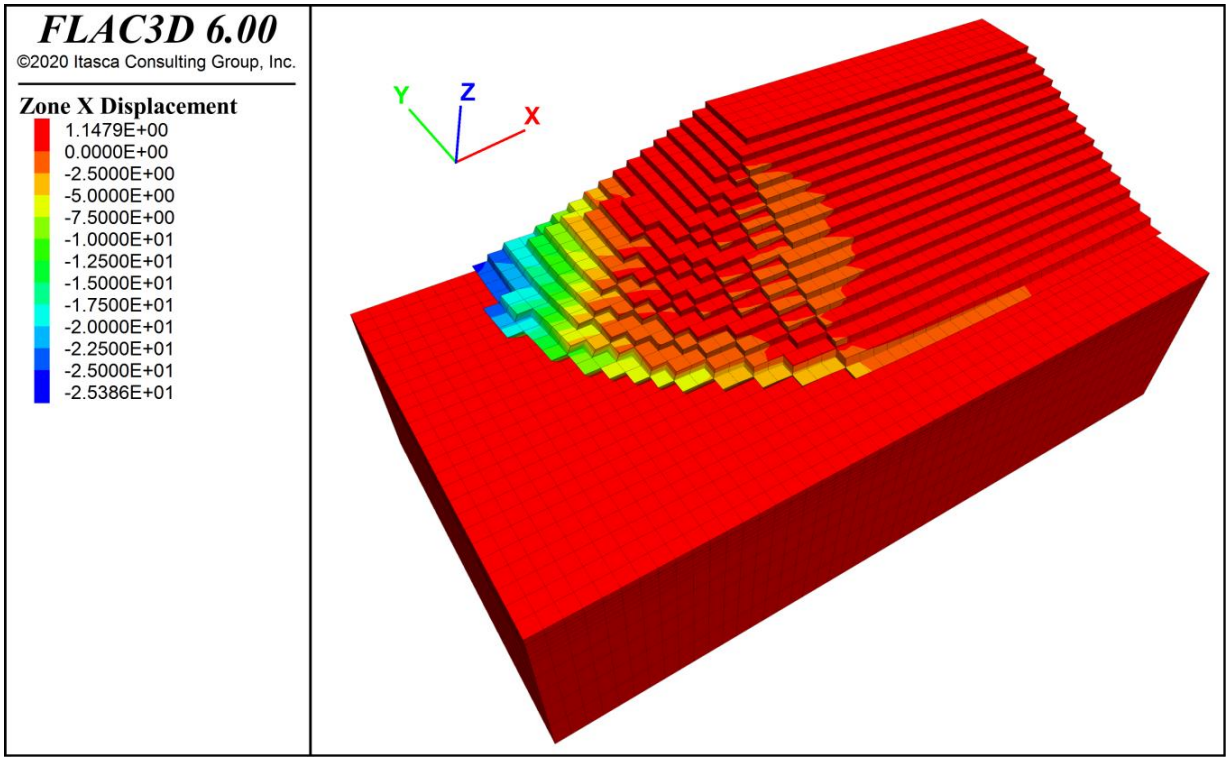

a)

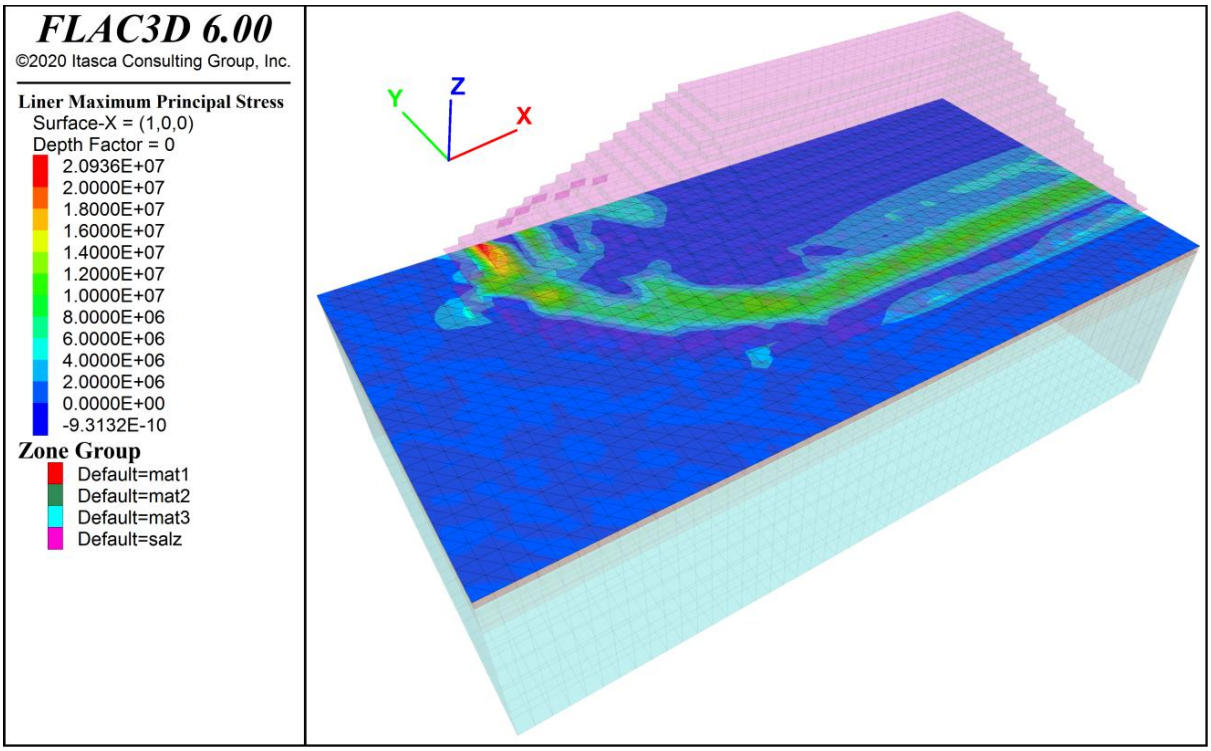

b)

Figure 6.14: Model 3D-plain:
a) Horizontal displacements in x-direction after 100 years,
b) Maximum principal stresses (Pa) in geomembrane

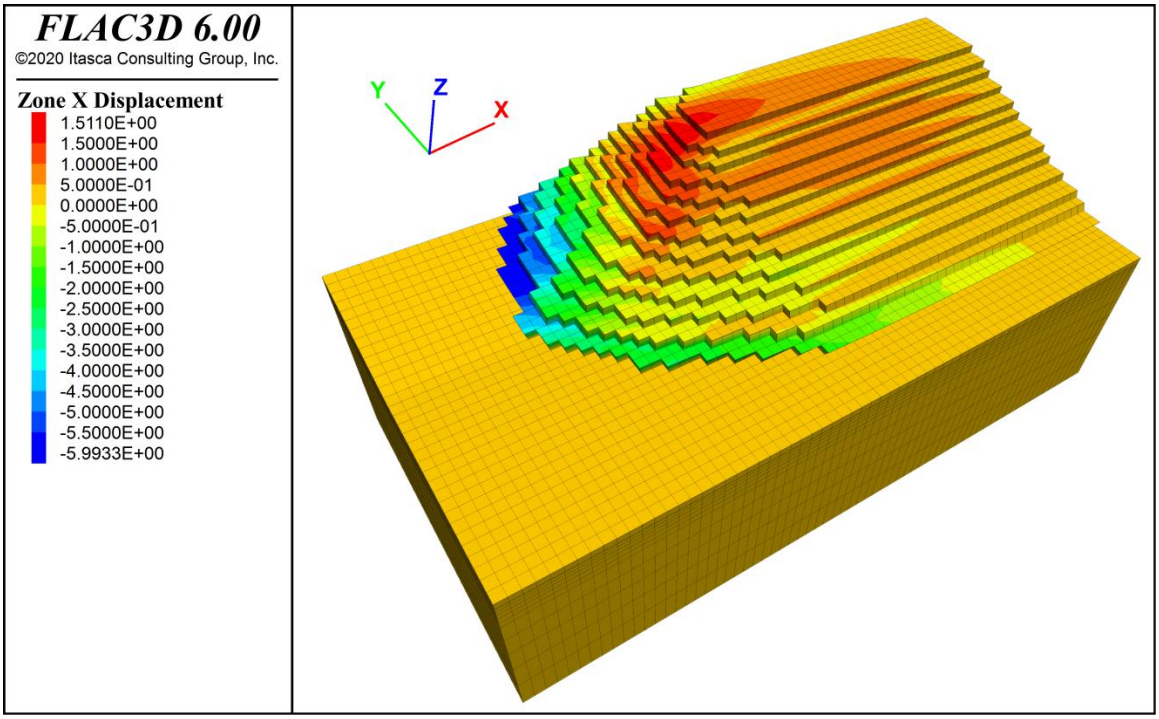

a)

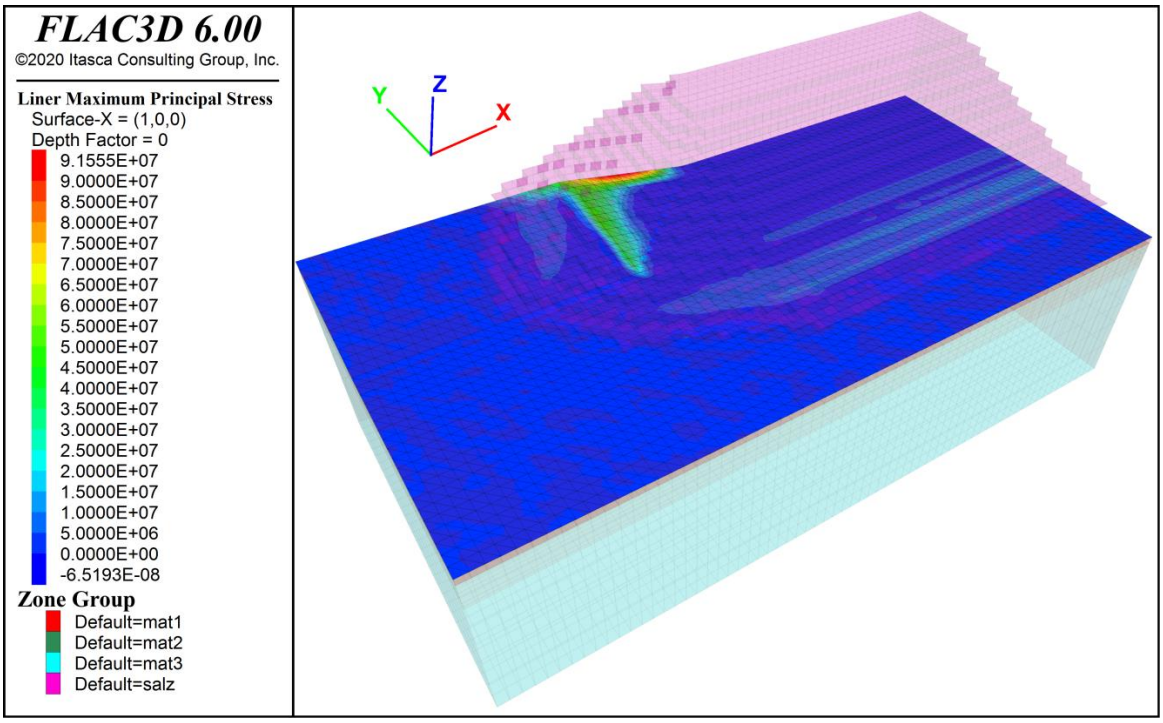

b)

Figure 6.15: Model 3D-mountain:
a) Horizontal displacements in x-direction after 100 years,
b) Maximum principal stresses (Pa) in geomembrane

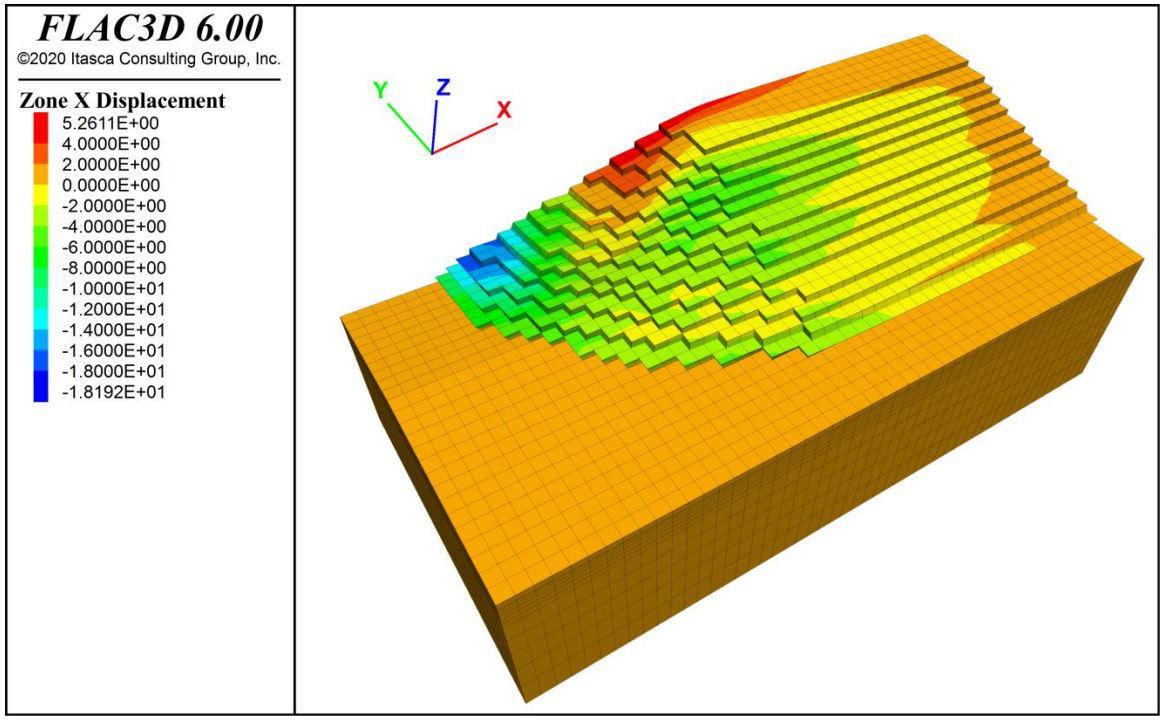

a)

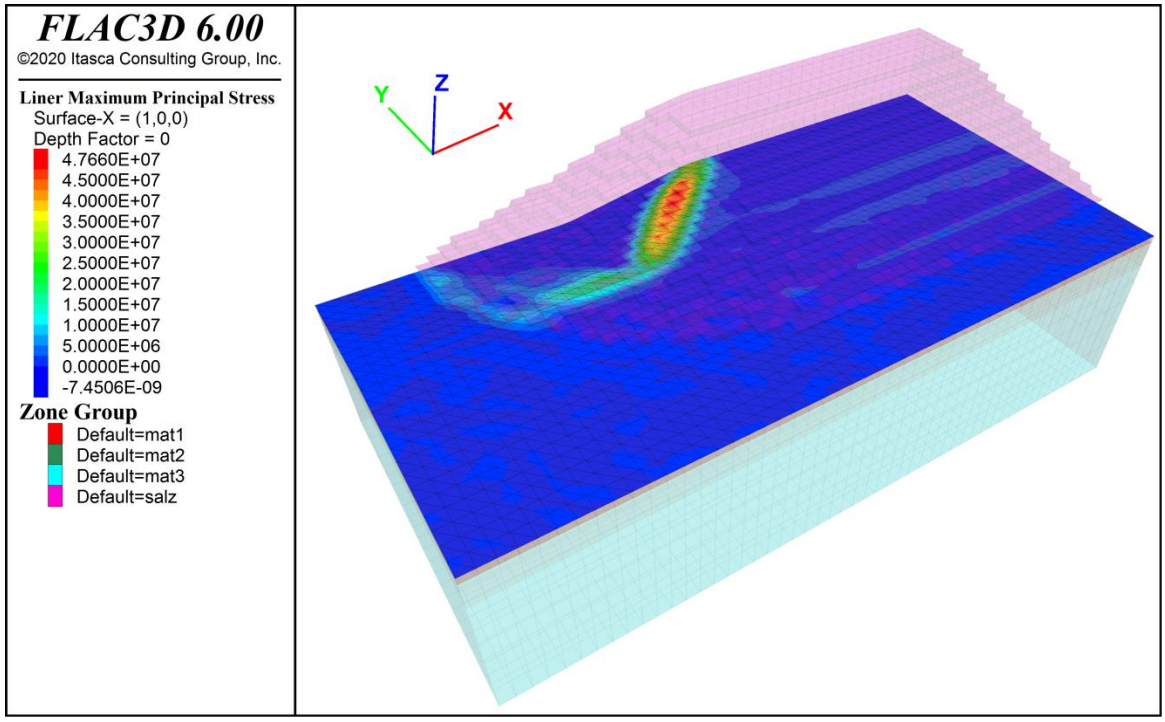

b)

Figure 6.16: Model 3D-valley:
a) Horizontal displacements in x-direction after 100 years,
b) Maximum principal stresses (Pa) in geomembrane

6.5 Discussion of results and conclusions

The discussion of the results focuses on the geomembrane. It aims in particular to what extent conclusions about the behavior of a geomembrane can be drawn from 2D models when considering a more complex topography of the contact area of a dump (real 3D situation). No project-specific topography is considered, but three quite different situations.

First of all, 3D models lead to significantly different results. These differences, of course, depend on the specific topographical situation, size and shape of the dump and the filling process, but also the parameters of the geomembrane, in particular, the friction angle between the geomembrane and the dump on the one hand and the ground on the other.

Even if the ground is plain, the 2D model gives different results than the 3D model, e.g., 32 m versus 25 m for the maximum horizontal displacement of the dump or 35 MPa versus 20 MPa for the maximum tensile stress in the geomembrane. In the considered case of a dump placed on the plain ground, it can be expected that displacements of the dump and also stresses inside the geomembrane are overestimated by 2D models (in this specific case by about 30%).

As expected, the uphill dumping reduces the horizontal displacements of the dump. This can be quite significant, as the example presented shows. This fact is confirmed by both 2D and 3D models, whereby the effect in the 2D case with a factor of 8 is about twice as large as in the 3D case with a factor of 4.

The maximum tensile load of the geomembrane is clearly overestimated in the "valley" situation in the 2D calculations (about a factor of 3). However, for the "mountain" situation, it is reversed: here, the 3D model shows a maximum tensile load of the geomembrane that is about 2.5 times higher.

In summary, the following can be stated:

The maximum horizontal displacements in the 2D and 3D models differ, but they are not extremely different (difference of approx. 30% to 50%). While the 2D model predicts higher displacement values for the “plain” and “valley” structures, it is the opposite for the “mountain” structure. Qualitatively similar results are obtained in the 3D case for the maximum tensile stresses in the geomembrane, but the differences are more pronounced here.

Thus, 2D calculations for the “plain” case and dumping into a “valley” structure are conservative concerning the displacements and loads of the geomembrane.

In the case of dumping over a ridge, the 2D calculations are not conservative, i.e., both displacements of the dump and the tensile stresses in the geomembrane are significantly underestimated.

In order to determine transfer functions (scaling factors) for the dump movements and geomembrane stresses (from 2D models to the real 3D situations), several at least approximate details of the 3D situation must be provided incl. the properties of the geomembrane and their interaction with the dump and the ground. However, for the “plain” and “valley” structures, 2D simulations are conservative and can be used to estimate upper bounds.

CHAPTER 7: CONCLUSIONS

This chapter summarizes the main research results in relation to the research aims and questions. It also reviews the limitations of the study and provides recommendations for future research.

The study aimed to simulate the behavior of geomembranes at large deformations using the proposed 'liner' model (element) in conjunction with FLAC^{3D}. The 'liner' element, which presents a geomembrane, includes two interfaces between the geomembrane and overlying and underlying material, respectively. The behavior of the 'liner' model itself is verified via uniaxial and biaxial pull-out tests.

The standard 'geogrid' and the new proposed 'liner' element were used to simulate pull-out tests and were compared with each other. The results in terms of pull-out resistance vs. displacement show that the 'geogrid' and 'liner' elements show similar results in the case of equal properties at both interfaces, whereby the 'liner' element is more accurate. It is important to note, that the 'liner' element has at least two major advantages: (1) it can describe the geomembrane behavior up to failure (cracking) incl. very large strain, and (2), it considers the interactions between geomembrane and overlying and underlying materials separately with the possibility to specify two different data sets for them.

In terms of the stress-strain response up to failure: realistic crack development of the geomembrane is proven for uniaxial and biaxial loading incl. different force ratios.

The main parameters (stiffness and friction) of the interfaces geomembrane/ overlying and geomembrane / underlying in a large-scale model were considered in detail. It was found that friction is the decisive parameter. When friction of the interface below is bigger than above, the loading on the geomembrane reaches a minimum, thereby minimizing friction above. Displacements of the liner become smaller and remain constant whenever the friction angle of the side below becomes bigger than 30^{o}.

To investigate the behavior of geomembranes at large deformation, salt dump simulations were performed exemplary. Therefore, a crushed salt constitutive model called 'Femesalz' was successfully developed and validated to describe the creep process of crushed salt. The model was validated in general using average field data from measurements and observations of huge salt dumps. This constitutive model was applied together with the 'liner' element to simulate the behavior of salt dumps via 2D and 3D models with more complex topography (plain, valley,

mountain). Comparing the results of the 2D and 3D models show that the maximum horizontal displacements between the 2D and 3D models differ by up to 30% to 50% for the given parameter constellation. The 2D models for the “plain” and “valley" cases are conservative with respect to the displacements and loads of the geomembrane and can be used to estimate upper bounds. However, for the ridge situation, the 2D modeling approach would underestimate the tensile stresses in the geomembrane considerably.

In the following some limitations are listed, which should be overcome by future research work:

- A more comprehensive constitutive model for the geomembrane itself as part of the ‘liner’ element should be developed because viscous behavior is not yet considered.
- The two interfaces on both sides of the geomembrane as part of the ‘liner’ element have also no viscous material behavior. Therefore, the constitutive interface model should be extended.
- The study should be extended by further modeling to duplicate the segmented construction according to the step-wise construction process in-situ. Although the proposed procedure allows that in general, the final proof is missing.
- An optimized initial meshing procedure or re-meshing algorithm should be developed to avoid illegal zone geometries in case of very large deformations.
- The ‘liner’ element representing a geomembrane should be applied also for other applications (not only for waste dumps). It should also be investigated if the ‘liner’ element works for other types of geosynthetics.

REFERENCE

(n.d.). Retrieved May 2, 2021, from https://www.naue.com/applications/mining/tailings-management/#iLightbox[a181d3eeaa7ea7a9033]/0

Abdi, M. R., & Zandieh, A. R. (2013). Finite Element Modeling of Pullout Test on Geogrid Embedded in Pluviated and Compacted layer of Sand. *The First Iranian Conference on Geotechnical Engineering*, (pp. 1-8).

Abu-Farsakh, M. Y., Almohd, I., & Farrag, K. (2006). Comparison of field and laboratory pullout tests on geosynthetics in marginal soils. *Transportation research record, 1975*(3), 124-136.

Atrechian, M., & Ahmadi, M. (2018). Studies on the Characteristics of the Type of Geotextiles. *The Civil Infrastructures Confronting Severe Weathers and Climate Changes Conference*, (pp. 257–269). Springer.

Bacas, B. M., Cañizal, J., & Konietzky, H. (2015). Shear strength behavior of geotextile/geomembrane interfaces. *Journal of Rock Mechanics and Geotechnical Engineering, 7*(6), 638-645.

Bacas, B. M., Konietzky, H., Berini, J. C., & Sagaseta, C. (2011). A new constitutive model for textured geomembrane/geotextile interfaces. *Geotextiles and Geomembranes, 29*(2), 137-148.

Backhaus, G. (1983). *Deformationsgesetze.* Akadermie- Verlag.

BAM. (2015). *Guidelines for the Certification of Protection Layers for Geomembranesin Landfill Sealing Systems.* Bundesanstalt für Materialforschung und Prüfung.

Bauer, G. E., & Mowafy, Y. M. (1988). The interaction mechanism of granular soils with geogrids. In *International Conference on Numerical Methods in Geomechanics* (pp. 1263-1272). AA Balkema.

Beneito, C., & Gotteland, P. (2020). Three-Dimensional Numerical Modeling of Geosynthetics Mechanical Behavior. In *FLAC and Numerical Modeling in Geomechanics* (pp. 191-198). CRC Press.

Bhattacharjee, A., Prashanth, V., & Krishna, A. M. (2011). Numerical Modelling of Pull-out test for Reinforcement in oblique direction. *Indian Geotechnical Conference*, (pp. 891-894).

Boley, C. (1999). *Untersuchungen zur Viskoplastizität und Festigkeit von Steinsalz.* Mitteilungen des Instituts und der Versuchsanstalt für Geotechnik der Technischen, Universität Darmstadt, Heft 48.

Boresi, A. P., & Deere, D. U. (1963). *Creep closure of a spherical cavity in an infinite medium (with special application to Project Dribble, Tatum Salt Dome, Mississippi). (TID-20083).* Illinois. Univ., Urbana.

Callahan, G. D. & DeVries, K. L. (1991). *Analyses of backfilled transuranic wastes disposal rooms (SAND91 - 7052).* Sandia National Laboratories.

Callahan, G. D. (1999). *Crushed salt constitutive model (SAND98-2680).* Sandia National Laboratories.

Cen, W. J., Wang, H., & Sun, Y. J. (2018). Laboratory investigation of shear behavior of high-density polyethylene geomembrane interfaces. *Polymers, 10*(7), 734.

Chen, C., McDowell, G. R., & Thom, N. H. (2013). A study of geogrid-reinforced ballast using laboratory pull-out tests and discrete element modelling. *Geomechanics and Geoengineering, 8*(4), 244-253.

Dolez, P. I., & Blond, E. (2017). Evaluation of geotextile performance for the filtration of fine-grained tailings. In *Geotechnical Frontiers 2017* (pp. 269-277). ASCE.

Duszyńska, A., & Bolt, A. F. (2004). Pullout tests of geogrids embedded in non-cohesive soil. *Archives of Hydro-Engineering and Environmental Mechanics, 51*(2), 135-147.

Effendi, R. (2011). Interface Friction Of Smooth Geomembranes and Ottawa Sand. *INFO-TEKNIK, 12*(1), 61-72.

Ferreira, F. B., Vieira, C. S., & Lopes, M. D. (2020). Pullout behavior of different geosynthetics-influence of soil density and moisture content. *Frontiers in Built Environment, 6*, 12.

Fischer, A., Artschwager, F., & Schleining, J.-P. (2022). *schriftliche Mitteilung.*

Garside, M. (2021). Retrieved Aug 22, 2021, from https://www.statista.com/topics/1143/mining/

Greenwood, J. H., Schroeder, H. F., & Voskamp, W. (2015). Durability of geosynthetic. CRC Press.

Günther, R. M. (2009). *Erweiterter Dehnungs-Verfestigungs-Ansatz: phänomenologisches Stoffmodell für duktile Salzgesteine zur Beschreibung primären, sekundären und tertiären Kriechens (Ph. D. Thesis).* Institut für Geotechnik, TU Bergakademie Freiberg.

Günther, R. M., Lüdeling, C., Popp, T., Naumann, D., Wiedemann, M., & Weise, D. (2016). Vergleich aktueller Stoffgesetze und Vorgehensweisen anhand von Modellberechnungen zum thermo-mechanischen Verhalten und zur Verheilung von Steinsalz. *Teilvorhaben, 2*, 184.

Günther, R. M., Salzer, K., Popp, T., & Lüdeling, C. (2015). Steady-state creep of rock salt: improved approaches for lab determination and modelling. *Rock mechanics and rock engineering, 48*(6), 2603-2613.

Hegde, A., & Roy, R. (2018). A comparative numerical study on soil–geosynthetic interactions using large scale direct shear test and pullout test. *International Journal of Geosynthetics and Ground Engineering, 4*(1), 1-11.

Herrmann, W., Wawersik, W. R., & Lauson, H. S. (1980). *Analysis of steady state creep of southeastern New Mexico bedded salt (No. SAND-80-0558).* Sandia National Laboratories.

Herrmann, W., Wawersik, W. R., & Lauson, H. S. (1980). *Creep Curves and Fitting Parameters for Southeastern New Mexico Rock Salt (No. SAND-80-0087)* . Sandia National Laborataries.

Hou, Z. (1999). *Untersuchungen zum Nachweis der Standisicherheit für Untertagedeponien im Salzgebire. (Ph. D. Thesis).* TU Clausthal.

Hsieh, C. W., Chen, G. H., & Wu, J. H. (2011). The shear behavior obtained from the direct shear and pullout tests for different poor graded soil-geosynthetic systems. *Journal of GeoEngineering, 6*(1), 15-26.

Hunsche, U., Schulze, O., & Langer, M. (1994). Creep and failure behavior of rock salt around underground cavities. *Proc 16th World Mining Congress, Sofia*, *5*, pp. 217-230.

Hussein, M. G., & Meguid, M. A. (2013). Three-dimensional finite element analysis of soil- geogrid interaction under pull-out loading condition. *GeoMontreal 2013, the 66th Canadian Geotechnical Conference. 1*, pp. 452-458. Canadian Geotechnical Society.

Itasca. (2016). *FLAC3D, Verson 6.0, Manual.* Itasca Consulting Group.

Itasca. (2017). *Stoffmodell zur Beschreibung des Verhaltens von Rückstandshalden.* Itasca Consultants GmbH.

Jewell, R. A., Milligan, G. W., & Dubois, D. (1985). Interaction between soil and geogrids. *Polymer grid reinforcement* (pp. 18-30). Thomas Telford Publishing.

Juran, I., Knochenmus, G., Acar, Y. B., & Arman, A. (1988). Pull-out response of geotextiles and geogrids (synthesis of available experimental data). In *Geotechnical Special Publication* (pp. 92-111). ASCE.

Kayadelen, C., Önal, T. Ö., & Altay, G. (2018). Experimental study on pull-out response of geogrid embedded in sand. *Measurement, 117*, 390-396.

Konietzky, H., te Kamp, L., Groeger, T., & Jenner, C. (2004). Use of DEM to model the interlocking effect of geogrids under static and cyclic loading. *The 2nd International PFC Symposium* (pp. 3-12). Balkema.

Leppla, S. (2021). Simulation of Viscoplastic Material Behavior in Numerical Models. In *International Conference of the International Association for Computer Methods and Advances in Geomechanics* (pp. 465-473). Springer.

Lopes, M. L., & Silvano, R. (2010). Soil/geotextile interface behavior in direct shear and pullout movements. *Geotechnical and geological engineering, 28*(6), 791-804.

Lüdeling, C., & Minkley, W. (2014). A Crushed–Salt Model with Creep, Compaction and Strain Softening, and Application to Tailings Heaps. *48th US Rock Mechanics/Geomechanics Symposium.* ARMA-2014-7037.

Markou, I. N. (2018). A study on geotextile-sand interface behavior based on direct shear and triaxial compression tests. *International Journal of Geosynthetics and Ground Engineering, 4*(1), 1-15.

Matthew, A. (2021). Retrieved April 17, 2022, from https://industrialplastics.com.au

McDowell, G. R., Harireche, O., Konietzky, H., Brown, S. F., & Thom, N. H. (2006). Discrete element modelling of geogrid-reinforced aggregates. *Proceedings of the Institution of Civil Engineers-Geotechnical Engineering, 159*(1), 35-48.

Milligan, G. W. (1988). Prediction of bond between soil and reinforcement. *Prediction and Performance in Geotechnical Engineering. 1*, pp. 147-153. CRC Press.

Minažek, K. (2013). A review of soil and reinforcement interaction testing in reinforced soil by pull-out test. *Građevinar, 65*, 235-250.

Minkley, W., Bérest, P., Schleinig, J. P., Farkas, F., & Böttge, V. (2012). Dynamic back-calculation of the collapse of the Saint-Maximilien mining field during mining on rock salt in Varangéville (1873). *Mechanical Behavior of Salt VII*, 241-252.

Mohiuddin, A. (2013, Aug). *Analysis of laboratory and field pull-out tests of geosynthetics in clayey soils. (Master thesis).* Louisiana State University and Agricultural and Mechanical College.

Moraci, N., & Cardile, G. (2008). Pullout behavior of different geosynthetics embedded in granular soils. In *Geosynthetics in Civil and Environmental Engineering* (pp. 146-150). Springer.

Moraci, N., Cazzuffi, D., Calvarano, L. S., Cardile, G., Gioffrè, D., & Recalcati, P. (2014, June). The influence of soil type on interface behavior under pullout conditions. *Geosynthetics, 32*(3), 42-50.

Munson, D. E. (1979). *Constitutive model for the low temperature creep of salt (with application to WIPP) (No. SAND-79-1853).* Sandia National Laborataries.

Murthy, B. S., & Sridharan, A. (1993). Evaluation of interfacial frictional resistance. *Geotextiles and Geomembranes, 12*(3), 235-253.

Nguyen, M. D., Yang, K. H., Lee, S. H., Wu, C. S., & Tsai, M. H. (2013). Behavior of nonwoven-geotextile-reinforced sand and mobilization of reinforcement strain under triaxial compression. *Geosynthetics International, 20*(3), 207-225.

Norton, F. H. (1929). *The creep of steel at high temperatures.* (No. 35). McGraw-Hill Book Company, Incorporated.

Odqvist, F. G., Hoff, N. J., & Hult, J. (1963). In *Kriechfestigkeit metallischer Werkstoffe* (Vol. 30, pp. 478-479). Springer.

Olivella, S., & Gens, A. (2002). A constitutive model for crushed salt. *International journal for numerical and analytical methods in geomechanics, 26*(7), 719-746.

Palmeira, E. M., Beirigo, E. A., & Gardoni, M. G. (2010). Tailings-nonwoven geotextile filter compatibility in mining applications. *Geotextiles and Geomembranes, 28*(2), 136-148.

Pelyk, L. V., Vasylechko, V. O., & Kyrychenko, O. V. (2019). Influence of Biodestructors on the Wear Resistance of Polyester Geotextile Materials. *Colloids and Interfaces, 3*(1), 21.

Perkins, S. W., & Edens, M. Q. (2003). Finite element modeling of a geosynthetic pullout test. *Geotechnical & Geological Engineering), 21*(4), 357-375.

Post, A., & Maubeuge, K. V. (2018). The use of geosynthetics in mining work. *Mining report Glückauf, 154*, 236-244.

Prambauer, M., Wendeler, C., Weitzenböck, J., & Burgstaller, C. (2019). Biodegradable geotextiles–An overview of existing and potential materials. *Geotextiles and Geomembranes, 47*(1), 48-59.

Pries, J., & Westhus, S. (2014). The use of geosynthetics in mining works. *The 20th WestCon Conference, Somerset West*, (pp. 189-194).

Rawal, A., Shah, T. H., & Anand, S. C. (2016). Geotextiles in civil engineering. In *Handbook of technical textiles* (pp. 111-133). Woodhead Publishing.

Salzer, K. (1993). Ableitung eines kombinierten Kriechgesetzes unter Berücksichtigung der Erholung. *Teilbericht zum BMFT Vorhaben, 2*.

Sayao, A. S., Nunes, A. L., Becker, L. D., & Sieira, A. C. (2009). Behavior of geogrids under pull-out tests in fine and coarse soils. In *Proceedings of the 17th International Conference on Soil Mechanics and Geotechnical Engineering* (pp. 865-868). IOS Press.

Schmachtenberg, E. (1985). *Die mechanischen Eigenschaften nichtlinear viskoelastischer Werkstoffe (Ph. D. Thesis).* Rheinisch-Westfälische Technische Hochschule Aachen.

Senseny, P. E. (1985). Determination of a constitutive law for salt at elevated temperature and pressure. In *ASTM International* (pp. 55-71).

Shirazi, S. G., Valipourian, K., & Golhashem, M. R. (2019). A Review on Geomembrane Characteristics and Application in Geotechnical Engineering. *International Journal of Civil and Environmental Engineering, 13*(8), 494-501.

Sjaardema G. D., K. R. (1987). *A constitutive model for the consolidation of WIPP crushed salt and its use in analyses of backfilled shaft and drift configurations (SAND-87-1977).* Sandia National Laboratories.

Stahl, M., & Konietzky, H. (2011). Discrete element simulation of ballast and gravel under special consideration of grain-shape, grain-size and relative density. *Granular Matter, 13*(4), 417-428.

Stepanovic, J. M., Trajkovic, D., Stojiljkovic, D., & Djordjic, D. (2016). Predicting the behavior of non-woven geotextile materials made of polyester and polypropylene fibers. *Textile Research Journal, 86*(13), 1385-1397.

Tuna, S. C., & Altun, S. E. (2012). Mechanical behavior of sand-geotextile interface. *Scientia Iranica, 19*(4), 1044-1051.

Tuomela, A., Ronkanen, A. K., Rossi, P. M., Rauhala, A., Haapasalo, H., & Kujala, K. (2021). Using Geomembrane Liners to Reduce Seepage through the Base of Tailings Ponds- A Review and a Framework for Design Guidelines. *Geosciences, 11*(2), 93.

Wachter, S. (2009). *Dreidimensionale, zeitvariante stoffliche Modellierung von granularem Steinsalz (Ph. D. Thesis).* Institut für Geotechnik, TU Darmstadt.

Wallner, M. (1983). Stability calculations concerning a room and pillar design in rock salt. *In 5th ISRM Congress*, (pp. D9-D15).

Wang, G. (2004). A new constitutive creep-damage model for salt rock and its characteristics. *International Journal of Rock Mechanics and Mining Sciences, 41*, 61-67.

Wiewel, B. V., & Lamoree, M. (2016). Geotextile composition, application and ecotoxicology- A review. *Journal of Hazardous Materials, 317*, 640-655.

Xu, C., & Liang, C. (2018). DEM Simulation of pullout tests of geogrid-reinforced gravelly sand. In *GeoShanghai International Conference* (pp. 446-454). Springer.

Zhang Q., S. Z. (2021). Creep Properties and Constitutive Model of Salt Rock. *Advances in Civil Engineering, 2021*.

Zhang, J., Yasufuku, N., & Ochiai, H. (2008). Discrete element modelling of geogrid pullout test. In *Geosynthetics in Civil and Environmental Engineering* (pp. 11-14). Springer.

Zornberg, J. G., & Christopher, B. R. (2007). Chapter 37: Geosynthetics. In *The Handbook of Groundwater Engineering, 2nd Edition by Jacques W. Delleur* (pp. 1270-1305). CRC Press.